

ANALOG CONTROLLER
BASED ON SLIDING MODE CONTROL
FOR PIEZOELECTRIC ACTUATORS

By
SELİM YANNIER

Submitted to the Graduate School of Engineering and Natural Sciences
in partial fulfillment of
the requirements for the degree of
Doctorate of Philosophy


SABANCI UNIVERSITY

Spring 2008

ANALOG CONTROLLER
BASED ON SLIDING MODE CONTROL
FOR PIEZOELECTRIC ACTUATORS

APPROVED BY:

Prof. Dr. ASIF ŞABANOVIĆ
(Dissertation Advisor)



Assistant Prof. Dr. AYHAN BOZKURT



Associate Prof. Dr. MUSTAFA ÜNEL



Assistant Prof. Dr. KEMALETTİN ERBATUR



Prof. Dr. METİN GÖKAŞAN



DATE OF APPROVAL: 17.07.2008

© Selim Yannier 2008

All rights reserved.

ANALOG CONTROLLER BASED ON SLIDING MODE CONTROL
FOR PIEZOELECTRIC ACTUATORS

Selim Yannier

EECS, PhD Thesis, 2008

Thesis Supervisor: Prof. Dr. Asıf Şabanoviç

Keywords: Sliding Mode Control, Disturbance Observer, Analog Controller,
Piezoelectric Actuation

ABSTRACT

Today, the digital implementation of the controllers is mainly preferred from re-programmability point of view. Many important control problems can be effectively solved using a digital architecture in conjunction with analog-to-digital (ADC) and/or digital-to-analog conversion (DAC). Digital solutions offer two very attractive advantages: (1)-promise to shorten design cycles, and (2)-provide the freedom to reprogram the design in simple ways. This ease-of-change stands in sharp contrast to the great effort required to redesign a typical hard-wired analog implementation.

However, depending on the complexity of the plant and the degrees of freedom (DOF) to be controlled, digital implementation of an algorithm may be demanding due to the high computational power requirement to run in real time. The necessity for the acquisition of the analog signals on the other hand requires ADC and DAC conversions that compel extra conditions on the system. Hence, multi-DOF systems may require either diminish in the systems operation frequency or additional hardware to run the algorithm in parallel for each DOF.

This work aims to develop an analog motion controller for single input single output (SISO) plants of complex nature. As the control algorithm, Sliding Mode Control (SMC) like the well known robust nonlinear controller is selected as a design framework. Originally designed as a system motion for dynamic systems whose essential open-loop behavior can be sufficiently modeled with ordinary differential equations, Sliding Mode Control (SMC) is one of the effective nonlinear robust control approaches that provide system invariance to uncertainties once the sliding mode motion is enforced in the system. An important aspect of sliding mode is the discontinuous nature of the control action, which switches between two values to move

the system motion on so-called “sliding mode” that exist in a manifold and therefore often referred as variable structure control (VSC). The resulting feedback system is called variable structure system (VSS).

The position tracking of the piezoelectric actuators (PEA) is selected as the test bed for the designed system. Piezoelectricity, the ability of the material to become strained due to an electric field, gives the possibility to use those materials as actuator in sub-micrometer domain for a range of applications. Piezoelectric effect is a crystalline effect, and therefore, piezoelectric actuators do not suffer from “stick slip” effect mainly caused by the friction between elements of a mechanical system. This property theoretically offers an unlimited resolution, and therefore piezoelectric actuators are already used in many applications to provide sub-micrometer resolution. Still the achievable resolution in practice can be limited by a number of other factors such as the piezo control amplifier (electronic noise), sensor (resolution, noise and mounting precision) and control electronics (noise and sensitivity to EMI).

As a result of this work, we are aiming an analog controller for SISO systems and by the use of this controller, improvement on the tracking performance for the plant we are studying and decrease on the possible computational load on digital controllers is targeted.

PİEZOELEKTRİK HAREKETLENDİRİCİLER İÇİN
KAYAN KIPLI DENETİM TABANLI ANALOG DENETLEYİCİ

Selim Yannier

EECS, Doktora Tezi, 2008

Tez Danışmanı: Prof. Dr. Asif Şabanoviç

Anahtar Kelimeler: Kayan Kipli Denetim, Bozulma Denetleyici, Analog Denetleyici,
Piezoelektrik Hareketlendirici

ÖZET

Denetim algoritmalarının sayısal olarak uygulanması temelde tekrar programlanabilirlik açısından tercih edilmektedir. Birçok önemli denetim problemi, analog-sayısal çevirici ve sayısal-analog çeviriciler ile salt sayısal yöntemler ve donanım kullanılarak çözülebilir. Sayısal çözümler iki temel avantaj vaat eder; (1) tasarım süreçlerini kısaltma ve (2) tasarımın yeniden programlanabilmesi. Bu kolay programlanabilirlik, klasik olarak tasarlanmış analog uygulamaların tekrar düzenlemesi için gerekli çalışma miktarı ile zıtlık gösterir.

Ancak, denetlenecek sistemin karmaşıklığı ve denetlenecek serbestlik derecesi sayısına bağlı olarak, gerek hesaplama gücü ihtiyacı açısından, gerek algoritmaların gerçek zamanda çalışma ihtiyacı açısından, sayısal uygulamalar oldukça zorludur. Analog sinyallerin, analog-sayısal çeviriciler ile toplanması ve çıktıların sayısal-analog çeviriciler ile iletilmesi ise tüm sistem üzerinde fazladan sınırlamalar yaratmaktadır. Dolayısıyla, çok serbestlik dereceli sistemler ya genel çalışma frekansında yavaşlama ya da her bir serbestlik için farklı donanımda denetim gerektirmektedir.

Bu çalışma, tek giriş tek çıkışlı (TGTÇ) dinamik sistemler için bir analog denetleyiciler tasarlamayı ve gerçekleştirmeyi amaçlıyor. Denetim algoritması için iyi bilinen, gürbüz ve performansını kanıtlamış, Kayan Kipli Denetim (KKD) tercih edilmiştir. Aslen, açık çevirim davranışları standart türevsel denklemler ile yeteri kadar modellenebilir sistemler için tasarlanmış olan KKD, sistem bir kez kayan kipe taşındığında, sistem parametreleri değişimi de dahil tüm dış etkilere karşı direnç ve gürbüzlük sağlar. KKD'in önemli bir özelliği de sistemi kayan kipe taşımak için, genelde iki farklı değer arasında anahtarlayan ve sürekli olmayan denetim hareketidir.

Tasarımı yapılan denetim sisteminin deneysel alıřmaları iin piezoelektrik hareketlendiriciler test sistemi olarak seilmiřtir. Piezoelektrik zellik, maddenin bir elektrik alana maruz kalınca genleřmesidir. Bu zellięe sahip malzemeler mikrometre ve altı hassasiyette hareket retici olarak kullanılabilirler. Piezoelektrik zellik, malzemenin kristal yapısının bir zellięi olup, srtnme ve yapıřma gibi mekanik etkilere maruz kalmadıęından teoride sonsuz znrlkte hareket olanaęı tanır. Ancak, uygulamalarda znrlk birok etken yznden sınırlı kalır; piezo denetim g ykseltecisi (grlt miktarı), algılayıcı (geri besleme znrlę, grlt, montaj hassasiyeti) ve denetim elektronięi (grlt ve elektromanyetik etkileřim) birkaç rnekir.

Bu alıřmanın sonucu olarak, TGT sistemleri iin bir analog denetleyici yaratılması planlanmıřtır. Bu yolla, denetimi yapılan sistemin referans izleme performansının arttırılması ve karmařık sistemlerde denetleyicinin sayısal alan dıřına tařınarak, hesaplama gc ihtiyalarının dřrlmesi hedeflenmiřtir.

To;
Habib & V. Vivet Yannier, “*full-time parents*” since April 1978,
Alper Yannier, “*full-time brother*” since August 1982,
and *Sibel Saranga*.

ACKNOWLEDGEMENTS

I wish to express my thankfulness to a number of people who became involved with this thesis, one way or another. First of all, I would like to convey my special thanks to Prof. Asif Şabanoviç, my thesis advisor and a true gentleman whose suggestions and encouragement led me find my way throughout this research. He has always been enthusiastic in guidance regarding the theoretical work and answering my questions, no matter how irrelevant they are. Thank you for being available whenever I needed you and for proposing me this research topic.

I would also like to give my thanks to Prof. Mustafa Ünel and Prof. Kemalettin Erbatur, member of the thesis committee, and my instructors in the past semesters. You were so polite in providing me the tools I needed for research and documentation.

I cannot forget my friend: thanks to all mechatronics people for their friendship. Especially to current and past graduate students who have spent numerous nights, together with me, in the laboratory; Kazım Çakır, A. Teoman Naskali, Emrah Deniz Kunt, Özkan Bebek, Nusrettin Güleç, Elif Hoccoğlu, A. Fatih Tabak, Meltem Elitaş, Merve Acer, Utku Seven, Ertuğrul Çetinsoy. İlker Sevgen, our laboratory technician, I cannot omit your name.

I owe many thanks to my parents Habib and Vivet, as well as my brother Alper, who were supportive of my academic enthusiasms.

Finally, my future spouse Sibel, thank you for your everlasting support.

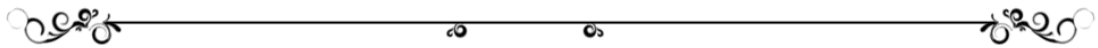


TABLE OF CONTENTS

ABSTRACT.....	IV
ÖZET	VI
ACKNOWLEDGEMENTS.....	IX
TABLE OF CONTENTS.....	X
LIST OF FIGURES	XIII
LIST OF TABLES.....	XVI
TABLE OF SYMBOLS.....	XVII
TABLE OF ABBREVIATIONS	XXI
1 INTRODUCTION	1
1.1 Motivation.....	1
1.2 Objectives of the Thesis.....	2
1.3 Structure of the Thesis	3
2 MODELING AND CONTROL OF PIEZOELECTRIC ACTUATORS.....	4
2.1 Piezoelectric Actuation.....	4
2.1.1 Daily Use of Piezoelectricity	4
2.1.2 Piezoelectricity for Nanopositioning	6
2.1.3 Major Piezoelectric Actuator Types	7
2.1.4 Features of Piezoelectric Actuators	8
2.1.5 Disadvantages of Piezoelectric Actuators.....	9
2.2 Piezoelectric Actuator Models.....	11
2.3 Hysteresis Models.....	13
2.4 Control of Piezoelectric Actuators.....	14
2.5 Disturbance Observer	17
2.5.1 Reduced Order Luenberger Observer.....	19
3 DESIGN AND IMPLEMENTATION	21
3.1 Modeling Piezoelectric Actuator	21
3.2 Hysteresis Model	24
3.3 Model Parameters	26

3.4	Sliding Model Control	27
3.4.1	Definitions	28
3.4.2	Controller Design.....	28
3.4.2.1	Sliding Manifold	29
3.4.2.2	Computation of the Necessary Control Action.....	29
3.4.2.3	Equations of Motion	31
3.4.2.4	Discrete Time Implementation	31
3.4.2.5	Stability in Discrete Time Implementation.....	33
3.4.2.6	Continuous Time Implementation and Stability.....	33
3.4.2.7	Approximation Error.....	35
3.5	Estimation of Disturbance for PEA	35
3.6	Reduced Order Luenberger Observer.....	38
3.7	Design Considerations	40
3.8	Circuit Design.....	42
3.8.1	Analog Computing and Scaling.....	44
3.8.2	Designed Control and Scaling	45
3.8.3	Position Measurement.....	46
3.8.3.1	Strain Gage	46
3.8.3.2	Position Measurement for PEA	49
3.8.4	Electronics Structure.....	50
3.8.4.1	Error Calculation.....	50
3.8.4.2	Calculation of Error's Derivatives.....	51
3.8.4.3	Calculation of the Sliding Surface " σ "	53
3.8.4.4	Calculation of the Intermediate Signal " φ "	53
3.8.4.5	Calculation of the Intermediate Signal " $\alpha \cdot \dot{x}$ "	54
3.8.4.6	Calculation of the Intermediate Signal " ψ "	55
3.8.4.7	Calculation of the Control Output " u ".....	56
3.8.5	High Voltage Amplifier.....	56
3.8.5.1	Power Limitation	57
3.8.5.2	The Effect of HVA	58
3.9	Analysis	60
3.9.1	Plant Analysis	63
3.9.1.1	Transient Response Analysis.....	63

3.9.1.2	Frequency Response Analysis	64
3.9.2	Controller Analysis	65
3.9.2.1	Frequency Analysis: Open Loop vs Closed Loop	66
3.9.2.2	Disturbance Observer Analysis	67
3.9.3	Circuit Simulations	69
4	EXPERIMENTAL RESULTS	72
4.1	Experimental Setup	72
4.2	Model Verification	73
4.3	Open Loop Actuator Control	75
4.4	Position Tracking Experiments Using DSP	76
4.5	Analog SMC Position Tracking Experiments	77
4.6	Analog SMC with Disturbance Observer	80
4.7	Summary of the Experimental Results	83
5	CONCLUSION AND FUTURE WORK	86
5.1	Conclusions	86
5.2	Recommendations and Future Work	88
6	REFERENCES	90



LIST OF FIGURES

Figure 2.1: Electrical connection of disks in a stack type piezoelectric actuator [7].	7
Figure 2.2: Measures hysteresis curves for voltage/displacement and force/displacement relations.	10
Figure 2.3: Open-loop step response of the piezoelectric actuator. “d” is the displacement difference due to hysteresis. Creep effect is magnified in the circular view [40].	11
Figure 2.4: Electrical equivalent circuit for piezoelectric actuators; equivalent circuit model for unloaded piezoelectric ceramics on the left and proposed circuit model for the piezoelectric structure on the right [43]	12
Figure 2.5: Schematic representation of the different representations in a piezoelectric actuator.	14
Figure 2.6: Motion Control system with disturbance observer.	18
Figure 3.1: Electromechanical model of the piezoelectric actuator.	22
Figure 3.2: Block diagram representation of the electromechanical model.	24
Figure 3.3: Example hysteresis loop and its characteristics [26].	24
Figure 3.4: Datasheet for the piezoelectric actuator: PSt 150/5/60 VS10.	27
Figure 3.5: The relations between measured and calculated variables for discrete time systems without computational delay.	32
Figure 3.6: Observer implementation.	38
Figure 3.7: General scheme of the controller.	44
Figure 3.8: An example strain gage.	47
Figure 3.9: The Wheatstone Bridge.	48
Figure 3.10: (Left) Bending beam example with two strain gages installed. (Right) Bridge configurations for two gages measurements.	49
Figure 3.11: Calculation of the error.	50
Figure 3.12: The differentiator block used to calculate the error’s derivative.	51
Figure 3.13: Bode plot for an ideal differentiator as in comparison to the open-loop gain.	52

Figure 3.14: Calculation of the sliding surface.....	53
Figure 3.15: Calculation of the Intermediate Signal “ φ ”.....	54
Figure 3.16: Calculation of the Intermediate Signal “ $\alpha \cdot \dot{x}$ ”.....	55
Figure 3.17: Calculation of the Intermediate Signal “ ψ ”.....	55
Figure 3.18: Calculation of the Control Output “ $-u$ ”.....	56
Figure 3.19: High voltage amplifier as a final block of the circuit.....	57
Figure 3.20: Observer implementation with the addition of the HVA.....	60
Figure 3.21: The block diagram of the full control scheme.....	61
Figure 3.22: Analog Sliding Mode Controller block diagram. \hat{u} is used to mark the input point of the disturbance observer.....	62
Figure 3.23: Transient response of the open-loop PEA plant to a unit-step input.....	63
Figure 3.24: The frequency response analysis of the open-loop plant (PEA): wide frequency range on the left and closer view on the right.....	65
Figure 3.25: Open-loop vs closed loop frequency response plots for PEA. The closed loop does not contain disturbance observer information.....	66
Figure 3.26: Gain and phase margins for closed loop system calculated by MatLab.	67
Figure 3.27: Frequency response analysis for plant under control with and without the disturbance observer: the reference tracking analysis on the left and disturbance rejection analysis on the right.....	68
Figure 3.28: Disturbance rejection performance comparison for different parameters by means of Bode plot.....	69
Figure 3.29: Plant representation for circuit simulation purposes.....	70
Figure 3.30: Circuit analysis results.....	70
Figure 4.1: Piezoelectric actuator control setup.....	72
Figure 4.2: Actual photo of the experimental setup.....	73
Figure 4.3: Real vs. simulated trajectory of the PEA for the input: $u=40+40.\sin(t)$ Volts presented with the corresponding modeling error.....	74
Figure 4.4: Real vs. simulated trajectory of the PEA for the input: $u=15+15.\sin(t)$ Volts presented with the corresponding modeling error.....	74
Figure 4.5: Inverse plant model for the Goldfarb-Celanovic model.....	75
Figure 4.6: Open-loop tracking error and input voltage for $x_d = 7.5 + 7.5 \cdot \sin(t) \mu m$	76
Figure 4.7: DSP tracking of 4.5um-pp 1Hz sinusoidal reference. The error is 110nm-pp (2.4%).....	76

Figure 4.8: DSP tracking of 10.8um-pp 1Hz sinusoidal reference. The error is 200nm-pp (1.8%).	77
Figure 4.9: ASMC tracking experiments for 4.5 and 10.8um-pp 1Hz sinusoidal references.	78
Figure 4.10: ASMC tracking experiments for 4.5um-pp and 10.8um-pp 1Hz triangular references.	79
Figure 4.11: ASMC with DO tracking experiments for 4.5 and 10.8um-pp 1Hz sinusoidal references.	81
Figure 4.12: ASMC with DO tracking experiments for 4.5 and 10.8um-pp 1Hz triangular references.	82
Figure 4.13: Tracking of human hearth beat signal. The peak to peak reference signal is 21.70um. The error is 46nm-pp (0.21%).	82
Figure 4.14: Tracking of 35.60um-pp 1Hz sinusoidal reference. The error is 54nm-pp (0.15%).	84



LIST OF TABLES

Table 2.1: Comparison of typical actuator properties [31].	8
Table 3.1: Material properties for lead zirconate titanate (PZT), the piezoelectric crystal of the used actuator for the experiments in this work.	23
Table 3.2: Nominal values for plant parameter used in this work [26].	26
Table 3.3: TLE074 electrical characteristics [69].	41
Table 3.4: MP108 electrical characteristics [70].	42
Table 3.5: Assumed maximum values for signals and parameters.	46
Table 3.6: Parameters used in the disturbance rejection performance study.	69
Table 4.1: Summary of the experimental results.	83

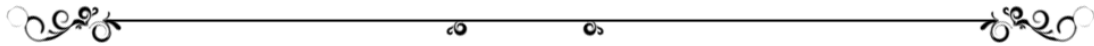


TABLE OF SYMBOLS

$L(t)$	piezoelectric actuator's displacement for any fixed input voltage
L_0	nominal constant displacement value
γ	creep factor
T_{ij}	stress component
c_{ijkl}^E	elastic stiffness
e_{kij}	piezoelectric constants
E_k	electric field
D_i	electric displacement
S_{kl}, ε	strain
$P, P(s)$	actual plant transfer function
r	reference input
y	plant output
u	control input
ξ	observer noise
a_i	constant coefficients
$G, g(s)$	low-pass filter transfer function
\hat{d}	estimated disturbance model
m	mass
m_N	nominal mass
c	damping coefficient
c_N	nominal damping
k	springness coefficient
k_N	nominal springness
T	piezoelectric effect conversion constant

T_N	nominal piezoelectric effect conversion constant
F_d	disturbance force
\hat{F}_d	estimated disturbance force
z	intermediate state variable
\hat{z}	estimated value of the intermediate state variable z
l	Luenberger constant
$Q(s)$	low pass filter
$H(q)$	hysteresis effect as a function of charge q
q	charge
\dot{q}	total current flowing through the circuit
h	voltage due to the hysteresis effect
q_p	transduced charge from the mechanical side
u_p	voltage due to the piezo effect
u	total voltage over the piezoelectric actuator
F_p	transduced force from the electrical side
F_{ext}	external applied force
x	elongation of the piezoelectric actuator.
E	elasticity modulus
η	viscosity
ρ	mass density
L	length
A	cross-sectional area
d , <i>dist</i>	disturbance
$f(h)$, $g(h)$	functions defining the shape of the hysteresis loop
α , a , b	constant parameters
u_{hc}	average voltage applied to the actuator by the sinusoidal input
q_c	corresponding average charge to u_{hc}
q_{ll}	lower left point of the hysteresis loop
q_{ur}	upper right point of the hysteresis loop
$2A$	maximum input amplitude

ε	area of the hysteresis loop
\tilde{u}	voltage offset
ω	angular frequency
$x^T \in \mathfrak{R}^n$	state vector
$u \in \mathfrak{R}^m$	control vector
$f(x) \in \mathfrak{R}^n$	unknown, continuous and bounded nonlinear function
$B(x) \in \mathfrak{R}^{n \times m}$	known input matrix with continuous and bounded elements
$d \in \mathfrak{R}^n$	unknown, bounded external disturbance
h_i	Coulomb friction term
g_i	interaction term
u	control input
\hat{u}	correction term calculated by the disturbance observer
u_0	control output from the Sliding Mode Controller alone
$x_1(t), \dots, x_n(t)$	system states/trajectories
$x_{d_1}(t), \dots, x_{d_n}(t)$	desired states/trajectories
S	function defining the sliding manifold
$V(\sigma)$	Lyapunov function candidate
σ	sliding function
$e_t = [e_1, \dots, e_n]^T$	error vector
D	a positive definite symmetric matrix used as a design parameter
μ	a design parameter
T	sampling time of the digital system
kT	the current control cycle
$kT + T$	the next control cycle
$kT - T$	the previous control cycle
t	time
u_{eq}	equivalent control
z	approximated equivalent control
\mathcal{E}_{ueq}	difference between real and approximated equivalent controls
u_{app}	approximated control

ε_u	error between the approximated and un-approximated controls
\bullet_N	nominal value of a parameter
$\Delta \bullet$	deviation of the parameter from its nominal value \bullet_N
$\varphi, \alpha \cdot \dot{x}, \psi$	intermediate signals to simplify the topology
GF	gage factor for the strain gage
C_\bullet	capacitor values
R_\bullet	resistance values
ΔR	change in the resistance
V_{EX}	excitation voltage
V_o	output voltage;
f	frequency
$W, W(s)$	transfer function of the high voltage amplifier
$C(s)$	transfer function the Sliding Mode Controller
$H_1(s), H_2(s)$	transfer functions forming the disturbance observer
$A_0(s) \cdots A_3(s)$	transfer functions forming the Sliding Mode Controller
K	gain
ω_n	natural frequency
ζ	damping factor

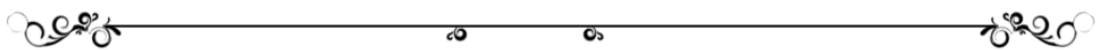


TABLE OF ABBREVIATIONS

ADC	:	Analog to Digital Converter
ASMC	:	Analog Sliding Mode Controller
DAC	:	Digital to Analog Converter
DO	:	Disturbance Observer
DOF	:	Degrees of Freedom
EDM	:	Electric Discharge Machining
EMI	:	Electromagnetic Interaction
FRF	:	Frequency Response Function
HVA	:	High Voltage Amplifier
IC	:	Integrated Circuit
JFET	:	Junction gate Field-Effect Transistor
m	:	Meters (um: micro meter, nm: nanometer, pm: picometer)
MEMS	:	Micro Electromechanical Systems
MIMO	:	Multi Input Multi Output
Op-amp	:	Operational Amplifier
PCB	:	Print Circuit Board
PEA	:	Piezoelectric Actuator
PID	:	Proportional Integral Derivative
PLZT	:	Lanthanum Modified Lead Zirconate Titanate
PSU	:	Power Supply Unit
PVDF	:	Polyvinylidene Fluoride
PZT	:	Lead Zirconate Titanate
SISO	:	Single Input Single Output
SMC	:	Sliding Mode Controller
SNR	:	Signal to Noise Ratio
V	:	Volts (mV: millivolts, uV: microvolts)
VSC	:	Variable Structure Control
VSS	:	Variable Structure System

1 INTRODUCTION

1.1 Motivation

Today, mainly from re-programmability point of view, digital platforms are preferred for the implementation of the control algorithms. Digital solutions offer two very attractive advantages: (1)-promise to shorten design cycles, and (2)-provide the freedom to reprogram the design in simple ways. This ease-of-change stands in sharp contrast to the great effort required to redesign a typical hard-wired analog implementation.

Many important control problems can be effectively solved using a digital architecture in conjunction with analog-to-digital (ADC) and/or digital-to-analog (DAC) conversions that compel extra conditions on the system. Data conversion requirement is not the only disadvantage of such systems; analysis and design methods are more complex for sampled data systems, sampling and resolution can affect the performance, computational delays limit the system bandwidth and degrade accuracy. A less commonly listed disadvantage of digital control is the “software development phase” which is tedious, error-prone, time consuming, and hence expensive.

Looking from control systems perspective, depending on the complexity of the plant and the degrees of freedom (DOF) to be controlled, digital implementation of an algorithm may be demanding due to the high computational power requirement to run in real time or in the case of small systems, an excessive computational power due to the problems of scaling down the digital hardware. Thus, multi-DOF systems may require either diminish in the systems operation frequency or additional hardware to run the algorithm in parallel for each DOF.

This thesis investigates the possibility of designing an *analog motion controller* for single input single output (SISO) systems of complex nature, based on non-linear control methodologies. Research is motivated by the need of a motion controller for a

14-DOF microassembly workstation [1, 2] designed and built in Sabanci University for experimental purposes.

Due to the fact that Sliding Mode Controller (SMC) is claimed to result in superior system performance, which includes insensitivity to parameter variations and almost complete rejection of disturbances, SMC is selected as the controller design framework even though any other nonlinear control strategy could be used. Originally designed as a system motion for dynamic systems whose essential open-loop behavior can be sufficiently modeled with ordinary differential equations, SMC is one of the effective nonlinear robust control approaches that provide system invariance to uncertainties once the sliding mode motion is enforced in the system [3, 4]. An important aspect of sliding mode is the discontinuous nature of the control action, which switches between two values to move the system motion on so-called sliding mode that exist in a manifold and therefore often referred as variable structure control (VSC). The resulting feedback system is called variable structure system (VSS).

As a test bed for the designed system, piezoelectric actuator (PEA), a nonlinear system with hysteresis as major nonlinearity, is selected. PEAs are used in many applications to provide sub-micrometer resolution since they theoretically provide unlimited resolution on a large band of frequency. However, strong hysteretic nonlinear behavior makes PEA control challenging. The previously mentioned microassembly workstation's motion is also based on piezoelectric actuation.

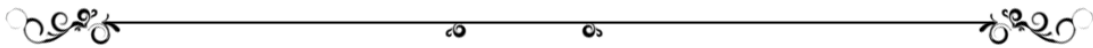
1.2 Objectives of the Thesis

This research is application oriented and aims to develop necessary hardware for an *analog nonlinear motion controller for SISO systems*. The work naturally starts with the selection of an appropriate plant as a test bed and modeling of this plant. The selection of an appropriate nonlinear control framework is the key part of the work since the whole design will be based on this selection. Once the test-plant model is clear and a suitable control framework is known, the design and fine-tune of the controller should be studied by targeting analog application and production possibility. To be followed by the circuit design, the analog controller should be well analyzed to prove the added-value. Finally hardware implementation and real-world experiments should also be studied.

With the design and implementation of this analog controller, we hope to gain an understanding on how to apply analog techniques for system control purposes. Analysis results are generated to gain insight on the implementation.

1.3 Structure of the Thesis

The rest of the thesis is organized as follows; Section II describes the plant and selected model which constitutes a basis for the controller design. The Sliding Mode Controller design together with Disturbance Observer is presented in Section III where circuit application of the algorithm is also depicted with analyses. Section IV presents the experimental results while conclusions and areas for future research are presented in Section V.



2 MODELING AND CONTROL OF PIEZOELECTRIC ACTUATORS

2.1 Piezoelectric Actuation

Piezoelectric effect, or piezoelectricity in brief, is an electromechanical phenomenon which couples elasticity with electricity through the existence of pressure or induced electrical field. This phenomenon was first discovered by Jacques and Pierre Curie brothers in 1880 during their work on quartz crystals and named as the “(direct) piezo effect” where the word “piezo” is derived from the Greek word for pressure. [5].

Later Curie brothers also verified that, an electrical field applied to the crystal, leads to deformation of the material. This effect is referred as the “inverse piezo effect” (or some times converse piezo effect). Since then, research on piezoelectricity has received much attention. However, it took several decades to utilize piezoelectricity; the first commercial applications were ultrasonic submarine detectors developed in 1940’s during World War I, due to the discovery of the barium titanate (BaTiO_3), a piezoelectric ceramic. After that, many researches are conducted on man-made piezoelectric materials, both on fabrication and use.

The (direct) piezoelectric effect results the material to be electrically charged when subject to pressure. Due to this property, piezoelectric materials can be used to “convert” strain, movement, force, pressure, or vibration to electric signals and therefore are widely preferred as detector material. The inverse piezoelectric effect, the ability of the material to become strained due to an electric field, on the other hand, gives the possibility to use those crystals as “actuator” for a range of applications [6].

2.1.1 Daily Use of Piezoelectricity

The piezoelectric effect is very often encountered in daily life both as actuator and/or sensor. The accelerometer for triggering the airbag of the cars during an accident is actually a piece of piezoelectric crystal [5]. In gas lighters, pressure by an impact is applied on a piezoelectric ceramic resulting electric field strong enough to produce a

spark that ignites the gas. Alarm clocks and phone rings often use a piezoelectric element that vibrates at the audible frequency [7].

Piezoelectric materials do also find place in auto-focus cameras [8, 9] and sports materials: “Smart Skis” introduced in 1995, are high-tech snow skis from K2 in Vashon, Washington, with embedded computer controlled piezoelectric actuators damp out shocks and vibrations automatically to provide better stability to the skier [10]. Another application of the smart material technology is used on mountain bikes; ACX engineers used piezoelectric actuators to alter the flow of fluid through a shock bypass port. That way, shock setting provides the optimal damping for the continuously changing terrain and speed during the off-road riding of mountain bike [10].

During the past decade, this material has been extensively used for controlling vibration, noise [11, 12] and shape of a structural system [13]. As an example, in aerospace, the actuator is currently being used to alleviate tail buffeting in aircrafts by NASA [14] and to increase stability in helicopter rotors [12, 14].

Due to the relatively small size and light weight, piezoelectric elements can be integrated in a complex actuator networks such as a robotic system [15]. “Miniman”, a miniaturized robot for micro manipulation by University of Karlsruhe, Germany, with its size 10x10x20mm, can “walk” in the environment by its piezo actuated legs and manipulate its tool holder in 3D space [16-18]. Similar approach is adopted by Kusakawa et al. [19]; their robot is 28mm diameter with a height of 16mm. This small robot of only 16 grams, uses three actuated piezo legs based on the elongation and contraction of the piezoelectric actuators, while Miniman uses bending type piezoelectric actuators for motion. Another micro robot based on bending type actuators is the one developed by Aoyama et al. [20, 21] for micromachining systems. These robots with the size of 30mm in cubic are designed to carry parts to the micromachining stations like drilling, assembling etc.

Other main applications of these ceramics is the scanning tunneling microscope (STM) and atomic force microscope (AFM) [22-24], commonly used in the field of material science for surface visualization at the resolution of atomic size. In those applications, the fixed tip on a system of piezoelectric actuators is supposed to move distances typically 50 Angstroms in parallel and perpendicular to the sample material.

Due to the limited stroke but high resolution of the piezoelectric actuators, they are sometimes used in combination with another actuator; one for coarse motion and piezoelectric actuator for fine motion. For example they act as secondary actuator in hard disk drive head to improve the alignment with data tracks on the disk which increases the data density [25, 26]. Even though in such applications the primary actuator is generally a DC motor, different applications exist. For example Liu et al. worked on piezo-voice coil motor combination [27].

2.1.2 Piezoelectricity for Nanopositioning

Piezoelectric effect is a crystalline effect and therefore piezoelectric actuators do not suffer from “stick slip” effect mainly caused by the friction between elements of a mechanical system. This property theoretically promises an unlimited resolution. However, the achievable resolution in practice can be limited by a number of other factors such as the piezo control amplifier (electronic noise), sensor (resolution, noise and mounting precision) and control electronics (noise and sensitivity to EMI) as will be discussed in further chapters.

In naturally occurring piezoelectric materials, such as quartz, piezoelectric effect is too small to be of practical use. Modern man-made piezoelectric polycrystalline ceramics are much more suitable for actuator and/or sensor purposes. The most popular commercial piezoelectric materials are lead zirconate titanate (PZT), lanthanum modified lead zirconate titanate (PLZT) and polyvinylidene fluoride (PVDF) [6]. Today, the most often used material is PZT and actuators made of this ceramic are often referred as PZT actuators.

To be able to exhibit piezoelectric effect, the crystal structure of the material must possess built-in dipoles that are highly oriented [28]. In other words the crystal structure must be asymmetric. Piezoelectric actuators are generally driven by applying voltage difference to the terminals, causing an electric field on the material which results in elongation or contraction of the material depending on the polarization or depolarization level of the crystal. The maximum permissible electric potential difference is limited by the saturation level of the polarization and/or depolarization. Maximum allowed positive field strength is generally much higher than the permissible negative field strength meaning that the material can elongate more than it can contract.

2.1.3 Major Piezoelectric Actuator Types

Piezoelectric materials have three basic deformation modes: axial, transversal and shear [28] creating three actuator types: the axial actuator, the transversal actuator and the shear actuator. Based on those deformation modes three main types of actuator developed: the bimorph actuator (transversal mode), the tube actuator (transversal mode) and the stack actuator (multilayer, axial mode).

So called “bimorphs” actuators, consists of two piezoelectric plates bonded together and electroded so that their piezoelectric expansion/contraction directions are opposing each another. This actuator will execute a bending motion of several hundred micrometers with the application of an electric field.

The tube actuator consist of bulk ceramic disks, which are 0.4 to 1mm thickness, glued together to form a stack. In this type of actuators, no intermediate electrodes are used; therefore, the required voltage is much higher compare to the other types of actuators.

The maximum electrical field that piezoelectric ceramics can survive is on the order of 1kV/mm. In order to keep the operating voltage within practical limits, some actuators are produced by serial thin layers of piezoelectric ceramic, with typical thicknesses of 20 to 100 μ m, that are stacked physically in series but are connected electrically in parallel (Figure 2.1) [29, 30]. So called the stack actuator is based on the axial mode of the material. The main advantage, beside low-voltage requirement, is the relatively large stroke: the total deformation for piezoelectric actuator is the sum of the expansions of the individual layers.

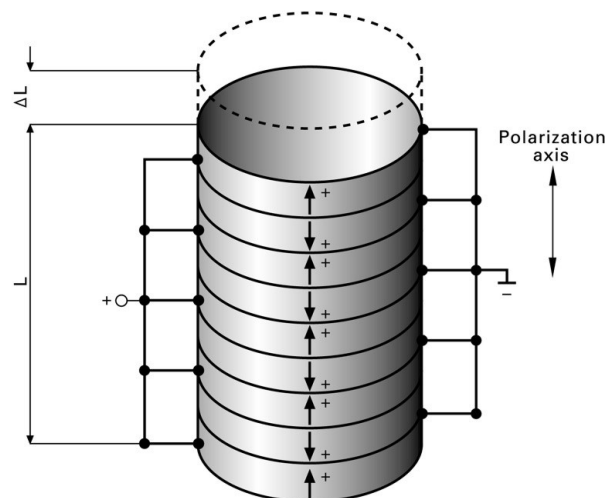


Figure 2.1: Electrical connection of disks in a stack type piezoelectric actuator [7].

Both tube and stack type of piezo actuators can be used in many applications: low-voltage actuators facilitate drive electronics design, but due to manufacturing technology, high-voltage ceramics can be designed with larger cross-sections suitable for higher-load applications.

2.1.4 Features of Piezoelectric Actuators

Until the last few decades the main actuation source used to be the electrostatic and electromagnetic actuators. However, the actuation by piezoelectric actuators gets more and more popular. Comparative properties of electrostatic, electromagnetic and piezoelectric actuators are summarized in Table 2.1 below will help to better understand the causes.

Table 2.1: Comparison of typical actuator properties [31].

Property	Actuator Type		
	Electrostatic	Electromagnetic	Piezoelectric
Volume power	↓	↔	↑
Area efficiency	↓	↔	↑
Volume efficiency	↔	↓	↑
Machinability	↑	↓	↔
Displacement	↓	↑	↔
Frequency response	↔	↓	↑
Displacement accuracy	↔	↓	↑

Legend: (↑) Good, (↔) moderate, (↓) not good.

Main advantage of electromagnetic actuators is their high energy density. Centimeter sized motors can be fabricated without difficulty. Therefore electromagnetic actuators are the dominant ones in conventional use. However, on micro or nano actuation, the volume and weight are very large and the assembling process of permanent magnets is required in fabrication process. So that it is at disadvantage for miniaturization of systems [8].

Electrostatic type of actuators is most widely applied for MEMS (micro electromechanical systems) since the processing method of semiconductors can be used for their fabrication, which is their main advantage. Their energy density is quite small compare to electromagnetic energy density. Moreover, they have the disadvantages of

small displacement, necessity for careful insulation and design of structures with a very large number of comb probes. Therefore, they are also at disadvantage for miniaturization of the systems [8].

Between the scales of centimeters (electromagnetic actuators) and hundreds of micrometers (electrostatic actuators), the demand for powerful actuators can be fulfilled with piezoelectric actuators. At the present the most widely used piezoelectric material is PZT. With additives of doping or acceptor ions, PZT can be modified to be soft type or hard type. Soft PZT materials $[\text{Pb}(\text{Ti}, \text{Zr})\text{O}_3]$ is the mixed solid solution of lead zirconate (PbZrO_3) of ferroelectric (analogous to ferromagnetic) and lead titanate (PbTiO_3) of anti-ferroelectric. [8, 29, 30].

Soft type piezoelectric materials are used to generate large strokes while hard type PZT actuators are used for resonance type actuators like ultrasonic motors. After all, hard type PZT's energy densities is only one order of magnitude above of the soft type PZT's.

Beside the energy density property, piezoelectric actuators have many advantages over electromagnetic and electrostatic actuators. Repeatable nanometer and sub-nanometer steps at high frequency can be achieved with piezoelectric actuators due to the motion derived through solid state crystal effects (molecular effects within the crystalline cells). There are no moving parts accordingly no "stick-slip" effect. Therefore managing displacements in the range of 10pm to 100 μm ($10^{-12} m$ to $10^{-4} m$) is theoretically possible. Due to the same reasons, piezoelectric actuators have also the following useful properties; no maintenance requirement, no lubrication requirement, high-oscillating frequency, less EMI influence and less noise and heat production.

2.1.5 Disadvantages of Piezoelectric Actuators

Along with the fast growing of precision manufacturing industry, high precision and high performance motion is becoming essential. Piezoelectric actuators, based on crystalline effects theoretically provide unlimited resolutions and therefore are widely used in commercial application to provide sub-micrometer resolution. Moreover their high speed, high bandwidth, high stiffness, high electrical-mechanical transformation efficiency and little heat generation properties make them more agreeable in the field.

Although the piezoelectric materials possesses so many advantages, almost all piezoelectric materials are ferroelectric and as all ferroelectric materials they exhibit

fundamental hysteresis phenomena in the polarization versus the applied electric field, as well as in all the material properties coupled to the polarization [7, 23, 25, 26, 32-36].

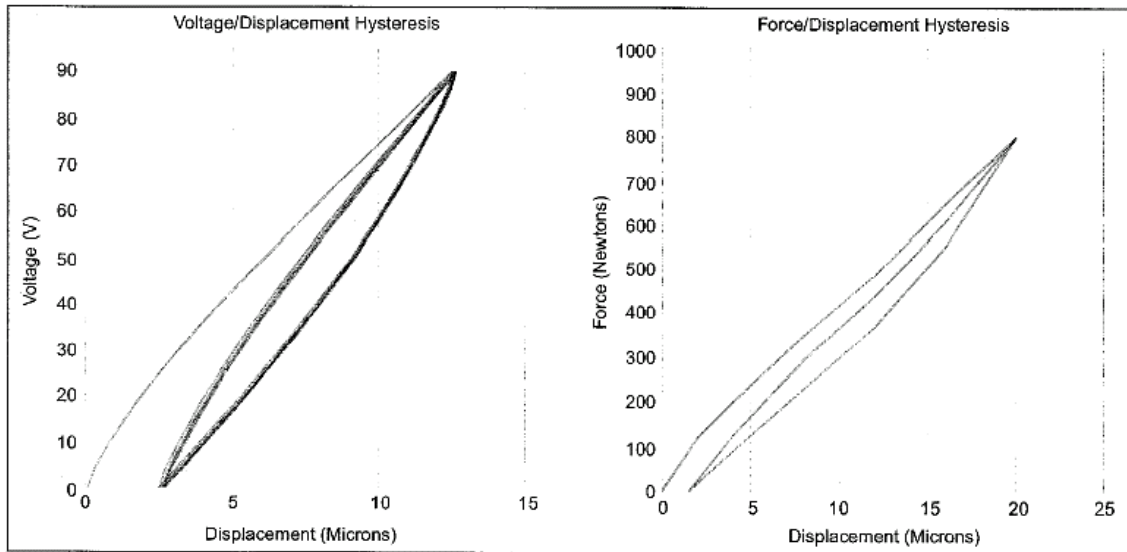


Figure 2.2: Measures hysteresis curves for voltage/displacement and force/displacement relations.

Hysteresis yields a rate-independent lag and residual displacement near zero input (Figure 2.2) [37]. Since the output depends on the input history, for a certain input there is no unique output. Hysteresis is nondifferential, multivalued, and is usually unknown. The existence of hysteresis often limits the performance of the piezoelectric actuator, leads to the severe inaccuracies (up to 10-15% of the traveling path) and causes undesirable oscillation or even instabilities when the piezo actuator is operated in an open-loop manner [38]. Achieving high speed, large-range precision positioning of piezo actuators is therefore challenging [39]. Hence how to design an effective controller for dealing with the hysteretic feature becomes a very important topic.

Another undesired characteristic of piezoelectric actuators is the “creep effect” that can be observed when a step input voltage is applied to the input of the actuator [40, 41]. Figure 2.3 shows a step response of a general stack-type piezoelectric actuator. As seen in the figure, the displacement differs for the same input voltage levels, which clearly shows the hysteresis effect. In addition to hysteresis, we can see the creep effect in each step (magnified view in the circle). It has been known that the creep response has a logarithmic shape over time that can be represented by the following equation [40]:

$$L(t) = L_0 \cdot \left[1 + \gamma \cdot \log_{10} \left(\frac{t}{0.1} \right) \right] \quad 2.1$$

where $L(t)$ is the piezoelectric actuator's displacement for any fixed input voltage, L_0 is a nominal constant displacement value which is the displacement of 0.1s after applying the input voltage, γ is a creep factor which determines the rate of the logarithm. Rates of creep γ are different according to the input voltages. Moreover, even if the final applied voltages are the same, the value of the parameter γ is still different from others according to the past applied voltages.

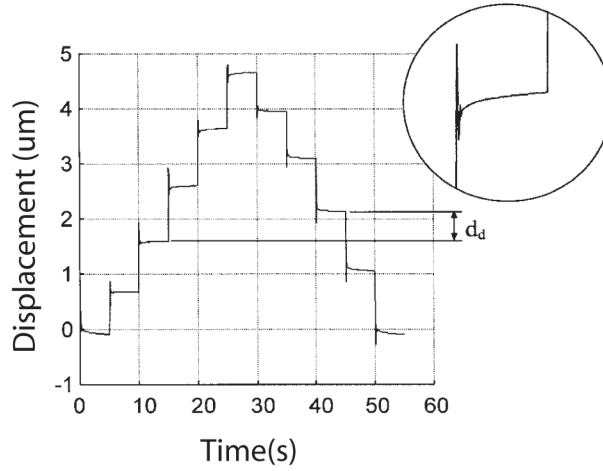


Figure 2.3: Open-loop step response of the piezoelectric actuator. “d” is the displacement difference due to hysteresis. Creep effect is magnified in the circular view [40].

2.2 Piezoelectric Actuator Models

Probably the most known piezoelectric actuator model is the one published by the standards committee of the IEEE in 1987 [42]. This description consists of two linear constitutive relations; the first one describes the mechanical behavior while the second one describes the electrical behavior of the material under *constant* electric field since the model is developed for quasistatic operation.

$$\begin{aligned} T_{ij} &= c_{ijkl}^E \cdot S_{kl} - e_{kij} \cdot E_k \\ D_i &= c_{ikl} \cdot S_{kl} - \varepsilon_{ij}^S \cdot E_k \end{aligned} \quad 2.2$$

where T_{ij} is the stress component (N/m^2), c_{ijkl}^E is the elastic stiffness (N/m^2), e_{kij} and e_{ikl} are the piezoelectric constants (C/m^2), E_k is the electric field (V/m), D_i is the

electric displacement (C/m^2) and S_{kl} is the strain component. In this set of equations the summations run according to Newton rule.

Although this description is the most widely recognized one and still widely used, model derivation on the IEEE linear constitutive relations requires several assumptions, resulting in an oversimplified description that fails to describe the nonlinear behavior present in all piezoelectric ceramics. Yet, they do provide us the basic relationship among strain (S), stress (T), electric field (E) and electric displacement (D) in a piezoelectric material.

The work by Guan and Liao [43] on the other hand, is one of the rare equivalent circuits modeling research for piezoelectric actuators under loaded and unloaded conditions. The work disregards the mechanical domain and summarizes the behavior of the actuator near resonance by two lumped-parameter equivalent circuits in parallel; one representing the non-resonant part and other resonant part. The resonant part is a number of R-L-C (in series) layers placed in parallel (Figure 2.4). Depending on the resonance points obtained by the experiments the number of layer is varied and components of each layer are adjusted to match the frequency.

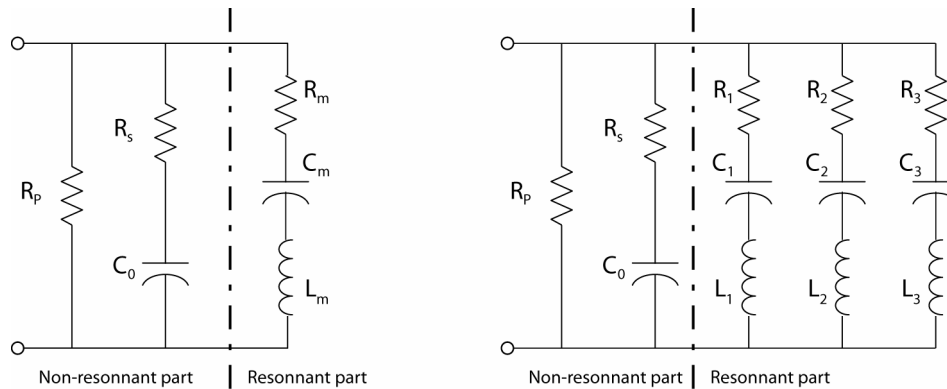


Figure 2.4: Electrical equivalent circuit for piezoelectric actuators; equivalent circuit model for unloaded piezoelectric ceramics on the left and proposed circuit model for the piezoelectric structure on the right [43]

In so called “quasistatic operation”, the operation up to few Hertz, the series resonant circuit (L_m, C_m, R_m) which represents dielectric losses, is canceled out and the piezoactuator is mainly a capacitor [28, 42]. Therefore require very little power in quasistatic operation: just to balance the leakage of current through the internal resistance R_p which is typically on the order of $10M\Omega$, simplifying power supply needs [8]. Even when disconnected from the electrical source, the charged actuator will

not make a sudden move but will very slowly return to its uncharged position. Since in quasistatic operation, piezoelectric devices consume almost no energy, they produce virtually no heat.

2.3 Hysteresis Models

A hysteresis loop is defined as the stationary loop in the input-output plane for a quasistatic monotone oscillating input such as a small frequency sinusoid. In piezoelectric actuators, hysteresis effect depends on many parameters including input amplitude and frequency, and is known to be the dominant nonlinearity. Many researchers have proposed different hysteresis models for piezoelectric ceramics.

Work done in this area can be grouped under two major categories; application of the ferromagnetic hysteresis models to piezoelectric actuators, like Jiles–Atherton model [44], and development of new models.

New model developments are based upon mathematical and logical approximation of the input–output behavior of the material, as for example the Preisach model, the Duhem model, the Generalized Maxwell slip model, and the constant phase lag approximation [34, 37].

Preisach model is constructed from the superposition of the outputs of a set of hysteretic relays. As generally accepted, the Preisach model that implies non recoverable nonlinearities, is superior to the others. However, it is quite long process to identify a Preisach model for a given piezoelectric actuator. A special set of inputs has to be applied to collect corresponding responses in order to calibrate model parameters. Moreover, the model is known to focus only on minor loops of hysteresis under operating voltage well-below saturation [45] and therefore ignores frequency-dependent behavior [46]. Duhem model on the other hand does not give a unique response for a given input, which requires additional algorithm to properly use it. Generalized Maxwell Slip model, first proposed by physicist James C. Maxwell in 1800s, requires many calculations during the control phase, making it computationally costly to apply.

2.4 Control of Piezoelectric Actuators

The use of piezoelectric actuator requires a robust and well designed controller. Although many open-loop controllers based on the hysteresis and creep models are applied in different applications, closed loop control is known to provide better linearity, long-term position stability, repeatability and accuracy.

Piezoelectric actuators can be driven with either of the two inputs: voltage input or charge input. In the early 1980's it has been reported that, in case of charge drive, the hysteresis behavior is reduced [47]. However, we know that, in both driving method a charge is induced on the electrodes of the piezoelectric actuator, generating an electric field, causing the material to elongate or contract which results a displacement. From this information we can conclude that the hysteresis is mainly formed by charge input that creates a voltage difference across the serial impedance to the actuator circuitry as summarized in Figure 2.5.

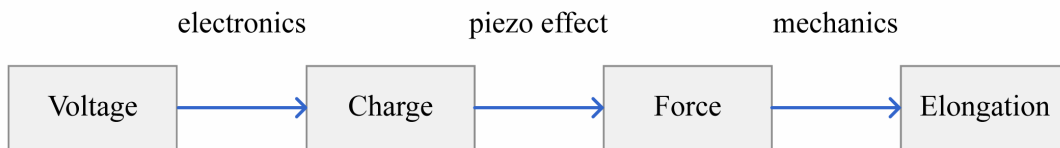


Figure 2.5: Schematic representation of the different representations in a piezoelectric actuator.

From the above information we can conclude that the charge control of the actuator does not avoid the hysteresis, but since this nonlinearity is between the voltage and charge it is now included to the control domain of the current source.

Still some charge control methods are investigated by researchers; however, the difficulties in hardware directed most of the research to voltage steering: a charge drive configuration has to be able to apply the desired charge to the piezoelectric actuator independently from the actuator impedance that is changing. This is completely analog to a current drive configuration that applies constant current independently from the attached impedance [47, 48]. However, in piezoelectric actuators care must be taken since piezoelectric materials do have maximum and minimum voltage limits. Therefore the applied current should have dynamic limits to protect the crystal from damage.

In [48], a current source is directly used for charge steering, while in [47] a simple configuration consisting of a voltage source, an operational amplifier, an external

capacitance, and a high voltage amplifier is proposed. It is known that these configurations have two apparent drawbacks: both sides of the piezoelectric actuator are floating with respect to ground and therefore is very sensitive to op-amp bias current [34].

In voltage steering on the other hand, much effort is done to model the hysteresis with invertible functions that will be used for compensation purposes [23, 30, 34, 36, 37, 46, 49]. The choice of open-loop control is generally shown as a must since the position change measurement in the orders of micrometers requires expensive devices such as LVDT's, laser interferometers etc... However, open-loop techniques have been successful in providing results up to 2% error which is acceptable compare to the 15-20% hysteresis error in the nature of the piezoelectric actuator. Due to the difficulties involved in modeling the actuator precisely, those techniques seem to approach the boundaries.

In [25], disturbance compensation based on a hysteresis model is used. However, unmodeled disturbances required the addition of a robust H_∞ controller. A similar work is done by Tamer and Dahleh [24]. They tried both the H_∞ method with estimated velocity, based on position measurement, and the lead-lag compensation that improves the transient response and steady state error. It is shown that lead-lag control needs frequency dependent feedforward gain, limited by the maximum voltage of the actuator. Experimental results show that although the error boundaries decreased from 8% to 6%, hysteresis is still a problem even at low frequencies. H_∞ control on the other hand gives better tracking and eliminates the high frequency oscillations for the cost of rounding the corners of the triangular waves and noticeable delay increasing with frequency.

In order to design a control scheme that will achieve successful tracking performance without precise dynamic modeling, some fuzzy logic and neural network solutions are presented in the literature. Due to the limited performance, this research area did not find much popularity [38, 50, 51].

Similar learning methods are used to estimate the hysteresis or the disturbance in general, in order to feedforward to the plant under simple PID controller [51-54]. Complexity of the hysteresis being major barrier, makes the design of the neural networks challenging. As a result the systems could barely perform better than model based feedforward controllers.

A similar idea with totally different approach is the hysteresis observer; in contrary to model inversion methods, hysteresis observers continuously predict the disturbance on the system and with a correction term, linearize the plant [55]. Many observers based on different plant and hysteresis models are investigated. Most recent works are by Shieh and Huang [33, 56, 57] and by Lin and Yang [58, 59].

Sliding mode control (SMC) is one of the effective nonlinear robust control approaches. One of the most important aspect of SMC is the discontinuous nature of the control action which switches between two values to move the system motion on so-called “sliding mode” that exist in a manifold. SMC provides system invariance to uncertainties once the system is in the sliding mode [3, 4] and originally designed as system motion for dynamic systems whose essential open-loop behavior can be sufficiently modeled with ordinary differential equations. The discontinuous control action is generally referred as variable structure control (VSC). The resulting feedback system, called variable structure system (VSS), is defined in continuous time domain and governed by differential equations with discontinuous right hand sides.

Bonnail et al. applied VSC on piezoelectric actuated scanning tunneling microscope to precisely follow the sample surface with the feedback of the tunneling current [60]. Compare to the commercial PI controlled motion, their solution shows less oscillating tunneling current due to the better tracking of the surface.

Abidi et al. used SMC in conjunction with the disturbance observer for both position and force tracking in piezoelectric actuators [61, 62]. In their work, they used the lumped parameter model of the piezoelectric actuator to estimate the external disturbances via disturbance observer. Feedforward application of the estimated disturbance improved the results.

Woronko et al. used SMC to control additional degree of freedom added to tool position on conventional CNC turning centers to improve machining precisions [63]. Chiang et al. used adaptive discrete variable structure control to control the piezoelectric actuator mounted on the tip of a pneumatic cylinder. That is how they obtained a large stroke yet precise linear actuation system using adaptive discrete variable structure control.

2.5 Disturbance Observer

A control scheme based on an observer is a highly effective method to improve the performance of the motion control due to its simple structure and it has been widely adopted in the various application areas. Instead of explicitly designing a nonlinear control law to compensate the nonlinearities in the plant, the nonlinearities are treated as disturbances to a linear plant. A disturbance observer (DO) is closed around the control loop to estimate and cancel these terms. Yet the DO is a helpful tool in the motion control system to reject not only the external disturbance but also all internal modeling parameter variations. This way the motion control performance can be greatly enhanced. Moreover the attractiveness of the DO based algorithms lie in their simplicity.

In recent years, disturbance observers have been widely used in realizing high performance and precise motion control systems. Even though there are various proposals to estimate the disturbance, this work uses the DO introduced by Ohnishi et al. [55] for the following reasons [64, 65];

- The amount of calculation is small: a disturbance observer allows for making estimates by considering parameter variation, nonlinear friction, and other disturbances together as one state variable.
- A disturbance observer can be readily built with only a reverse system for the nominal plant and a low-pass filter. As a result, the physical meaning of the parameters of the structural elements can be readily understood.
- A nominal system can be created by feeding back the estimated disturbance.
- The sensitivity to disturbance can be decreased by simply making the disturbance observer of a higher order as necessary.

The conventional motion control system simply consists of a position controller and a disturbance observer as shown in Figure 2.6. Note that this is a SISO system that is represented using the Laplace domain. The position controller, C_f , is usually a PID controller, which is a cascaded form of position and speed controller. In order to enhance the control performance, the DO is adopted to compensate the disturbance.

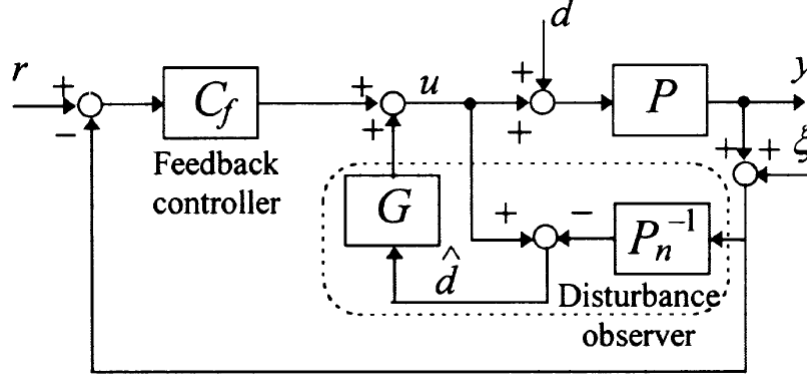


Figure 2.6: Motion Control system with disturbance observer.

P represents the actual plant which is affected by variations in the parameters, r , y , u , and ξ represent the reference input, the plant output, the control input and the observer noise respectively. The DO is the block surrounded by the dotted line; the disturbance d is estimated from the output y and the input u . Here, P_n is the nominal plant, all of whose parameters are known. A system for which P_n has m^{th} order delay can be expressed as follows:

$$P_n = \frac{1}{a_0 s^m + a_1 s^{m-1} + \dots + a_{m-1} s + a_m} \quad 2.3$$

The coefficients a_i of the denominator in polynomial equation 2.3 are generally selected as follows;

$$a_i = 0 \quad (i = 1, \dots, m) \quad 2.4$$

G is defined as the low-pass filter used to make the observer proper. The design of G is shown in equation 2.5 for the disturbance model defined as in equation 2.6

$$G(s) = \frac{g_{m+k-k} s^{k-1} + \dots + g_{m+k-2} s + g_{m+k-1}}{s^{m+k-1} + g_1 s^{m+k-2} + \dots + g_{m+k-1} s + g_{m+k-1}} \quad 2.5$$

$$\hat{d} = \frac{1}{s^k} \quad 2.6$$

Above equations show that the selection of filter G merely depends on the order of the system and on the order of the estimated disturbance model. In general, the step function model, that is $k = 1$, is used. When a disturbance model with $k > 1$ is preferred, the order is higher than in the typical system and consequently called a higher-order DO [64].

2.5.1 Reduced Order Luenberger Observer

There are many possibilities to approach the disturbance estimation and our intention is not to exhaust all possible structures but, by discussing some, to select the most appropriate one to the problem in focus.

The application of the Luenberger observer requires making some assumptions regarding the parameters of the system and the disturbance itself. First disturbance is assumed as bounded and can be modeled as the output of a linear system. Such an assumption allows writing reduced order Luenberger observer for a second order system represented by;

$$m \cdot \ddot{x} + c \cdot \dot{x} + k \cdot x + F_{ext} = F \quad 2.7$$

Assume disturbance force changes slowly relative to the mechanical time constant of the system and therefore the derivative of the disturbance is neglectable. That assumption together with system 2.7 leads to an augmented system;

$$m \cdot \ddot{x} + \underbrace{c \cdot \dot{x} + k \cdot x + F_{ext}}_{F_d} = F \quad 2.8$$

$$\dot{F}_d(x, \dot{x}, t) = 0 \quad 2.9$$

Under assumption that velocity and input force are measurable, reduced order Luenberger observer can be designed by introducing the intermediate variable;

$$z = F_d + l \cdot \dot{x}, \quad l = const > 0 \quad 2.10$$

By taking into account the augmented system 2.8 the dynamics of $z = F_d + l \cdot \dot{x}$ can be written as;

$$\dot{z} = \dot{F}_d + l \cdot \ddot{x} = \frac{l}{m} \cdot (F - z + l \cdot \dot{x}) \quad 2.11$$

since $\dot{F}_d = 0$. Now it is easy to design observer for z just by taking the same structure as in 2.11;

$$\dot{\hat{z}} = \frac{l}{m} \cdot (F - \hat{z} + l \cdot \dot{x}) \quad 2.12$$

By taking Laplace transformation of 2.12, one can easily find

$$\hat{z} = \frac{(l/m)}{s + (l/m)} (F + l \cdot sx) = Q(s) \cdot (F + l \cdot sx), \quad Q(s) = \frac{(l/m)}{s + (l/m)} \quad 2.13$$

Where $Q(s)$ is a low pass filter with corner frequency defined by design parameter l/m . Just by plugging 2.13 into 2.10, estimated disturbance can be expressed in the form

$$\hat{F}_d = Q(s) \cdot F - l \cdot (1 - Q(s)) \cdot sx \quad 2.14$$

Under the condition $l = m \cdot g$ the structure can be rearranged to the following form

$$\hat{F}_d = \frac{g}{s + g} \cdot F - \frac{g \cdot s}{s + g} \cdot m \cdot sx = \frac{g}{s + g} \cdot (F - a \cdot s^2 x) = Q(s) \cdot F_d \quad 2.15$$

The reduced order Luenberger observer is providing estimation of the disturbance $F_d = c \cdot \dot{x} + k \cdot x + F_{ext}$ modified by simple first order filter $Q(s) = \frac{g}{s + g}$. If one requires constant bandwidth of the low pass filter, then the gain of the observer must depend on the system inertia. If the system inertia is not known than this requirement cannot be met.



3 DESIGN AND IMPLEMENTATION

This research mainly focuses on the analysis and control of piezoelectric actuators using Sliding Mode Controller for analog circuit application as a final target. The organization of the rest of the text is as follows; we will first study the plant and present the selected piezoelectric actuator model together with the nonlinearity model namely the hysteresis. Next we will present the Sliding Mode Control as it is applied in this work followed by the disturbance observer design. Analog application of the control and disturbance observer is studied; therefore the subsequent section will discuss the requirements, design criterion and application of the Sliding Mode Control algorithm in electronics. The last part summarizes the analysis used either in the design process or after the design has been established.

3.1 Modeling Piezoelectric Actuator

Discussed in previous sections, different models for piezoelectric actuators exists, with most based on IEEE standard [42]. Modeling strategies are bounded to fail if only the actuator displacement is taken into account and not the force. A complete model should include the coupled displacement and force variables of the actuator. In 1997, Goldfarb and Celanovic proposed a model that is completely based on physical principles and that uses Maxwell slip model for the hysteresis realization [36]. This model consists of an electrical and a mechanical domain, as well as the connection between the two domains. Even though this model describes well the linear dynamical aspects and the hysteresis nonlinearity, the hysteretic behavior description requires serious computation. Based on Maxwell slip model, the hysteresis calculation requires a serious number of slip elements to increase calculation accuracy.

As a useful ability, the model allows simple means to include different nonlinearity models. The hysteresis model used by Adriaens et al. [34] and by Banning et al. [35] together with the electromechanical model proposed by Goldfarb and Celanovic is known to give good performance, even though it is mainly tested for

ferromagnetically soft materials by Coleman and Hodgdon [34, 35] in 1986. This combination is also used and validated by Abidi et al. [61, 62].

According to the Goldfarb-Celenovic model, the piezoelectric actuator consists of an electrical and a mechanical model connected to each other by an appropriate conversion constant called “the piezoelectric effect constant”. The model is summarized on Figure 3.1 where $H(q)$ is the hysteresis effect as a function of charge q , h the voltage due to this effect, T is the piezoelectric effect conversion constant, C represents the capacitance, \dot{q} is the total current flowing through the circuit (q may be seen as the total charge in the piezoelectric actuator), q_p is the transduced charge from the mechanical side, u_p is the voltage due to the piezo effect, u is the total voltage over the piezoelectric actuator, F_p is the transduced force from the electrical side while F_{ext} is the externally applied force and finally x is the elongation of the piezoelectric actuator.

The mechanical relation between F_p and x is denoted by M that compromise equivalent mass m , spring k , and damping c . Note that we have equal electrical and mechanical energy at the ports of interaction, i.e. $u_p \cdot q_p = F_p \cdot x$.

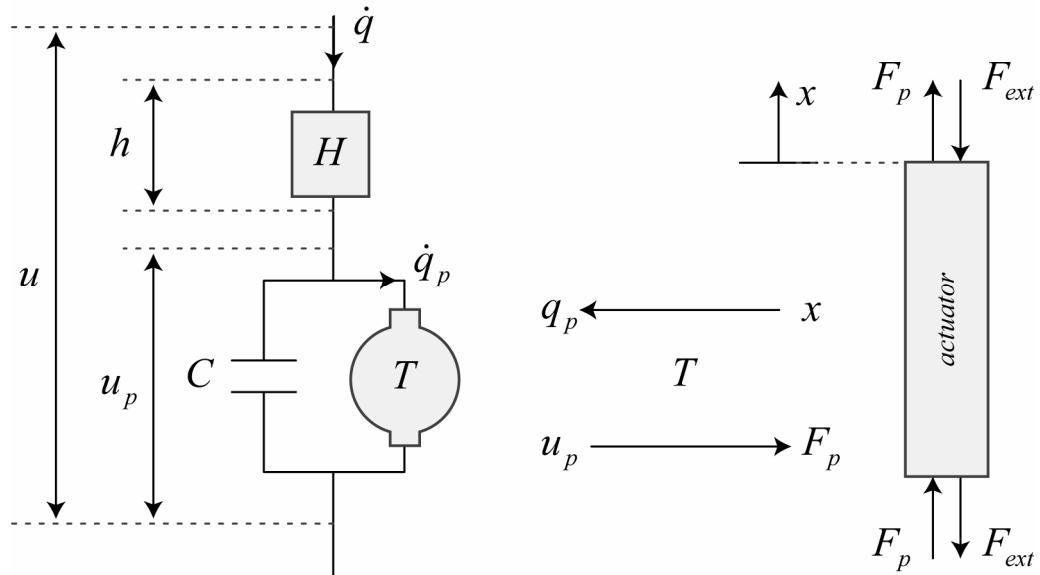


Figure 3.1: Electromechanical model of the piezoelectric actuator.

The lumped parameters of the piezoelectric actuator; m , c and k can be calculated in terms of the piezoelectric ceramic properties: elasticity modulus E ,

viscosity η , mass density ρ and physical properties like physical length L and cross-sectional area A of the wafers as follows:

$$m = \rho AL \quad c = \frac{\eta A}{L} \quad k = \frac{EA}{L} \quad 3.1$$

Parameters for the lead zirconate titanate (PZT) material are presented on Table 3.1. Though, it will be safer to experimentally measure those values using FRF (Frequency Response Function) analysis, since due to the production phase, aging and operation temperature, some of the parameters may drift and/or differ.

Table 3.1: Material properties for lead zirconate titanate (PZT), the piezoelectric crystal of the used actuator for the experiments in this work.

Property	Symbol	Value
Elasticity modulus	E	$6.6 \cdot 10^{10} \text{ N / m}^2$
Viscosity	η	10mPa.s
Mass density	ρ	7800 kg / m^3

The complete electromechanical model, which can also be described by the block diagram given in Figure 3.2, is mathematically formulated by 6 equations;

$$u_p = u - h \quad 3.2$$

$$h = H(q) \quad 3.3$$

$$q = C \cdot u_p + q_p \quad 3.4$$

$$q_p = T \cdot x \quad 3.5$$

$$F_p = T \cdot u_p \quad 3.6$$

$$m \cdot \ddot{x} + c \cdot \dot{x} + k \cdot x = F_p - F_{ext} \quad 3.7$$

System defined by equations 3.2 to 3.7 can be evaluated further for state space representation. First of all 3.3 is inserted in 3.2 that is also inserted in 3.6 to obtain;

$$F_p = T \cdot (u - H(q)) \quad 3.8$$

Then this equation must be replaced in 3.7. The resultant equation can be written as;

$$m \cdot \ddot{x} + c \cdot \dot{x} + k \cdot x = T \cdot [u - H(q)] - F_{ext} \quad 3.9$$

This equation can easily be rewritten in state space form;

$$\begin{aligned}
\dot{x}_1 &= \dot{x} = x_2 \\
\dot{x}_2 &= \ddot{x} = -\frac{k}{m} \cdot x_1 - \frac{c}{m} \cdot x_2 + \frac{T}{m} \cdot u - \left(\frac{T}{m} \cdot H(q) + \frac{F_{ext}}{m} \right) \\
\dot{x}_2 &= \ddot{x} = -\frac{k}{m} \cdot x_1 - \frac{c}{m} \cdot x_2 + \frac{T}{m} \cdot u - dist
\end{aligned} \tag{3.10}$$

This is a second order time invariant single input single output (SISO) system with disturbance represented by the term ‘*dist*’.

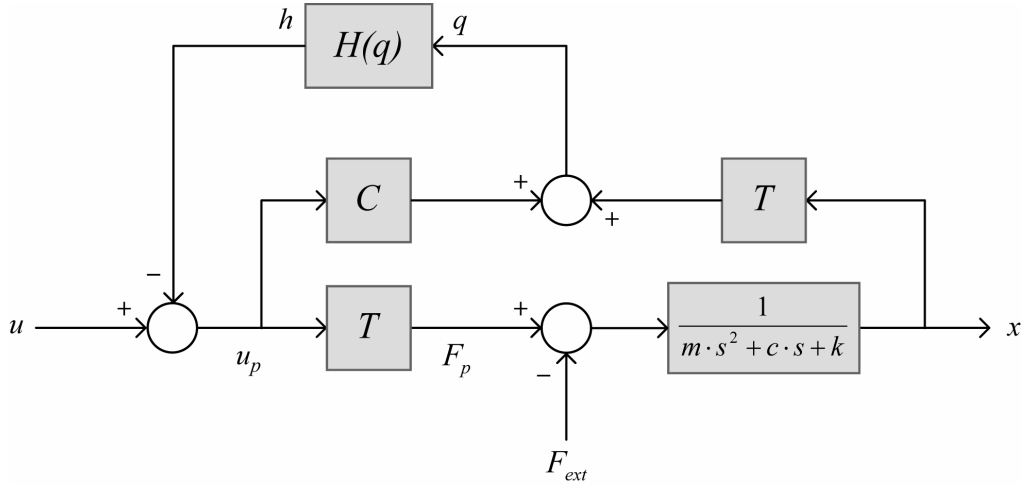


Figure 3.2: Block diagram representation of the electromechanical model.

3.2 Hysteresis Model

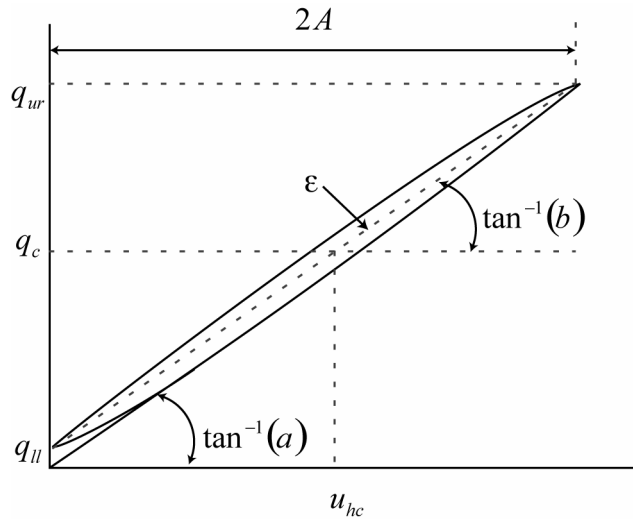


Figure 3.3: Example hysteresis loop and its characteristics [26].

Goldfarb-Celenovic model summarizes the electromechanical model of the piezoelectric actuator and includes the hysteresis as function of charge flowing to the actuator. For the modeling of this hysteresis effect we will use the model proposed by

Coleman and Hodgdon [34, 35] initially developed for magnetic hysteresis. It has been proven that the model is also suitable for describing the electrical hysteresis [61, 62].

According to the model, the relation between the hysteresis voltage h and charge flowing to the actuator q is given by;

$$\dot{q} = \alpha \cdot |h \cdot (f(h) - q)| + \dot{h} \cdot g(h) \quad 3.11$$

where $f(h)$ and $g(h)$ are functions defining the shape of the hysteresis loop, shown in Figure 3.3, and α is a constant.

It has been shown that the center point of the hysteresis loop is given by $q_c = f(u_{hc})$, where u_{hc} is the average voltage applied to the actuator by the sinusoidal input, and the average slope of the loop is given by $g(u_{hc})$, where q_c is corresponding average charge to u_{hc} .

Although piezoelectric actuators have a physical stroke limit, in practice the operation point is kept away from those boundaries. Accordingly, the hysteresis loop having the shape shown in Figure 3.3 can be defined by two shaping functions selected as;

$$\begin{aligned} f(h) &= a \cdot h \\ g(h) &= b \end{aligned} \quad 3.12$$

where a and b are constants. Then using the equation for the center point and the average slope, those two constants can be determined from the following equalities;

$$\begin{aligned} q_c &= a \cdot h \\ q_{ur} - q_{ll} &= b \cdot 2A \end{aligned} \quad 3.13$$

where q_{ll} and q_{ur} are respectively the lower left and upper right points of the hysteresis loop and $2A$ is the maximum input amplitude.

In order to determine the third parameter α in the model of the hysteresis, a relation for the area of the hysteresis loop, ε , is derived for small amplitude of the sinusoidal input;

$$\varepsilon = \frac{4}{3} \cdot (a - b) \cdot \alpha \cdot A^3 \quad 3.14$$

Remark that the hysteresis area represents the amount of energy spent by the system [35] and therefore ε corresponds to the lost of the energy in the system.

In order to find the values of the variables a , b and α one must analyze the behavior of the piezoelectric actuator for small amplitude, moderate frequency sinusoidal input: $h(t) = \tilde{u} + A \cdot \sin(\omega \cdot t)$ where \tilde{u} is the offset, A is the amplitude and ω is the angular frequency of the input. First of all \tilde{u} is slowly varied and q_c vs. \tilde{u} is plotted. The fitting of the line $q_c = a \cdot \tilde{u}$ will give the value for a . Similarly, varying A and plotting slope of the hysteresis loop vs. $h(t)$ will yield a line parallel to the horizontal axis whose value is equal to b . Finally the hysteresis area loop vs. $h(t)$ is plotted for various amplitudes A and then α is determined from the plot since a and b are known in equation 3.14.

3.3 Model Parameters

Model parameters are mainly defined from the datasheet of the piezoelectric actuator used in experiments and from previous work by Abidi et al. [61, 62] as the same actuator was used in that work. Some other parameters are determined with experiments and the values are refined by trial and error. Since robust control techniques will be used exact knowledge of parameters is not crucial. The used piezoelectric actuator is PSt 150/5/60 VS10 type from Piezomechanik SVR with datasheet information presented on Figure 3.4. Nominal values for plant parameters are presented on Table 3.2 as they are used in the next sections.

Table 3.2: Nominal values for plant parameter used in this work [26]

Parameter	Nominal Value
m_N	$9.24 \cdot 10^{-4}$ kg
c_N	685 N.s/m
k_N	$8 \cdot 10^6$ N/m
T_N	3.9 N/V
C	$2.4 \mu F$
a	5
b	4.5
α	1.8

Type	max. stroke μm	length L mm	el. capacitance nF	stiffness N/ μm	resonance frequency kHz
PSt 150/5/7 VS10	13/9	19	350	50	40
PSt 150/5/20 VS10	27/20	28	800	25	30
PSt 150/5/40 VS10	55/40	46	1600	12	20
PSt 150/5/60 VS10	80/60	64	2400	8	15
PSt 150/5/80 VS10	105/80	82	3200	6	12
PSt 150/5/100 VS10	130/100	100	4000	5	10

Figure 3.4: Datasheet for the piezoelectric actuator: PSt 150/5/60 VS10.

3.4 Sliding Model Control

The Sliding Mode Control is an effective robust control to deal with parameter uncertainties and disturbance for nonlinear systems; it is widely used for the nonlinear control scheme. The major problem with the classical SMC is that the control input that shows high frequency oscillations, resulting in a problem known as chattering. The chattering involves extremely high control activity and increase power consumption. In addition, produces undesirable high frequency dynamics.

One of the most common solutions to chattering problem is the boundary layer approach. The SMC with the boundary layer consists of a smooth function instead of the sign function. However this method has some side effects. First, the boundary layer thickness has the trade-off relation between control performance of sliding controller and chattering migration. Second, within the boundary layer, the characteristics of robustness and the accuracy of the system are no longer assured. Another method for cancelling the chattering problem is the high order SMC that requires complex calculation.

When the continuity of input signals to the plant is an important design criterion, the classical method fails. For example, if the input to the system is current, a fast oscillating signal cannot be tolerated. Therefore a method which can assure continuous control signals becomes desirable.

In this work, SMC design methodology is used to arrive a controller that has very small discontinuous component or in some cases no discontinuous component at all, if the exponential convergence to sliding mode manifold is acceptable. In addition, the structure is kept as simple as possible in order to allow analog implementation with limited hardware. The aim is in this later stage is to try to integrate a whole controller as

a part of the high voltage amplifier needed to supply the PEA. Using Lyapunov stability theorem, the stability of the control strategy is proven.

3.4.1 Definitions

In the controller design we will consider dynamical systems that can be represented as a class of nonlinear systems, linear with respect of control as described by the following equation;

$$\dot{x} = f(x) + B(x) \cdot u + d \quad 3.15$$

where $x^T \in \mathfrak{R}^n$ is the state vector, $u \in \mathfrak{R}^m$ is the control vector, $f(x) \in \mathfrak{R}^n$ is an unknown, continuous and bounded nonlinear function, $B(x) \in \mathfrak{R}^{n \times m}$ is a known input matrix whose elements are continuous and bounded and $rank(B(x))|_{\forall x} = m$, with $d \in \mathfrak{R}^n$ being an unknown, bounded external disturbance. It is assumed that both $f(x) \in \mathfrak{R}^n$ and $d \in \mathfrak{R}^n$ satisfy the matching conditions and all their components are bounded $\|f_i(x)\|_{\forall x} \leq M$ and $\|d_i(t)\|_{\forall t} \leq N$. Fully actuated mechanical systems belong to the class of systems described by 3.15. Such systems can be interpreted as m interconnected sub-systems $\ddot{x}_i = h_i(x_i, \dot{x}_i) + b_i(x_i, t) \cdot u_i + g_i(x_i, x_j)$, $h_i(x_i, \dot{x}_i)$ in general represents Coulomb friction term, $g_i(x_i, x_j)$ represents the interaction term and is regarded as a disturbance.

The aim is to determine the control input $u = [u_1, \dots, u_m]^T$ such that the system states $x_1(t), \dots, x_n(t)$ track the desired trajectories $x_{d_1}(t), \dots, x_{d_n}(t)$ while control error satisfies selected dynamic requirements. In other words, derive the states of the system into the set S defined by;

$$S = \{x : G \cdot (x_d - x) = \sigma(x, x_d) = 0\} \quad 3.16$$

where $\sigma(x, x_d)$ is the function defining the sliding manifold.

3.4.2 Controller Design

The controller will be designed in the SMC framework by firstly selecting a suitable sliding manifold S that will ensure desired systems dynamics and then selecting control such that the Lyapunov stability conditions are satisfied. Selecting the Lyapunov function candidate in terms of the sliding function σ is a natural way of

guaranteeing the sliding mode existence on the selected manifold and thus having desired closed loop dynamics. For a selected candidate Lyapunov function $V(\sigma)$, Lyapunov stability conditions are satisfied and therefore the equilibrium as the $\sigma = 0$ is globally asymptotically stable, if;

- $V(\sigma)$ is positive definite,
- $\dot{V}(\sigma)$ is negative definite,
- $V(\sigma) \rightarrow \infty$ as $\|\sigma\| \rightarrow \infty$

Therefore the necessary control input should be selected such that the requirements of the Lyapunov stability criteria are fulfilled.

3.4.2.1 Sliding Manifold

For system 3.15 the natural selection of the sliding manifold is in the following form

$$S = \{x : \sigma(x, x_d) = G \cdot e_t = 0\} \quad 3.17$$

where tracking error vector is defined as $e_t = [e_1, \dots, e_n]^T \in \mathfrak{R}^n$, $e_i = x_{di} - x_i$ and the sliding surface satisfies $\sigma = [\sigma_1, \dots, \sigma_m]^T \in \mathfrak{R}^m$, $G \in \mathfrak{R}^{m \times n}$.

3.4.2.2 Computation of the Necessary Control Action

A Lyapunov Function candidate can be selected as

$$V = \frac{1}{2} \sigma^T \sigma \quad 3.18$$

where, $V \in \mathfrak{R}$, $V(0) = 0$. The time derivative of the candidate Lyapunov function \dot{V} should be negative definite. In order to use this condition in selection of the control, we may require that \dot{V} satisfies some preselected form. Equating the time derivative of this function to a negative definite function like in 3.19,

$$\dot{V} = -\sigma^T \cdot \left(D\sigma - \mu \frac{\sigma}{\|\sigma^T \sigma\|} \right) \quad 3.19$$

where D is a positive definite symmetric matrix and $\mu > 0$ thus Lyapunov conditions are satisfied. By substituting 3.19 into 3.18, the following requirement is found;

$$\sigma^T \cdot \left(\dot{\sigma} + D\sigma + \mu \frac{\sigma}{\|\sigma^T \sigma\|} \right) = 0 \quad 3.20$$

Therefore, for $\sigma \neq 0$, the control law can be calculated by satisfying the following equation;

$$\dot{\sigma} + D\sigma + \mu \frac{\sigma}{\|\sigma^T \sigma\|} = 0 \quad 3.21$$

and the sliding mode conditions are satisfied. The discontinuous term can be selected as small in order to avoid chattering. It had been proven [66, 67] that in the discrete time implementation the sliding mode is guaranteed with continuous control action. Since the analog application, with continuous signals, is targeted, the discontinuous term $\mu \cdot \sigma / \|\sigma^T \sigma\|$ can be omitted and the control action that satisfies conditions $(\dot{\sigma} + D\sigma) = 0$ can be determined. This will result in quazi-sliding mode behavior of the system with exponential convergence defined by selection of matrix D . If that convergence is fast enough, then the motion of the system will be in an ε -vicinity of the $\sigma = 0$ for most of the time and the reaching stage will be governed by the equation $(\dot{\sigma} + D\sigma) = 0$. All further analysis can be easily adopted for application of expression 3.21 if the term $D\sigma$ is replaced with $D\sigma + \mu \cdot \sigma / \|\sigma^T \sigma\|$.

Starting with the derivative of the sliding function and using 3.15;

$$\dot{\sigma} = G(\dot{x}^r - \dot{x}) = G\dot{x}_d - G\dot{x} \quad 3.22$$

$$\dot{\sigma} = \underbrace{G\dot{x}_d - Gf}_{GBu_{eq}} - GBu(t) = GB \cdot (u_{eq} - u(t)) \quad 3.23$$

If $(GB)^{-1}$ exists, for system 3.15 with sliding mode manifold 3.16, the control that satisfies $(\dot{\sigma} + D\sigma) = 0$ can be determined as

$$u = -(GB)^{-1}(G \cdot (f + d - \dot{x}_d) - D\sigma) = u_{eq} + (GB)^{-1} D\sigma \quad 3.24$$

where $x_d = [x_{d_1}, \dots, x_{d_n}]$ and u_{eq} is so-called equivalent control obtained as a solution of the equation

$$\dot{\sigma} = GB \cdot (u_{eq} - u) = 0 \quad 3.25$$

3.4.2.3 Equations of Motion

By substituting u_{eq} from this last equation 3.25 and from 3.24 into 3.15, the equations of motion of system 3.15 in and outside of the manifold 3.16 are obtained respectively;

$$\begin{aligned}
 \dot{x} &= f + B \cdot u_{eq} + d \\
 \dot{x} &= f - B \cdot (GB)^{-1} \cdot G \cdot (f + d - \dot{x}_d) + d \\
 \dot{x} &= +\dot{x}_d \Rightarrow \sigma = 0
 \end{aligned} \tag{3.26}$$

For the approaching of the sliding surface the following equation of motion can be obtained;

$$\begin{aligned}
 \dot{x} &= f + B \cdot u_{eq} + B \cdot (GB)^{-1} \cdot D\sigma + d \\
 &= f - B \cdot (GB)^{-1} \cdot G \cdot (f + d - \dot{x}_d) + B \cdot (GB)^{-1} \cdot D\sigma + d \\
 &= +\dot{x}_d + B \cdot (GB)^{-1} \cdot D\sigma \\
 \Rightarrow -(\dot{x}_d - \dot{x}) &= -\dot{\sigma} = G^{-1} \cdot D\sigma \\
 \Rightarrow -G\dot{\sigma} &= -\dot{\sigma} = D\sigma \\
 \Rightarrow D\sigma + \dot{\sigma} &= 0
 \end{aligned} \tag{3.27}$$

The role of the equation 3.27 is to drive the system states to the sliding surface $\sigma = 0$. This will result in quazi-sliding mode behavior of the system with an exponential convergence defined by selection of matrix D . If that convergence is fast enough then the motion of the system will be in an ε -vicinity of the $\sigma = 0$ for most of the time and the reaching stage will be governed by the $(D\sigma + \dot{\sigma}) = 0$. In the cases where asymptotic convergence is not acceptable, all above analysis can be easily adopted with the term $D\sigma$ replaced by $D\sigma + \mu\sigma / \|\sigma^T \cdot \sigma\|$. Then the approach to the solution will be governed by equation $\dot{\sigma} + D\sigma + \mu\sigma / \|\sigma^T \cdot \sigma\|$.

3.4.2.4 Discrete Time Implementation

In equation 3.24, the resulting control action is continuous (the equivalent control is continuous and function $\sigma = \sigma(x, t)$ is continuous by assumption) and $u = u_{eq}$ for $\sigma = 0$. In the implementation of the algorithm 3.24, full information about system dynamics and external disturbances is required mainly for the equivalent control calculation and therefore this algorithm is not practical for application. Yet it is used here as intermediate result to show the procedure in the development of simpler and

more useful control strategies. From $\dot{\sigma} = GB \cdot (u - u_{eq})$ equivalent control can be substituted into 3.24 to obtain;

$$u = u + (GB)^{-1} \left[D\sigma + \frac{d\sigma}{dt} \right] \quad 3.28$$

Even though the written form of this equation is not usual, it is very informative; it shows that in order to force the system to reach ε -vicinity of the selected sliding mode manifold S and to stay within ε boundary layer, the control input should be modified by the term $(GB)^{-1} \left[D\sigma + \frac{d\sigma}{dt} \right]$ at every instant of time.

For a discrete time system with no computational delay, the relations between the measured and computed variables are depicted in Figure 3.5 below. T shown on the figure is the sampling time of the digital system; kT represents the current control cycle, $kT + T$ is the next cycle while $kT - T$ is the previous one.

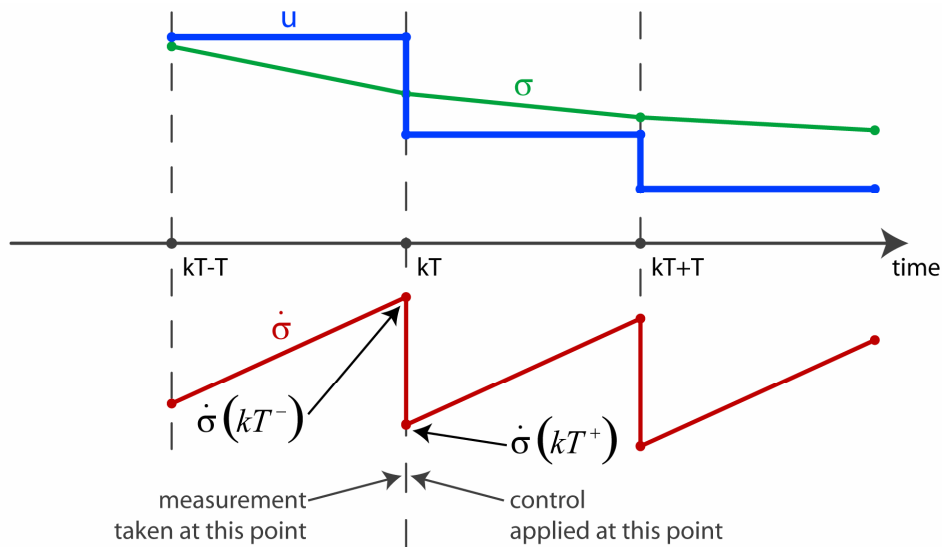


Figure 3.5: The relations between measured and calculated variables for discrete time systems without computational delay.

The measurements are taken before the calculation of the new control value input and therefore are denoted as $\bullet(kT^-)$. All variables immediately after the application of the new control input are denoted by $\bullet(kT^+)$. Remark that for all continuous functions and variables $\bullet(kT^-) = \bullet(kT^+)$. Then 3.28 can be rewritten as,

$$u(kT^+) = u(kT^-) + (GB)^{-1} \left[D\sigma(kT^-) + \frac{d\sigma(kT^-)}{dt} \right] \quad 3.29$$

Control 3.29 is suitable for implementation since it only requires measurement of the sliding mode function and value of the control applied in the preceding step. Obviously, derived from the continuous time equations with discrete time approximations, above control law will introduce errors that must be analyzed carefully.

3.4.2.5 Stability in Discrete Time Implementation

The stability should be analyzed both at the moment the control input is applied and at the end of the corresponding sampling time interval. By calculating the derivative of function $\sigma(x, t)$ at $t = kT^+$ one can obtain;

$$\frac{d\sigma(kT^+)}{dt} = \frac{\partial\sigma(kT^+)}{\partial t} + \frac{\partial\sigma(kT^+)}{\partial x} \cdot \frac{\partial x}{\partial t} = \frac{\partial\sigma(kT^+)}{\partial t} - G \cdot (f(kT^+) + B \cdot u(kT^+)) \quad 3.30$$

Replacing $u(kT^+)$ from 3.29 into 3.30 it follows;

$$\frac{d\sigma(kT^+)}{dt} = \frac{\partial\sigma(kT^+)}{\partial t} - G \cdot \underbrace{[f(kT^+) + B \cdot u(kT^-)]}_{\frac{d\sigma(kT^-)}{dt}} - D\sigma(kT^+) - \frac{d\sigma(kT^-)}{dt} \quad 3.31$$

since both σ and f are continuous by assumption and therefore $\sigma(kT^-) = \sigma(kT^+)$ and $f(kT^-) = f(kT^+)$.

$$\frac{d\sigma(kT^+)}{dt} = -D\sigma(kT^+) \quad 3.32$$

This shows that at the moment immediately after new control is applied, in other words at the beginning of the sampling interval, the stability conditions are satisfied. For $t \in [kT, kT + T]$ the control input u is constant. Similarly it can be proven that the maximum deviation from the sliding surface both at and between each sampling instance is on the order of sampling time square, $O(T^2)$.

3.4.2.6 Continuous Time Implementation and Stability

Implementation of the control 3.24 in continuous time domain on the other hand, requires information about the plant dynamics and external disturbances, which is hard to achieve. In addition, this solution needs the information on the equivalent control

thus may be applied for the plants when u_{eq} is known or can be estimated with sufficient accuracy. In this work we will be using a fact proven in [68] that the solution of the differential equation

$$\tau \dot{z} + z = \left(u - (GB)^{-1} \cdot \dot{\sigma} \right) \quad 3.33$$

with small enough filtering time constant τ is close to the equivalent control. In this work we will be using this result in order to avoid direct calculation of the equivalent control from $u_{eq} = -(GB)^{-1} G(f + d - \dot{x}_d)$ but instead to use approximated result $u_{eq} = z$;

$$z = \frac{g}{s + g} \cdot u - K \cdot \frac{g}{s + g} \cdot s\sigma \quad K = (GB)^{-1} \quad 3.34$$

The above equation could be used as it is, but it requires the calculation of the derivative for σ . The derivative operation is known to amplify the high frequency components existing in a signal which contains non-continuous elements, namely noise. Calculation of $s\sigma$ will contain second derivative of the error, since σ is already a function of the derivative of the error, and this operation will result in over noised signal. The calculation of $s\sigma$ can be easily avoided by the use of a simple mathematical fact;

$$\frac{s}{s + g} = 1 - \frac{g}{s + g} \quad 3.35$$

Now the above equation can be written as;

$$z = \frac{g}{s + g} \cdot (u + K \cdot g \cdot \sigma) - K \cdot g \cdot \sigma \quad 3.36$$

Using $u_{eq} = z$ and 3.24 the applied control $u = z + KD \cdot \sigma$ can be calculated;

$$u = \frac{g}{s + g} [u + K \cdot g \cdot \sigma] - K \cdot (g + D) \cdot \sigma \quad 3.37$$

Control 3.37 is suitable for analog implementation since it requires measurement of the sliding mode function and control, yet ideally gives stable motion in manifold $S = \{x : G \cdot e_t = \sigma(x, x_d) = 0\}$. Design parameters D and C should be selected as high as possible in order to achieve fast transients.

3.4.2.7 Approximation Error

The error ε_{ueq} due to the approximation $u_{eq} = z$ can be directly calculated;

$$\begin{aligned}\varepsilon_{ueq} &= u_{eq} - z = [u + K \cdot D \cdot \sigma] - \frac{g}{s + g} \cdot [u - K \cdot s \sigma] \\ \varepsilon_{ueq} &= \frac{s}{s + g} \cdot [u + K \cdot D \cdot \sigma] \\ \varepsilon_{ueq} &= \frac{s}{s + g} \cdot u_{eq}\end{aligned}\tag{3.38}$$

For large g , the error in equivalent control due to the approximation mainly consists of the high frequency part of the un-approximated equivalent control. Using this result, it can be shown that the tracking error due to the control approximation error is bounded. For large g , the estimation error is small, yet as $g \rightarrow \infty$ then $(u_{eq} - z) \rightarrow 0$; so the approximated system behaves close to the ideal.

The effect of this calculation in tracking errors can be calculated using the equation of motion for the system under control $u = u_{eq} + K \cdot D \cdot \sigma$ and $u_{app} = z + K \cdot D \cdot \sigma$. The derivation with the calculation of the error ε_u between the approximated (u_{app}) and un-approximated (u) controls;

$$\varepsilon_u = u - u_{app} = \varepsilon_{ueq} \quad \Rightarrow \quad u_{app} = u - \varepsilon_{ueq}\tag{3.39}$$

Then this control is substituted into 3.15 to calculate the equations of motion of system in manifold S can be obtained;

$$\begin{aligned}\dot{x} &= f + B \cdot u_{app} - B \cdot \varepsilon_{ueq} + d \\ \Rightarrow B \cdot \varepsilon_{ueq} &= B \cdot K \cdot D \sigma + (\dot{x}_d - \dot{x}) \\ \Rightarrow \varepsilon_{ueq} &= K \cdot (D \sigma + \dot{\sigma})\end{aligned}\tag{3.40}$$

Therefore, as the system approaches the sliding surface, the effect of the approximation approaches zero, so the approximated system behaves close to the ideal: $\dot{\sigma} + D \sigma = 0$.

3.5 Estimation of Disturbance for PEA

The accepted model for the PEA, as summarized in section 3.1, is a second order time invariant SISO system. The structure of the observer is based on 3.9 under the

assumption that all the plant parameter uncertainties, nonlinearities and external disturbances can be represented as a lumped disturbance.

The possible parameter variations of the system presented in this equation can be written as $\bullet = \bullet_N + \Delta \bullet$ (where \bullet represents the parameter, \bullet_N its nominal value and $\Delta \bullet$ its deviation from \bullet_N) and therefore be included into the disturbance term “*dist*”.

$$\begin{aligned} m &= m_N + \Delta m \\ c &= c_N + \Delta c \\ k &= k_N + \Delta k \\ T &= T_N + \Delta T \end{aligned} \quad 3.41$$

The displacement of the plant x and the input to the plant u are measurable or accepted to be known. Hence, the nominal structure of the plant is found as;

$$\begin{aligned} m_N \cdot s^2 x &= T_N \cdot u \\ &- T_N \cdot h + \Delta T \cdot (u - h) - \Delta m \cdot s^2 x - (c_N + \Delta c) \cdot s x - (k_N + \Delta k) \cdot x - F_{ext} \end{aligned} \quad 3.42$$

$$m_N \cdot s^2 x = T_N \cdot u - F_d \quad 3.43$$

where;

$$F_d = T_N \cdot h + \Delta T \cdot (h - u) + \Delta m \cdot s^2 x + \Delta c \cdot s x + \Delta k \cdot x + c_N \cdot s x + k_N \cdot x \quad 3.44$$

is the disturbance on the system. Now that the above equation matches the system defined by 2.3 and 3.15 we can proceed as proposed by section 2.5; the disturbance defined by 3.42 can be calculated as;

$$F_d = T_N \cdot u - m_N \cdot s^2 x \quad 3.45$$

Then the estimated disturbance can be written as the inverse plant model multiplied by a low pass filter [55];

$$\hat{F}_d = G(s) \cdot (T_N \cdot u - m_N \cdot s^2 x) \quad 3.46$$

where \hat{F}_d is the observed disturbance force, $G(s)$ is the a filter of suitable order. Since x and u are measurable, \hat{u} , the correction to be added to the control output of the controller to compensate for the disturbance, can then be calculated as

$$\hat{u} = \frac{\hat{F}_d}{T_N} = G(s) \cdot \left(u - \frac{m_N}{T_N} \cdot s^2 x \right) \quad 3.47$$

Equation 2.5 shows that for a system of second order ($m = 2$) with first order DO ($k = 1$), a second order low pass filter is required. Yet second derivative for the position x is required. To simplify the requirement we will be using the same fact 3.35 used in previous sections. This way it will be possible to use a first order filter. The efficiency will also be proven in this section.

One can determine \hat{u} as;

$$\hat{u} = \frac{g}{s+g} \cdot u - \alpha \cdot sx + \alpha \cdot \frac{g}{s+g} \cdot sx \quad 3.48$$

where $\alpha = \frac{m_N \cdot g}{T_N}$ and $G(s) = \frac{g}{(s+g)}$. In real applications the velocity is usually calculated from the position measurement using first order filter to obtain $s \cdot x \approx \frac{s \cdot g_v}{(s+g_v)} \cdot x$. That approximation leads to the calculation of disturbance as;

$$\hat{u} = \frac{g}{s+g} \cdot u - \alpha \cdot \left(1 - \frac{g}{s+g}\right) \cdot \frac{g_v}{s+g_v} \cdot x \quad 3.49$$

It is now clear that the filter $G = g/(s+g)$ could have higher corner frequency than the velocity measurement filter $s g_v/(s+g_v)$.

For the implementation of the structure, the observer should be analyzed: plant and the control correction term can be rewritten as;

$$m_N \cdot s^2 x = T_N \cdot u - F_d \quad 3.50$$

$$\hat{u} = \frac{g}{s+g} \cdot u - \frac{m_N \cdot g}{T_N} \cdot \left(1 - \frac{g}{s+g}\right) \cdot sx = G \cdot u - \frac{m_N \cdot g}{T_N} \cdot (1-G) \cdot sx \quad 3.51$$

Since $u = u_0 + \hat{u}$ the following simplification will help in next steps;

$$u \cdot (1-G) = u_0 - \frac{m_N \cdot g}{T_N} \cdot (1-G) \cdot sx \quad 3.52$$

Inserting this last equation into 3.45 one obtain,

$$m_N \cdot sx \cdot (s+g) = \frac{T_N \cdot u_0}{(1-G)} - F_d \quad 3.53$$

Simplifying this equation and using $G = g/(s+g)$ yields;

$$\begin{aligned}
m_N \cdot sx \cdot (s + g) \cdot (1 - G) &= T_N \cdot u_0 + (G - 1) \cdot F_d \\
\Rightarrow m_N \cdot s^2 x &= T_N \cdot u_0 + (G - 1) \cdot F_d
\end{aligned}
\tag{3.54}$$

Therefore the selection of filtering transfer function G should be selected as close to 1 as possible in order to completely remove the disturbance. The observer implementation is best described by Figure 3.6. For the case where $G \approx 1$, the positive feedback of \hat{u} would, ideally, force the system to behave close to an ideal system defined by

$$m_N \cdot s^2 x = T_N \cdot u_0(t) \tag{3.55}$$

where $u_0(t)$ is the control output from the Sliding Mode Controller. However, in reality the dynamics of the observer would lead to differences between the real disturbance and the estimated disturbance.

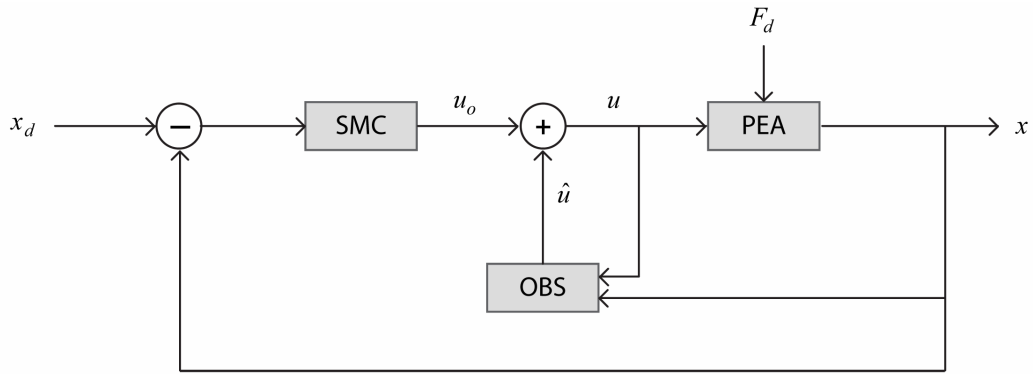


Figure 3.6: Observer implementation.

3.6 Reduced Order Luenberger Observer

The disturbance estimation can also be proven by designing a modified version of the reduced order Luenberger observer as demonstrated in section 2.5.1. The calculations are not repeated in this section but modifications are presented.

The reduced order Luenberger observer is providing estimation of the disturbance $F_d = c \cdot \dot{x} + k \cdot x + F_{ext}$ modified by simple first order filter $Q(s) = \frac{g}{s + g}$. If one requires constant bandwidth of the low pass filter then the gain of the observer must depend on the system inertia and if the system inertia is not known than this requirement cannot be met. In the plant model, the mass is assumed to be bounded but

unknown quantity expressed in the form $m = m_N \pm \Delta m$ where $m_N > 0$ stands for so-called nominal value, Δm stands for bounded variation of the mass. Since only m_N is known, the structure of the observer 2.12 in actual implementation should use m_N instead of $m = m_N \pm \Delta m$. Then 2.12 becomes

$$\dot{\hat{z}} = \frac{l}{m_N} \cdot (F - \hat{z} + l \cdot \dot{x}) \Rightarrow \hat{z} = \frac{(l/m_N)}{s + (l/m_N)} \cdot (F + l \cdot sx) \quad 3.56$$

The structure of observer is not changed. Hence the estimated disturbance can be expressed in the same form $\hat{F}_d = Q(s) \cdot F - l \cdot (1 - Q(s)) \cdot sx$. By taking $l = g \cdot m_N$, inserting 3.56 and 2.8 into $\hat{z} - l \cdot sx = \hat{F}_d$ the output of the observer becomes as in 3.57

$$\begin{aligned} \hat{F}_d(s) &= Q(s) \cdot F - g \cdot m_N \cdot (1 - Q(s)) \cdot sx \\ \hat{F}_d(s) &= Q(s) \cdot (F - m_N \cdot s^2 x) = Q(s) \cdot (c \cdot sx + k \cdot x + F_{ext} + \Delta m \cdot s^2 x) = Q(s) \cdot F_d \end{aligned} \quad 3.57$$

It appears that by changing the parameters of the observer, the proposed structure is able to estimate a linear combination of the disturbance and the parameter's variation. Just by changing the convergence term $l = g \cdot m$ or $l = g \cdot m_N$ the output of the observer is either

$$\hat{F}_d(s) = Q(s) \cdot (c \cdot sx + k \cdot x + F_{ext}) \quad 3.58$$

or

$$\hat{F}_d(s) = Q(s) \cdot (c \cdot sx + k \cdot x + F_{ext} + \Delta m \cdot s^2 x) \quad 3.59$$

respectively.

Implementation of structure 3.58 or 3.59, under assumption that velocity is measured, can be rearranged to the form that does not require information on acceleration

$$\begin{aligned} \hat{F}_d &= Q(s) \cdot F - m_N \cdot g \cdot (1 - Q(s)) \cdot (sx) \\ &= Q(s) \cdot (F + (sx) \cdot m_N \cdot g) - (sx) \cdot m_N \cdot g \\ &= Q(s) \cdot (F - m_N \cdot s^2 x) \end{aligned} \quad 3.60$$

The topology is already depicted in Figure 3.6 and is very widely used in the motion control systems literature [55]. This implementation is very simple and straight forward. For the case of piezoelectric actuator, if $F = T_N \cdot u$ and \ddot{x} are available then

just by applying filter $Q(s)$ as depicted one can estimate the disturbance. In this structure the selection of filter $Q(s)$ is not anymore limited by the structure of the observer. Assumption on slow change of disturbance with respect to the mechanical time constant (as it is in the case of reduced order Luenberger observer) is not required. Selection of filter may give a degree of freedom to adjust the behavior of the system.

3.7 Design Considerations

The controller design presented so far posses two inputs; one for reference and one for the actual position measurement and two outputs; the tracking error (for performance measurements) and the control input that will be connected to the plant trough the voltage amplifier. This controller is designed to operate at relatively high frequencies. Therefore the selection of the operational amplifiers, filtering elements and the power supply is crucial.

The hearth of the circuit is the operational amplifier. Operational amplifiers (op-amps) are highly stable, high gain DC difference amplifiers. Since there is no capacitive coupling between their various amplifying stages, they can handle signals from zero frequency (DC signals) up to a few MegaHertz. Their name is derived by the fact that they are used for performing mathematical operations on their input signal(s).

Since the plant uses high voltage and op-amps generally runs on much lower voltages, another constraint in the design is to have appropriate signal levels for op-amps and plant. This is achieved via having a computation stage running on low voltage power supply unit (PSU) and a separate high voltage amplifier (HVA) stage amplifying the previous stage's output to the desired voltage level for the plant. Moreover this approach allows the controller to work with different plants that need different supply voltages by simply changing the high voltage amplifier.

For mathematical operations, TLE074, a quad, low-noise JFET input op-amp by Texas Instruments, is used. The JFET-input operational amplifiers in the TLE07x series have low input bias and offset currents and fast slew rate. The low harmonic distortion and low noise make the TLE07x series ideally suited for high-fidelity applications. Main characteristics are presented in Table 3.3.

Table 3.3: TLE074 electrical characteristics [69].

	Parameter	Min	Typical	Max	Units
V_{IO}	Input offset voltage		3	10	mV
I_{IO}	Input offset current		5	100	pA
I_{IB}	Input bias current		65	200	pA
V_{ICR}	Common-mode input voltage range	-11...+11	-12...15		V
A_{VD}	Large-signal differential voltage amplification	25	200		V/mV
B_1	Unity-gain bandwidth		3		MHz
r_i	Input resistance		1012		Ohm
CMRR	Common-mode rejection ratio	70	100		dB
SR	Slew rate at unity gain	5	13		V/us
t_r	Rise-time overshoot factor		0.1		us
V_n	Equivalent input noise voltage (f = 1 kHz)		18		nV/\sqrt{Hz}
I_n	Equivalent input noise current		0.01		pA/\sqrt{Hz}
THD	Total harmonic distortion		0.003%		
VCC± = ±15 V, Ambient Temp 25°C (unless otherwise noted)					

For high voltage amplifier stage on the other hand, the MP108 by Apex Microtechnology is preferred. The 300kHz power bandwidth and 10A current output of the MP108 makes it a good choice for piezo drive applications. This power op-amp is a surface mount constructed component built on a thermally conductive but electrically insulating substrate that can be mounted to a heat sink. Main characteristics are presented in Table 3.4

Since the operation at relatively high frequencies is targeted, both the low voltage (or signal) PSU and high voltage (or driving) PSU should be able to supply enough current to drive the plant at the required frequencies. Moreover, since piezoelectric actuators are very sensitive to voltage oscillations, instead of high frequency switching supplies, transformer type power supplies should be preferred.

Table 3.4: MP108 electrical characteristics [70].

	Parameter	Min	Typical	Max	Units
V _{IO}	Input offset voltage		1	5	mV
I _{IO}	Input offset current			50	pA
I _{IB}	Input bias current			100	pA
V _{ICR}	Common-mode input voltage range		-V _B + 15 ... +V _B - 15		V
	Open-loop gain @ 15Hz	96			dB
B ₁	Unity-gain bandwidth		10		MHz
	Power bandwidth		300		
r _i	Input resistance	1011			Ohm
CMRR	Common-mode rejection ratio	92			dB
SR	Slew rate at unity gain	150	170		V/us
	Noise		10		μV RMS
VCC \pm = ± 15 V, Ambient Temp 25°C (unless otherwise noted)					

3.8 Circuit Design

Following the derivation in previous sections, the analog controller should calculate the control u from the two inputs; desired trajectory x_d and the actual trajectory x . The implementation requires a manifold selection as a starting point;

$$\sigma = G \cdot e_t = G \cdot \begin{bmatrix} e_1 \\ e_2 \end{bmatrix} = [C \quad 1] \cdot \begin{bmatrix} x_d - x \\ \dot{x}_d - \dot{x} \end{bmatrix} = C \cdot e + \dot{e} \quad 3.61$$

where tracking error vector is defined as $e_t = [e_1 \quad e_2]^T \in \mathfrak{R}^2$ with $e_1 = e = x_d - x$ and $e_2 = \dot{e}_1 = \dot{e} = \dot{x}_d - \dot{x}$.

Now that the sliding surface is defined the control equation 3.37 must be broken to sub-equations that can separately be applied using op-amp circuits. In the application phase the inverting behavior of the op-amp topologies must also be taken into account. Therefore below sub-equations are formulated according to that requirement;

$$e = -(-x_d + x) \quad 3.62$$

$$\dot{e} = -s \cdot (-x_d + x) \quad 3.63$$

$$-\sigma = -(C \cdot e + \dot{e}) \quad 3.64$$

$$\varphi = \frac{g}{s+g} [u + K \cdot g \cdot \sigma] = -\frac{g}{s+g} [(-u) + K \cdot g \cdot (-\sigma)] \quad 3.65$$

$$-u = -[\varphi + (K \cdot (g + D)) \cdot (-\sigma)] \quad 3.66$$

The addition of the DO can similarly be divided into sub-equations as shown below. With the addition of the DO, the sub-equation 3.66, that is calculating the control output to feed to the high voltage amplifier, is revised to include the control correction term \hat{u} from the DO.

$$-\alpha \cdot \dot{x} = \underbrace{\frac{m_N \cdot g}{T_N}}_{\alpha} \cdot \frac{g_v}{s+g_v} \cdot sx \quad 3.67$$

$$\psi = -\frac{g}{s+g} \cdot [(-\alpha \cdot \dot{x}) + (-u)] \quad 3.68$$

$$-u = -[\varphi + K \cdot (g + D) \cdot (-\sigma) + (-\alpha \cdot \dot{x}) + \psi] \quad 3.69$$

φ , $-\alpha \cdot \dot{x}$ and ψ are used as intermediate signals to simplify the topology. Now each equation 3.62 to 3.69 can easily be applied using op-amp topologies.

The operation of the structure and circuit design summarized in Figure 3.7 can be described as follows; the position measurement x is subtracted from the desired position x_d using op-amp U1 to calculate the tracking error e . U2 has similar operation but it also includes a derivation behavior to calculate \dot{e} . Op-amp U3 is used to sum up those two signals with appropriate weights to calculate the sliding function $-\sigma$. In next stage, the signals $-u$ from the output is fed forward together with $-\sigma$ to U4 where they are summed and filtered to output an intermediate signal φ .

In parallel, the first derivative of the position measurement is calculated using U6 and the summation of this value with $-u$ is filtered in U7. As a final stage U5 sums up all calculated values with appropriate weight to form the control output $-u$ that is fed to the high voltage amplifier.

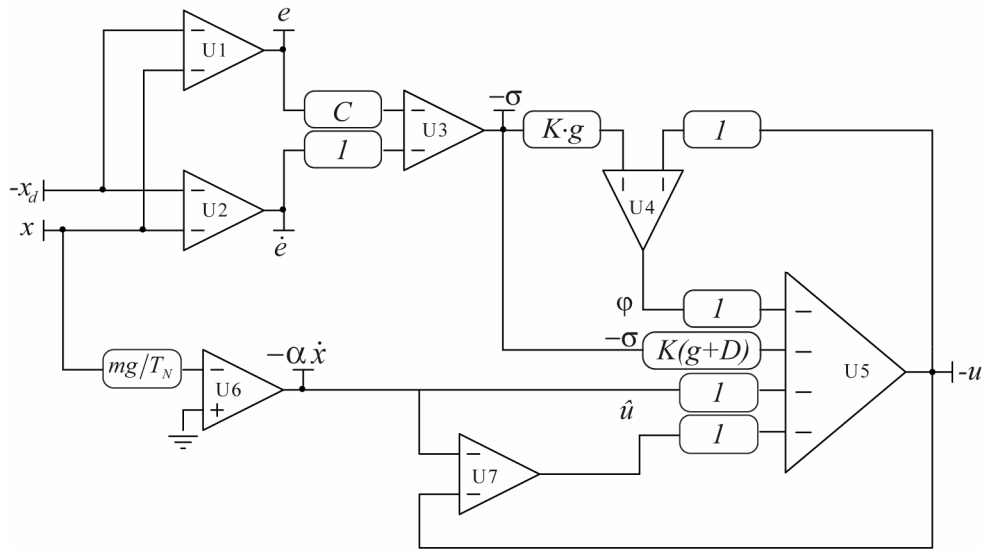


Figure 3.7: General scheme of the controller.

Sections below discuss and analyze the scheme in detail. However, so-called “scaling” should be discussed prior to the circuit operations since it constitutes a key point in the application: in an analog circuit, all signals must fall within the full-scale voltage span of the used operational amplifiers; otherwise part of the signals might have been lost. This requires appropriate voltage scaling to assure that each variable utilizes the available voltage span effectively. The discussion starts with the analog scaling and since position measurement is important part of the controller, continues with the position measurement information.

3.8.1 Analog Computing and Scaling

An analog computer is a form of computer that uses electrical phenomena to model the problem being solved. Created in the years following World War II, analog computers were based on electronic versions of the mechanical differential analyzers. The heart of the analog computer is the operational amplifier (op-amp) and op-amps can be combined to solve linear differential equations with constant coefficients. The analog computer was once the leading-edge tool for dynamic simulation and vibration analysis.

Analog computers produce continuous signals and there is no concept of sample-rate. The computed variables are differentiable but not quantized. All computations take place simultaneously, continuously and in real-time; there are no operation sequence issues to be dealt with and therefore all variables are always current and available. These characteristics are very desirable in a simulation or modeling tool, as well as in control.

However, the analog computer has some severe restrictions on its computations. All computed variables must fall within the full-scale voltage span of the machine's amplifiers. This requires appropriate voltage scaling to assure that each variable utilizes the available voltage span effectively. And the precision of any coefficient is ultimately determined by the tolerance of components within the computer.

Due to the finite range of values which can be processed by an analog computer, it is necessary to scale the equations to be solved in order to avoid overloading the operational amplifiers and thus introducing erroneous terms. Coupled differential equations are normally quite difficult to scale since it is challenging to estimate maximum values for the variables.

The output of each amplifier should be proportional to the problem variable that it represents. The constant K relating the two is called the scaling factor. To determine an appropriate value for K , the maximum value of the problem variable is needed to be estimated. Assuming that this estimate is available, when the problem variable reaches its maximum value, then the amplifier output will be at its maximum value which is the supply voltage of the operational amplifiers. Therefore the scale factor K is formally defined as;

$$K = \frac{\text{Amplifier Supply Voltage}}{\text{Max. Value of the Problem Variable}} \quad 3.70$$

When maximum values are estimated and scale factors are selected, the next step is to make the computer circuit consistent with the original problem equations. An expression giving a scaled amplifier output in terms of the scaled inputs is called a "scaled equation". To calculate the scaled equations of a problem, each and every equation is written down with the program variables replaced by the scaled variables multiplied by scales. For example the variable x with estimated maximum value X should be written as $X \cdot [x/X]$. The term in the bracket represents the scaled variable. Solving the equations for the scaled outputs in terms of the scaled inputs will yield the scaled equations.

3.8.2 Designed Control and Scaling

The analog controller that is designed has strong similarities with the analog computers; even though it is not designed to solve differential equations, it consists of operational amplifiers and therefore suffers from the same disadvantages. Therefore the

designed control's equations needs to be scaled with the assumed maximum values for the signals and parameters that are presented on the Table 3.5. The scaling of the equations used in the controller is shown below.

Table 3.5: Assumed maximum values for signals and parameters.

Parameter	Determined Value	Signal	Assumed Max Value
C	~ 300	e	0.05V
D	~ 20	\dot{e}	1.00V
K	~ 0.2	$\sigma, u, \alpha \cdot \dot{x}$	1.00V

$$e = x_d - x \Rightarrow \left[\frac{e}{0.05} \right] = 20 \cdot \left(\left[\frac{x_d}{1} \right] - \left[\frac{x}{1} \right] \right) \quad 3.71$$

$$\dot{e} = \dot{x}_d - \dot{x} \Rightarrow \left[\frac{\dot{e}}{1} \right] = \left(\left[\frac{\dot{x}_d}{1} \right] - \left[\frac{\dot{x}}{1} \right] \right) \quad 3.72$$

$$\sigma = C \cdot e + \dot{e} \Rightarrow \left[\frac{\sigma}{1} \right] = C \cdot 0.05 \cdot \left[\frac{e}{0.05} \right] + \left[\frac{\dot{e}}{1} \right] \quad 3.73$$

Above equations are equivalent to the previously stated equations since we have always substituted equivalent expressions. But it guarantees that the signals will be in the range of the amplifiers unless the expected maximum values are exceeded. To obtain problem variables, one must rescale those values according to the obtained equations. Equations missing in the above list are the ones that does not require scaling due to their expected maximum value falling in the full scale voltage span of the op-amps.

3.8.3 Position Measurement

In this work, a PEA that consists of a piezo-drive integrated with a sophisticated flexure structure is used. The flexure structure is wire-EDM-cut and is designed to have zero stiction and friction. Flexure stages are also insensitive to shock and vibration. The piezoelectric actuator has two built-in strain-gages for position measurement. The working principles of the strain gage are presented on next section.

3.8.3.1 Strain Gage

Strain ε is the amount of deformation of a body due to an applied force. More specifically, is defined as the fractional change in length L ; $\varepsilon = \Delta L/L$ and can be

positive (tensile) or negative (compressive). While there are several methods of measuring strain, the most common is with a strain gage.

Strain gage is a long and very thin metallic strip arranged in a zigzag pattern on so called backing. When the shape of the backing changes due to the motion of the specimen it is mounted on, the resistance of the strip changes. It is very important that the strain gage be properly mounted onto the test specimen so that the strain is accurately transferred from the specimen, through the adhesive and strain gage backing, to the foil itself.

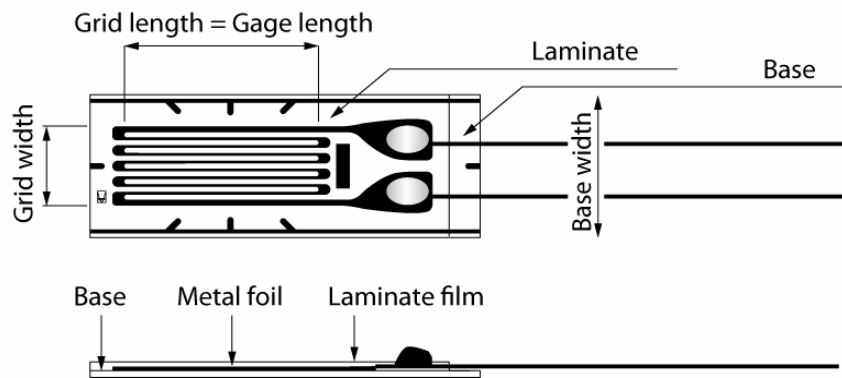


Figure 3.8: An example strain gage.

A fundamental parameter of the strain gage is its sensitivity to strain, expressed quantitatively as the gage factor GF : the ratio of fractional change in electrical resistance to the fractional change in length (strain);

$$GF = \frac{\Delta R/R}{\Delta L/L} = \frac{\Delta R/R}{\varepsilon} \quad 3.74$$

If the nominal resistance of the strain gage is designated as R , then the strain-induced change in resistance, ΔR , can be expressed as $\Delta R = R \cdot GF \cdot \varepsilon$. Strain gages are commercially available with different nominal resistance values with 120, 350, and 1000 Ω being the most common values.

Ideally, the resistance of the strain gage is liked to change only in response to applied strain. However, strain gage material, as well as the specimen material to which the gage is applied, will also respond to changes in temperature. Manufacturers attempt to minimize thermal sensitivity by processing the gage materials. Other compensation methods exist.

To measure such small changes in resistance, strain gages are mounted in the same direction as the strain and often in groups of two or four to form a half or a full “Wheatstone Bridge” respectively. The general Wheatstone Bridge, illustrated in Figure 3.9, consists of four resistive arms with an excitation voltage V_{EX} , and the output voltage;

$$V_o = \left[\frac{R_3}{R_3 + R_4} - \frac{R_2}{R_1 + R_2} \right] \cdot V_{EX} \quad 3.75$$

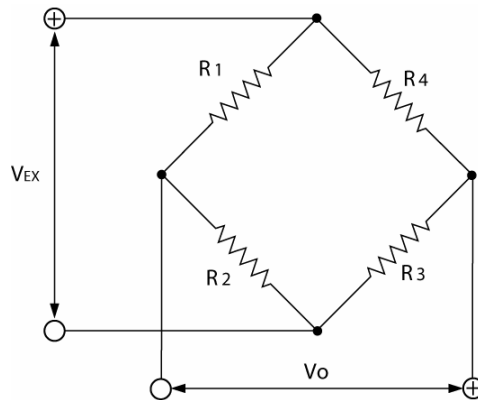


Figure 3.9: The Wheatstone Bridge.

From this equation, it is apparent that when $\frac{R_1}{R_2} = \frac{R_4}{R_3}$ the voltage output V_o will be zero. Under these conditions, the bridge is said to be balanced. Any change in resistance in any arm of the bridge will result in a nonzero output voltage. Therefore if one of the resistances is replaced by a strain gage, any changes in the strain gage resistance will unbalance the bridge and produce a nonzero output voltage. The sensitivity to strain can be doubled by making both gages active in a half-bridge configuration. As an example, Figure 3.10 illustrates a bending beam application with one bridge mounted in tension ($R + \Delta R$) and the other mounted in compression ($R - \Delta R$). This half-bridge configuration, whose circuit diagram is also illustrated in Figure 3.10, yields an output voltage that is linear and approximately doubles the output of the quarter-bridge circuit. Finally, the sensitivity can further be increased by making all four of the arms of the bridge active strain gages in a full-bridge configuration.

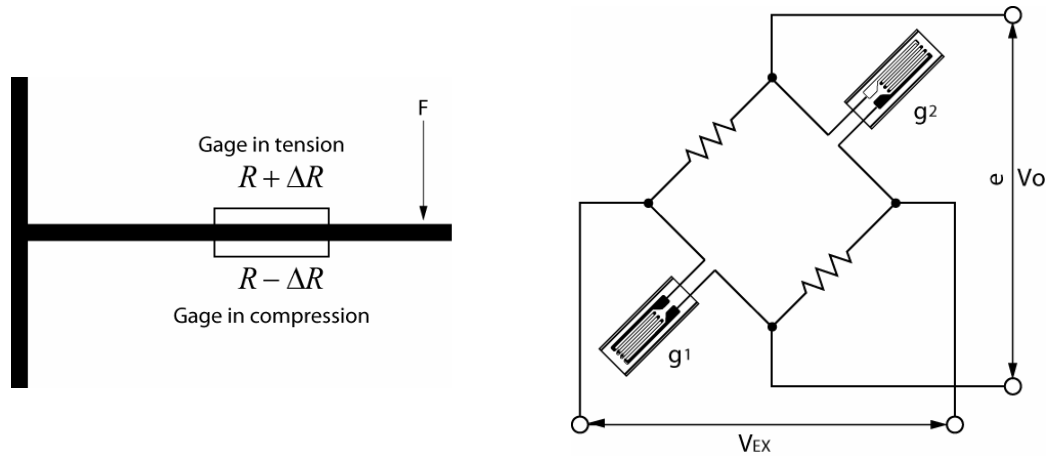


Figure 3.10: (Left) Bending beam example with two strain gages installed. (Right) Bridge configurations for two gages measurements.

The equations, given above, assume an initially balanced bridge that generates zero output when no strain is applied. In practice however, resistance tolerances and strain induced by gage application will generate some initial offset voltage. This initial offset voltage is typically nulled with a voltage shift circuit.

3.8.3.2 Position Measurement for PEA

The used PEA in this work has two built-in strain-gages for position measurement. Being installed in parallel, two strain gages allow doubling the measurement precision through half-bridge configuration shown in Figure 3.10.

However, proactive strain gage measurement requires certain signal processing beside the simple Wheatstone Bridge configuration. Those include noise filtering, bridge balancing (offset nulling) and calibration. Therefore, instead of designing and building a so called strain gage amplifier, an industry standard compliant amplifier is used; SCM5B38-03 wide band strain gage amplifier from Dataforth Corporation. The amplifier has 100kHz signal bandwidth, 100dB common mode rejection ration and $\pm 0.03\%$ accuracy according to the datasheet supplied by the manufacturer.

As a result of the full stroke measurement experiments it is determined that, for the sample piezoelectric actuator, $17.96\mu\text{m}$ (micrometers) elongation (or contradiction) corresponds to 1V of the strain gage amplifier reading, or in other words $1\mu\text{m}$ position deflection results 55.68mV and 1nm (nanometers), $55.68\mu\text{V}$.

3.8.4 Electronics Structure

3.8.4.1 Error Calculation

The application of the control algorithm starts with the equation 3.71 (the scaled version of 3.62) that calculates the error. The calculation is realized with well known commonly used, “inverting summing amplifier” with multiple inputs and one single-ended output. The circuit adds the reference signal $-x_d$ to the actual signal x to calculate the error $-e$ due to the inversion of the amplifier.

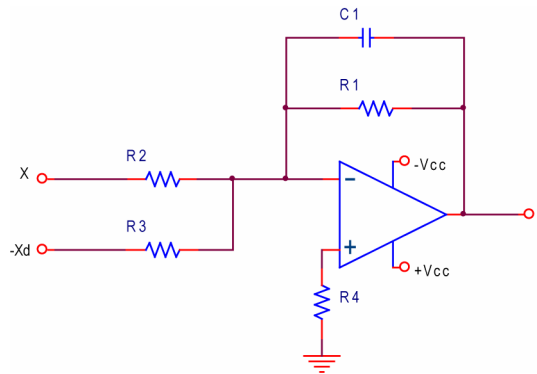


Figure 3.11: Calculation of the error.

Analysis of the circuit shows that the transfer function of the summing amplifier is:

$$V_0 = -\left(\frac{-x_d}{R_2} + \frac{x}{R_3}\right) \cdot \frac{R_1}{R_1 \cdot C_1 \cdot s + 1} = -\frac{[x_d - x]}{\tau \cdot s + 1} \cdot \frac{R_1}{R_2} = -e, \quad R_2 = R_3 \quad 3.76$$

where $V_0 = -e$ is the output voltage, C_1 's are the capacitor, R_1 's the resistance values and $\tau = R_1 \cdot C_1$. If input resistors are equal $R_1 = R_2$, the output is a scaled sum of all inputs, whereas, if they were different, the output would be weighted linear sum of them.

The capacitor C_1 is used to create a first order filtering behavior with corner frequency $f = (2\pi \cdot R_1 \cdot C_1)^{-1}$, so that the possible input noise is limited. For experimental purpose $f \approx 1kHz$ is considered to be high-enough corner frequency. In this circuit R_4 is used to balance the current through the op-amp's input branches and calculated as the equivalent resistance for $R_1 // R_2 // R_3$.

3.8.4.2 Calculation of Error's Derivatives

Calculation of the \dot{e} , error's first derivative, can be realized with a differentiator block that in the mean time sums the reference signal $-x_d$ to the actual signal x . The scheme is presented in Figure 3.12.

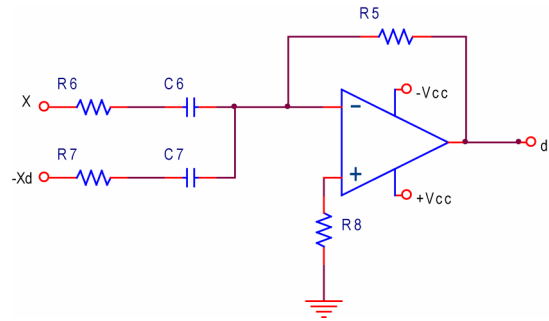


Figure 3.12: The differentiator block used to calculate the error's derivative.

The transfer function for the above circuit is;

$$V_0 = - \left[\frac{R_5 \cdot C_6 \cdot s}{R_6 \cdot C_6 \cdot s + 1} \cdot x + \frac{R_5 \cdot C_7 \cdot s}{R_7 \cdot C_7 \cdot s + 1} \cdot (-x_d) \right] = \frac{R_5 \cdot C_6 \cdot s}{R_6 \cdot C_6 \cdot s + 1} [x_d - x] = -\dot{e} \quad 3.77$$

where $V_0 = -\dot{e}$ is the output voltage. To simplify the calculations, $R_6 = R_7$, $C_6 = C_7$ equalities are preferred. Resistors R_6 and R_7 are installed on purpose since the derivative circuit brings two challenges.

First because the circuit is a high-pass filter by nature, it may amplify unwanted noise and disturbances causing unpredictable signals. To reduce this undesirable effect, resistors $R_6 = R_7$ place a limit on the high frequency gain to $G_{\max} = R_5/R_6 = R_5/R_7$. To further cut the high frequency gain, many circuits include a feedback capacitor C_F , with a value around $C_F = C_5/10$, across R_5 . With C_F , the circuit begins to look like a low-pass filter at higher frequencies.

The second challenge of the derivative circuit is keeping it stable. The classic op-amp differentiator may oscillate if resistors R_6 and R_7 were missing. Those resistors reduce the phase-shift caused by R_5 and C_6 , or by R_5 and C_7 , especially at high frequencies where it can threaten circuit stability. Capacitor C_F brings an added bonus of bringing stability to the differentiator. And finally, C_F helps the differentiator recover in case its output is overdriven to the supply rails.

Accordingly the response in time domain can be written as;

$$V_0 = -R_5 \cdot C_6 \cdot \frac{d(x_d - x)}{dt} = -R_5 \cdot C_6 \cdot \frac{de}{dt} \quad 3.78$$

And the frequency response is;

$$K(j\omega) = -j\omega \cdot R_5 \cdot C_6 \quad 3.79$$

$$|K(j\omega)| = \omega \cdot R_5 \cdot C_6 \quad 3.80$$

$$\varphi(\omega) = +\frac{\pi}{2} \quad 3.81$$

The Bode plot for an ideal differentiator (missing R_6 and R_7) has a constant slope of +20dB/decade, which is unrealistic since for a real circuit the gain cannot exceed the open-loop gain as shown in Figure 3.13. Apart from this, the gain increasing with frequency makes the circuit more sensitive to high-frequency noise and may result in instability. Existence of those problems approves the necessity to use resistors $R_6 \neq 0$ and $R_7 \neq 0$, which reduces the gain at high frequencies.

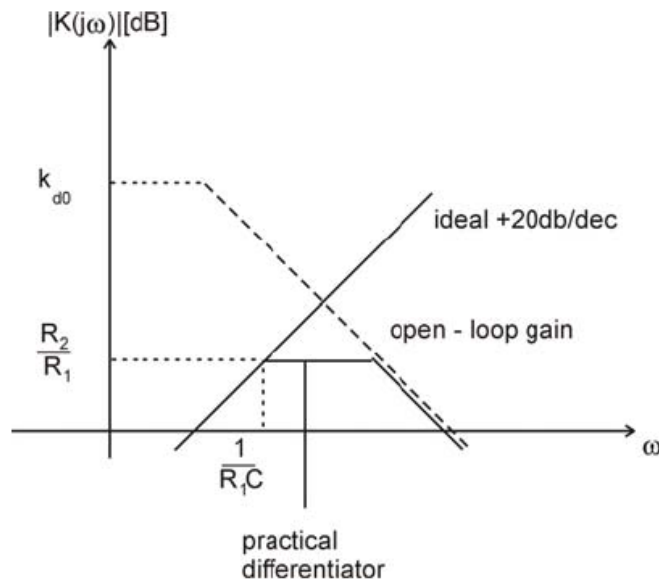


Figure 3.13: Bode plot for an ideal differentiator as in comparison to the open-loop gain.

Now the differentiation only occurs at the frequencies $\omega \leq \omega_c$ where

$$\omega_c = \frac{1}{R_6 \cdot C_6}, \quad f_c = 2\pi \cdot \omega_c \quad 3.82$$

Another important point in the error's derivative calculation is having coefficient 1 through $R_5 \cdot C_6$ multiplication since this requires large capacitance C_6 . Instead, one can calculate $\dot{e}/100$, not \dot{e} in this step, to reduce component values and then compensate for the difference in next steps by using $\dot{e} \times 100$ instead of \dot{e} .

3.8.4.3 Calculation of the Sliding Surface “ σ ”

Equation 3.64 summarizes the work required by the op-amp U3. Obviously an inverting summing amplifier, as discussed in section 3.8.4.1, can be used. This time filtering components are omitted (Figure 3.14).

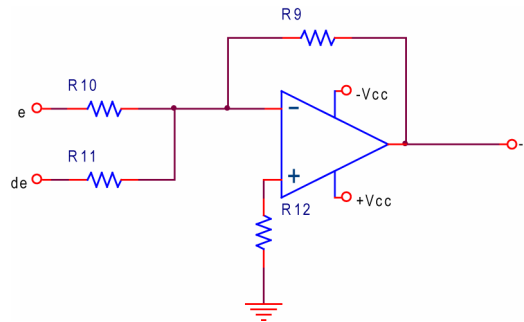


Figure 3.14: Calculation of the sliding surface.

Analysis of the above circuit shows that the transfer function of this summing amplifier is:

$$V_0 = - \left(\underbrace{\frac{R_9}{R_{10}}}_C \cdot e + \dot{e} \cdot \underbrace{\frac{R_9}{R_{11}}}_1 \right) = -\sigma \quad 3.83$$

Input resistors R_{10} and R_{11} are selected in different values, so the output is weighted linear sum of the inputs.

3.8.4.4 Calculation of the Intermediate Signal “ φ ”

The intermediate signal φ is a weighted sum of the sliding surface σ with the control output u that is fed back to the system. The summation must also be filtered through a first order filter. Therefore equation 3.65 is applied exactly in the same manner with section 3.8.4.1 (Figure 3.15).

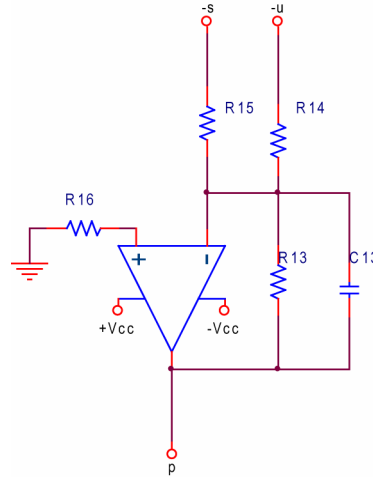


Figure 3.15: Calculation of the Intermediate Signal “ φ ”

Analysis of the circuit shows that the transfer function of this circuit is:

$$V_0 = - \left((-\sigma) \cdot \underbrace{\frac{R_{13}}{R_{15}}}_{K \cdot g} + (-u) \cdot \underbrace{\frac{R_{13}}{R_{14}}}_1 \right) \cdot \frac{1}{\underbrace{R_{13} \cdot C_{13} \cdot s + 1}_g} = \varphi \quad 3.84$$

The capacitor C_{13} is used to create a first order filtering behavior with corner frequency $\tau = 1/g = R_{13} \cdot C_{13}$, so that the required low pass filter in the equation is applied. The balance resistor R_{16} is selected as the equivalent resistance for $R_{13} // R_{14} // R_{15}$.

3.8.4.5 Calculation of the Intermediate Signal “ $\alpha \cdot \dot{x}$ ”

The intermediate signal $\alpha \cdot \dot{x}$, or more precisely $-\alpha \cdot \dot{x}$, is a signal required for the calculation of the control correction term \hat{u} from the DO. The α coefficient in the signal represents a constant coefficient with value $\alpha = m_N \cdot g / T_N$. Since the derivative of

the position measurement \dot{x} is required one must calculate $\frac{g_v}{s + g_v} \cdot s x$ and multiply it

with the α coefficient to complete this step. Necessity for the first order filter $\frac{g_v}{s + g_v}$ is

justified both in section 3.4.2.6 and in 3.8.4.2. Accordingly the circuit in Figure 3.16 is designed.

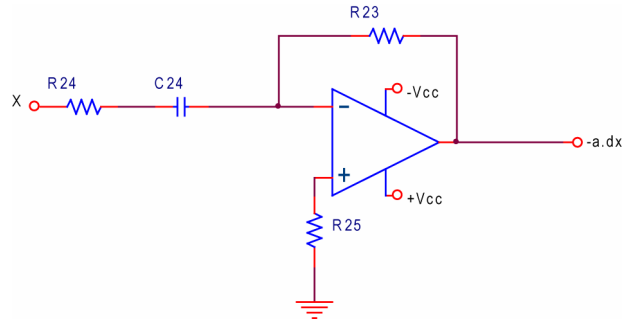


Figure 3.16: Calculation of the Intermediate Signal “ $\alpha \cdot \dot{x}$ ”

The transfer function for the above circuit is;

$$V_0 = -\underbrace{R_{23} \cdot C_{24}}_{\alpha} \cdot \frac{1}{\underbrace{R_{24} \cdot C_{24} \cdot s + 1}_{\frac{g_v}{s + g_v}}} \cdot s \cdot x = -\alpha \cdot \dot{x} \quad 3.85$$

where g_v corresponds to $g_v = (R_{24} \cdot C_{24})^{-1}$ and $R_{23} \cdot C_{24} = \alpha$ is the necessary coefficient.

3.8.4.6 Calculation of the Intermediate Signal “ ψ ”

The intermediate signal ψ has the same structure with the intermediate signal φ (Figure 3.17).

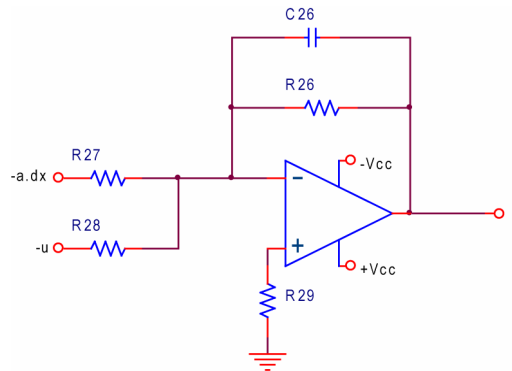


Figure 3.17: Calculation of the Intermediate Signal “ ψ ”

Analysis of the circuit shows that the transfer function of this circuit is:

$$V_0 = -\left(\frac{R_{26}}{\underbrace{R_{27}}_1} \cdot (-\alpha \cdot \dot{x}) + \frac{R_{26}}{\underbrace{R_{28}}_1} \cdot (-u) \right) \cdot \frac{1}{\underbrace{R_{26} \cdot C_{26} \cdot s + 1}_{\frac{g}{s + g}}} = \psi \quad 3.86$$

3.8.4.7 Calculation of the Control Output “ u ”

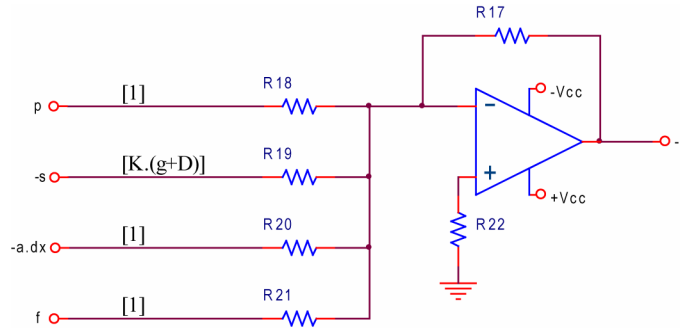


Figure 3.18: Calculation of the Control Output “ $-u$ ”

The final step in the controller implementation is the summation to find the control output $-u$, to be fed to the high voltage amplifier (HVA) described in next section. The transfer function for this final circuit is;

$$V_0 = - \left(\underbrace{\frac{R_{17}}{R_{18}}}_1 \cdot \varphi + \frac{R_{17}}{\underbrace{R_{19}}_{K(g+D)}} \cdot (-\sigma) + \frac{R_{17}}{\underbrace{R_{20}}_1} \cdot (-\alpha \cdot \dot{x}) + \frac{R_{17}}{\underbrace{R_{21}}_1} \cdot \psi \right) = -u \quad 3.87$$

3.8.5 High Voltage Amplifier

Piezoelectric actuators require $-60 \dots 150V$ for full range operation while the described circuit can handle only few volts. For this reason a high voltage amplifier is added to the circuit as a buffer between the calculation circuit and the actuator. This circuit is actually a simple inverting amplifier with constant gain with MP108 power op-amp is used as the core, as presented in Figure 3.19.

The input is protected with diodes D1 and D2, while the rest of the circuit is designed as suggested by the datasheet. The circuit is supplied by a dual supply with $\pm 150V$, 1A per channel power supply. The gain is selected as -10 to amplify the control u to the necessary $-150 \dots 150V$ range. No precaution is taken to prevent the output voltage to be less than $-60V$, which is defined as the breakdown level of the piezoelectric actuator. Therefore care must be taken with the input signals. This could also be achieved by limiting the negative input supply $-V_{cc}$ with $-60V$.

The compensation capacitor C_c is selected to be $10pF$ allowing a slew rate of $170V$ per microsecond. The current limit resistor R_{lim} is calculated as 0.65Ω according

to the formula given in the producer's datasheet; $R_{lim} = 0.65/I_{lim}$ where I_{lim} is the max permissible current selected as 1A.

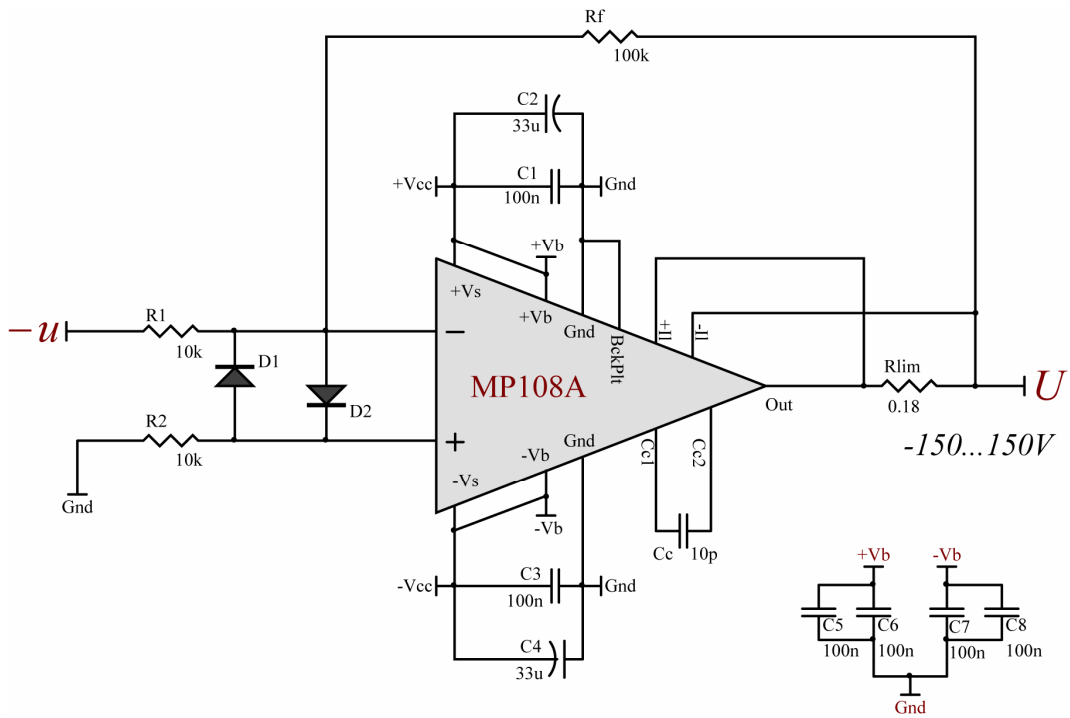


Figure 3.19: High voltage amplifier as a final block of the circuit.

Transfer function of this block can be written as;

$$V_0 = -V_i \cdot \frac{R_f}{R_1} = -\frac{R_f}{R_1} (-u) = U \quad 3.88$$

where $V_0 = U$ is the output voltage fed to the piezoelectric actuator, $V_i = -u$ is the control calculated from previous stages, R_i 's the resistance values with $R_1 = R_2 = R_f/10$.

According to the data given for MP108 amplifier, the open-loop gain of the amplifier at 15kHz is typically 96dB $\approx 63095,7$. Therefore for the used gain of 10, the influence of the closed loop behavior of the amplifier can be neglected.

3.8.5.1 Power Limitation

Due to the limitations on the power that the amplifier can supply, the maximum operation frequency of the piezoelectric actuator is limited. Note that the resonance frequency of the used actuator is 15kHz, well above the frequency set by the voltage amplifier. This second limit can easily be calculated;

$$Q = C \cdot V$$

$$I_{AVRG} = \frac{dQ}{dt} = C \cdot \frac{dV}{dt} \quad 3.89$$

where I_{AVRG} is the average current required for the motion [28, 42]. On the other hand, the peak current I_{PEAK} , required for the fast motion is defined as [28, 42];

$$I_{PEAK} = \pi \cdot I_{AVRG} \quad 3.90$$

Knowing that the maximum current supplied by the voltage amplifier is $1A$, and the capacitance of the actuator is $C = 2400nF$, we can calculate the maximum operation frequency as $f_{MAX} \approx 5.2kHz$, which is well above the targeted operation frequency.

3.8.5.2 The Effect of HVA

The disturbance observer as proposed in section 3.5 proposes that the control output is directly fed to the plant. However, the high voltage amplifier (HVA) constitutes an additional transfer function W between the control $-u$ from the controller and control fed to the actuator U .

$$U = W \cdot u = W \cdot (u_0 + \hat{u}) \quad 3.91$$

The same disturbance observer proposed by Ohnishi et al., described and analyzed in section 3.5, can still be used [55], however the effect of the HVA must be studied. The derivation of the observer is as follows; from 3.45 the disturbance is;

$$F_d = T_N \cdot U - m_N \cdot s^2 x \quad 3.92$$

As realized in previous sections the estimated disturbance can be defined as;

$$\hat{F}_d = G(s) \cdot (T_N \cdot U - m_N \cdot s^2 x) \quad 3.93$$

where \hat{F}_d is the observed disturbance force, G is the a filter of suitable order. Since x , u and U are measurable, \hat{u} , the correction to be added to the control output of the controller to compensate for the disturbance, can then be calculated as

$$\hat{u} = \frac{\hat{F}_d}{T_N} = G(s) \cdot \left(u - \frac{m_N}{T_N} \cdot s^2 x \right) \quad 3.94$$

In fact, instead of the control u the amplified control U must be used in the above formula since U is the real control input to the plant. However, since U is a high

voltage signal, it is preferable to keep-it outside of the calculation part that consist of low voltage signals only. Besides, the HVA may depend on plant properties and have different dynamics for different plants. Isolating the control U from the DO would simplify the application of the controller to different plants.

The effect of this choice is analyzed below. We know that the control U can be calculated by the following steps;

$$\begin{aligned}
 U &= (W \cdot u_0 + W \cdot \hat{u}) = W \cdot u_0 + \underbrace{G \cdot W \cdot u - W \cdot G}_{G \cdot U} \cdot \frac{m_N}{T_N} \cdot s^2 x \\
 \Rightarrow U &= \frac{W \cdot u_0}{(1-G)} - \frac{W \cdot G}{(1-G)} \cdot \frac{m_N}{T_N} \cdot s^2 x
 \end{aligned} \tag{3.95}$$

Inserting this last equation into the plant equation $m_N \cdot s^2 x = T_N \cdot U - F_d$ one obtains,

$$m_N \cdot s^2 x = \frac{T_N \cdot W}{(1+W \cdot G - G)} \cdot u_0 - \frac{(1-G)}{(1+W \cdot G - G)} \cdot F_d \tag{3.96}$$

which is the best rejection of the total disturbance, that may be achieved by this scheme. If the transfer function W was unity, $W = 1$, then this last equation would yield;

$$m_N \cdot s^2 x = T_N \cdot u_0 - (1-G) \cdot F_d \tag{3.97}$$

which is the same equation found earlier 3.54.

Independently from the transfer function W , the discussed observer best performs when G tends to 1; the positive feedback of \hat{u} would, ideally, force the system to behave close to an ideal system defined by

$$m_N \cdot s^2 x = T_N \cdot u_0(t) \tag{3.98}$$

where $u_0(t)$ is the control output from the Sliding Mode Controller. However, in reality the dynamics of the observer would lead to differences between the real disturbance and the estimated disturbance.

Equations 3.91 and 3.92 can also be used to determine the control correction term \hat{u} in few steps;

$$\begin{aligned}
T_N \cdot u &= \frac{\hat{u}}{G} + m_N \cdot s^2 x \\
m_N \cdot s^2 x &= W \cdot [T_N \cdot u] - F_d \\
m_N \cdot s^2 x \cdot (1 - W) &= \left(W \cdot \frac{\hat{u}}{G} \right) - F_d \\
\hat{u} &= \frac{m_N \cdot s^2 x \cdot (1 - W) + F_d}{W} \cdot G
\end{aligned} \tag{3.99}$$

Note that \hat{u} tends to the disturbance force F_d , if both G and W tend to 1. With those new additions, the observer implementation is different than the one previously shown and presented on Figure 3.20.

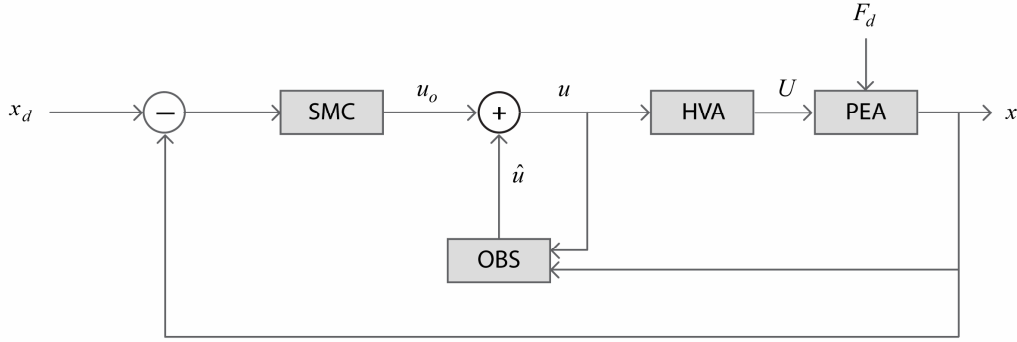


Figure 3.20: Observer implementation with the addition of the HVA.

3.9 Analysis

This part of the text concentrates on the analysis of the plant, controller, DO and analog circuit. The analysis starts with the transfer function formation of the plant. Because transfer functions are complex-valued, frequency-dependent quantities, we can better appreciate a transfer function by examining the magnitude and phase for various input frequencies.

The nonlinear behavior of the piezoelectric actuator, mainly dominated by the hysteresis, prevents us using linear system analysis tools for the investigation of the system. However, for this section we will assume that, for Sliding Mode Controller without observer, the plant is second order linear plant without hysteresis. On the other hand for the Sliding Mode Controller with disturbance case, we are assuming that the observer linearizes the plant and therefore linear analysis tool can be used.

Figure 3.21 below, demonstrates the block diagram of the full scheme composed of the Sliding Mode Controller (SMC), high voltage amplifier (HVA), plant, namely the piezoelectric actuator, and the disturbance observer (DO). The transfer function the Sliding Mode Controller is represented by $C(s)$, high voltage amplifier by $W(s)$, plant by $P(s)$. The transfer function of the observer is a combination of the functions $H_1(s)$ and $H_2(s)$. The signals x_d , x , e , u_0 , \hat{u} , u , U , F_d/T_N represents the desired position, actual position, position tracking error, control output from SMC, observers correction term to the control, total control term, amplified control and disturbance force over nominal value of the piezoelectric effect conversion constant respectively

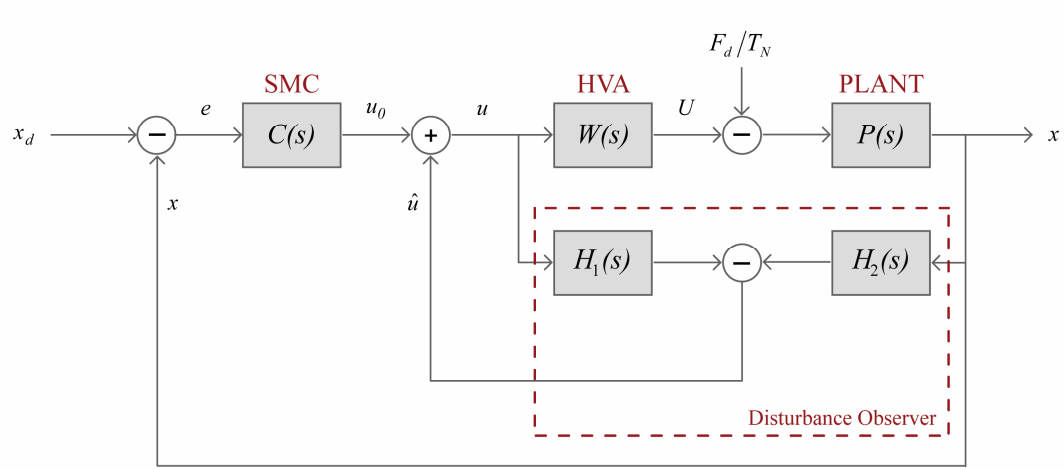


Figure 3.21: The block diagram of the full control scheme.

From the above diagram the following equations can immediately be written;

$$e = x_d - x \quad 3.100$$

$$u_0 = C(s) \cdot e \quad 3.101$$

$$u = u_0 + \hat{u} \quad 3.102$$

$$U = W(s) \cdot u \quad 3.103$$

$$x = P(s) \cdot \left(U + \frac{F_d}{T_N} \right) \quad 3.104$$

$$\hat{u} = H_1(s) \cdot u - H_2(s) \cdot x \quad 3.105$$

The next step in the analysis is the calculation of the required transfer functions for further analysis; $C(s)$, $P(s)$, $W(s)$, $H_1(s)$ and $H_2(s)$. For this step the information

on the previous sections is used. The transfer function of the plant can be found from equations 3.6 and 3.7 for the nominal parameter definition given in equation 3.41;

$$P(s) = \frac{X(s)}{U(s)} = \frac{T_N}{m_N \cdot s^2 + c_N \cdot s + k_N} \quad 3.106$$

since, for Sliding Mode Controller without observer, the plant is assumed to be second order linear plant without hysteresis or other disturbance.

The high voltage amplifier transfer function W is already given in 3.88;

$$W(s) = -\frac{R_f}{R_1} = -10 \quad 3.107$$

The used first order filter $G(s)$ is;

$$G(s) = \frac{g}{s + g} = \frac{1}{R_{13} \cdot C_{13} \cdot s + 1} = \frac{1}{R_{26} \cdot C_{26} \cdot s + 1} \quad 3.108$$

From 3.105 one can easily conclude that;

$$H_1(s) = \frac{g}{s + g} = G(s) \quad 3.109$$

$$H_2(s) = \frac{m_N \cdot g}{T_N} \cdot (1 - G(s)) \cdot s \quad 3.110$$

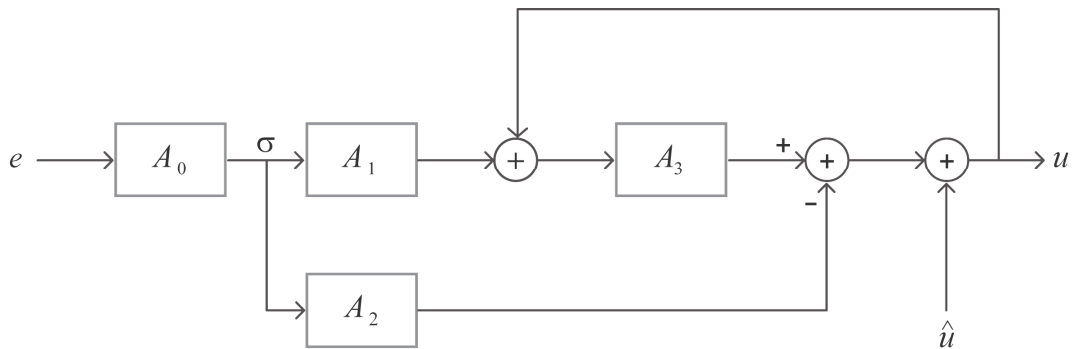


Figure 3.22: Analog Sliding Mode Controller block diagram. \hat{u} is used to mark the input point of the disturbance observer.

To calculate $C(s)$, the transfer function of the Analog Sliding Mode Controller, one must look at the controller scheme presented in Figure 3.22. Accordingly, for the ideal op-amp case, where the open-loop gain is assumed to be high enough, the transfer functions $A_0(s) \cdots A_3(s)$, can be written as;

$$A_0(s) = C + s \quad 3.111$$

$$A_1(s) = K \cdot g \quad 3.112$$

$$A_2(s) = K \cdot (g + D) \quad 3.113$$

$$A_3(s) = \frac{g}{s + g} = G(s) \quad 3.114$$

Using the block diagram and those equations the calculation of the transfer function $C(s) = u/e$ is straight forward;

$$\sigma = A_0 \cdot e \quad 3.115$$

$$u = A_3 \cdot (A_1 \cdot \sigma + u) - A_2 \cdot \sigma = A_3 \cdot A_1 \cdot A_0 \cdot e + A_3 \cdot u - A_2 \cdot A_0 \cdot e \quad 3.116$$

$$C(s) = \frac{U(s)}{E(s)} = \frac{A_3 \cdot A_1 \cdot A_0 - A_2 \cdot A_0}{1 - A_3} \quad 3.117$$

3.9.1 Plant Analysis

3.9.1.1 Transient Response Analysis

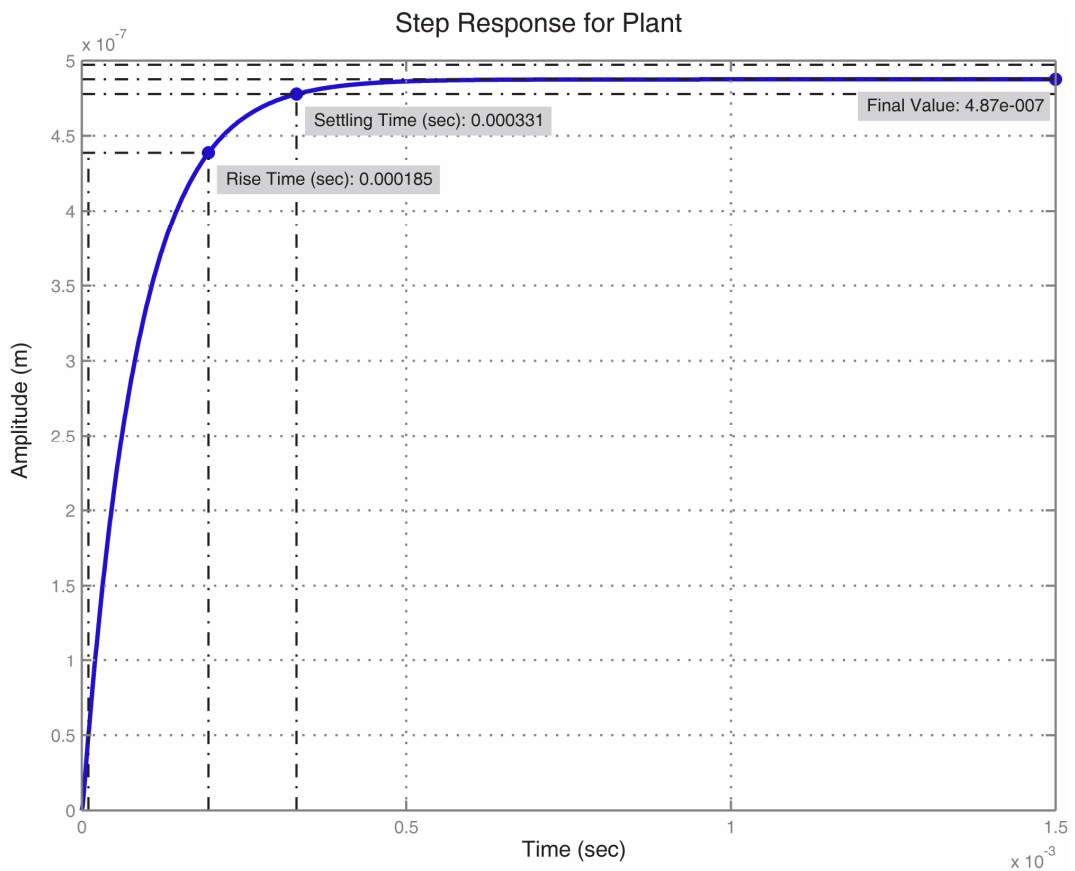


Figure 3.23: Transient response of the open-loop PEA plant to a unit-step input.

In many practical cases, the desired performance characteristics of control systems are specified in terms of time-domain quantities. Systems with energy storage cannot respond instantaneously and will exhibit transient responses whenever they are subjected to inputs or disturbances. To specify the performance of the open-loop PEA plant, transient response to a unit-step input is presented in Figure 3.23. The response is calculated for the standard initial conditions; the system is initially at rest with all outputs, inputs and related derivatives zero.

The above plot demonstrates the rise time ($185\mu s$) and the settling time ($331\mu s$). Moreover, clearly the final settled value is $487nm$ and the response does not have any visible overshoot. Those numbers are important to show the performance of the controller since on later sections similar responses to unit-step inputs will be instigated for closed loop systems.

3.9.1.2 Frequency Response Analysis

The frequency response analysis refers to the steady state analysis of a system to a sinusoidal input. In frequency-response methods, the input signal frequency is varied over a certain range and the resulting response is studied as a bode plot that represents the response in terms of magnitude and phase plots. The frequency response analysis of the open-loop plant (PEA) is presented in Figure 3.24.

Since the plant transfer function is a standard second order plant, we can use related information to study the transfer function;

$$P(s) = \frac{T_N / m_N}{s^2 + \frac{c_N}{m_N} \cdot s + \frac{k_N}{m_N}} = \frac{K \cdot \omega_n^2}{s^2 + 2 \cdot \omega_n \cdot \zeta \cdot s + \omega_n^2} \quad 3.118$$

Accordingly the gain K , the natural frequency ω_n and damping factor ζ can be calculated as;

$$K = \frac{T_N}{k_N}, \quad \omega_n = \sqrt{\frac{k_N}{m_N}}, \quad \zeta = \sqrt{\frac{c_N^2}{4 \cdot k_N \cdot m_N}} \quad 3.119$$

For the plant parameters used in this work, the natural frequency ω_n can be calculated as $\omega_n = 9.3 \cdot 10^4 \text{ rad/s} = 1.48 \cdot 10^4 \text{ Hz}$. Another important aspect of the

analysis is that the model is linear below the frequency $\sim 1kHz$, then a roll-off of $40dB/dec$ occurs.

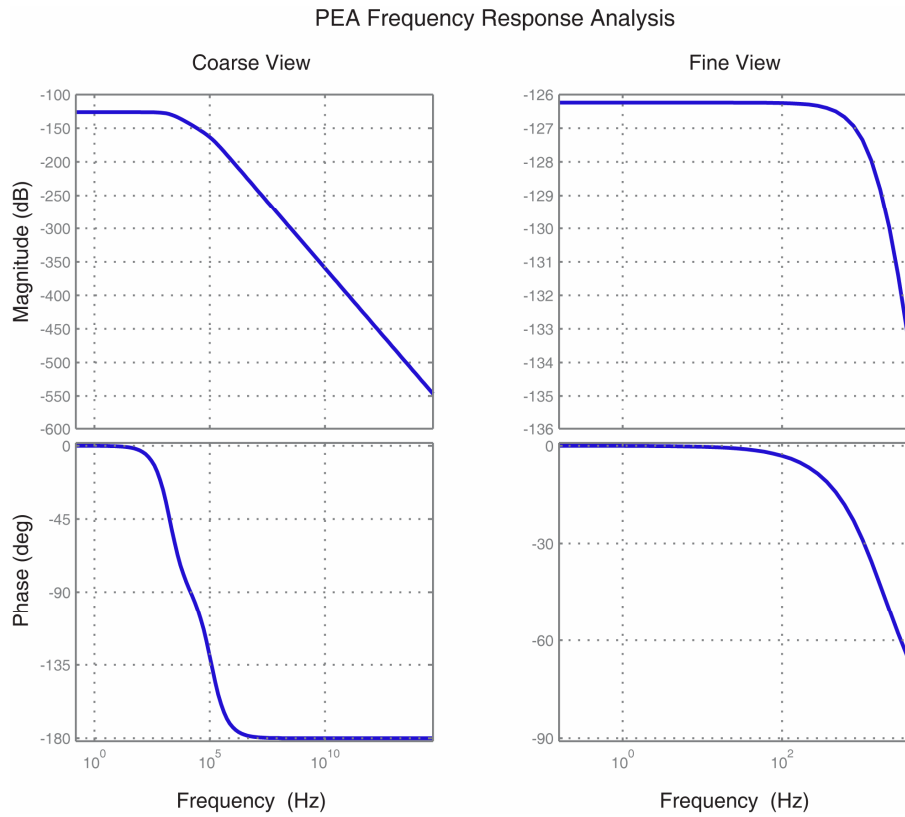


Figure 3.24: The frequency response analysis of the open-loop plant (PEA): wide frequency range on the left and closer view on the right.

3.9.2 Controller Analysis

The analysis of the Sliding Mode Controller requires the calculation of x/x_d which can be obtained from the above equations as follows; inserting 3.105 into 3.102;

$$u = \frac{u_0 - H_2 \cdot x}{1 - H_1} \quad 3.120$$

then using 3.103 and 3.104 one can obtain;

$$u = (P^{-1} \cdot x - dist) \cdot W^{-1} \quad 3.121$$

where $dist = F_d/T_N$. Now using equations 3.100, 3.101 and 3.120 and collecting terms together the transfer function can be obtained.

$$x = \frac{P \cdot W \cdot C}{1 - H_1 + P \cdot W \cdot (H_2 + C)} \cdot x_d + \frac{P \cdot (1 - H_1)}{1 - H_1 + P \cdot W \cdot (H_2 + C)} \cdot dist \quad 3.122$$

If the transfer functions $H_1(s)$ and $H_2(s)$ are assumed to be zero; $H_1 = H_2 = 0$, then the above equation reduces to the case where only the Analog Sliding Mode Controller is in action and the disturbance observer is removed. For this later case the transfer function reduces to;

$$x = \frac{P \cdot W \cdot C}{1 + P \cdot W \cdot C} \cdot x_d + \frac{P}{1 + P \cdot W \cdot C} \cdot dist \quad 3.123$$

3.9.2.1 Frequency Analysis: Open Loop vs Closed Loop

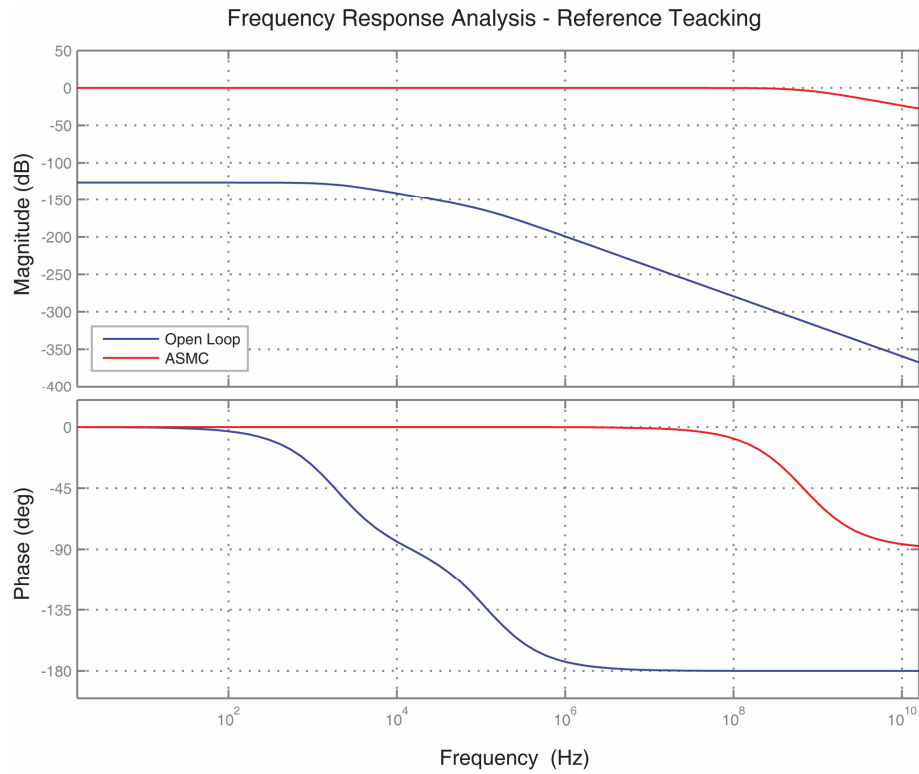


Figure 3.25: Open-loop vs closed loop frequency response plots for PEA. The closed loop does not contain disturbance observer information.

The later transfer function, calculated in the previous section, supplies enough information to study the frequency response of designed analog SMC as a bode plot. Figure 3.25 shows the bode plots for the system transfer function x/x_d for open-loop plant and Analog Sliding Mode Controller without the disturbance observer (assuming zero disturbance; $dist \approx 0$).

For the controlled plant, one can see that, the linear tracking is greatly enhanced and exact tracking can be obtained up to the frequencies like 10MHz. For the closed loop system, gain and phase margins are also calculated (Figure 3.26); the gain margin

for the Sliding Mode Controlled system is infinite while the phase margin is calculated as 0 rad/s.

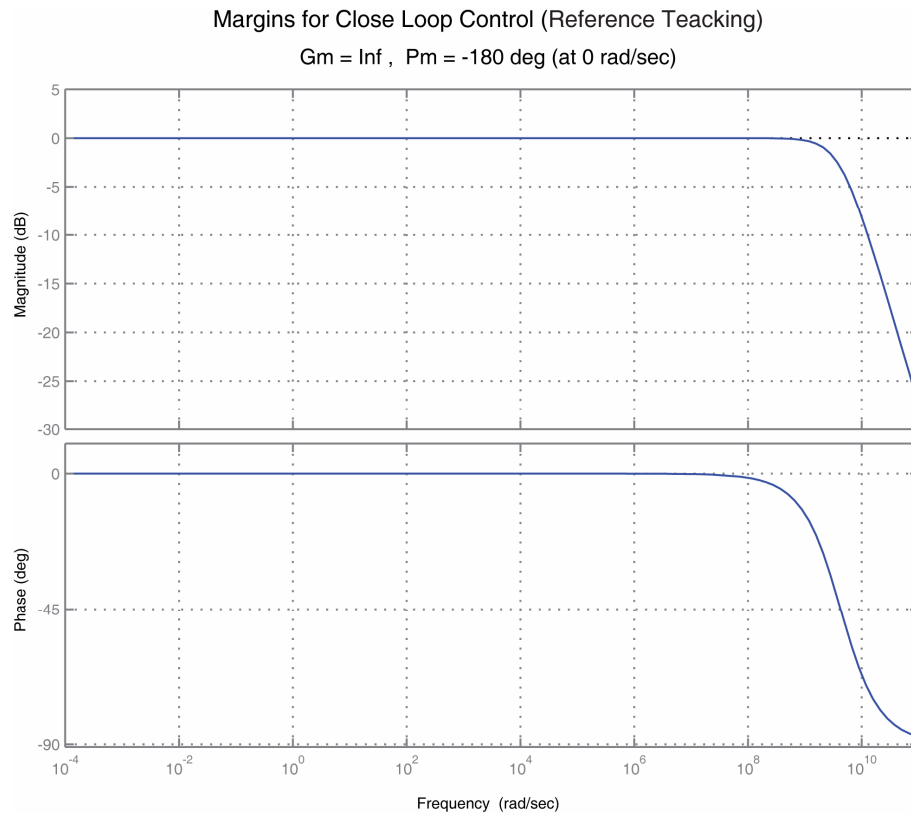


Figure 3.26: Gain and phase margins for closed loop system calculated by MatLab.

3.9.2.2 Disturbance Observer Analysis

Second parts of the equations 3.122 and 3.123 represents the reaction of the closed loop system to the disturbance, which contains parameter variations, damping c and springiness k terms and external forces, by selection in this work. Using these terms, one can depict the frequency response of the system under analog SMC with and without the DO and observe the performance of the disturbance observer. According to the bode plots, the SMC with without DO performs almost identical for reference tracking (Figure 3.27 on the left). For the disturbance rejection on the other hand, the responses differ as expected; the attenuation is higher in the presence of the DO (Figure 3.27 on the right).

To further examine the DO behavior and performance, responses of disturbance rejection for different cases are plotted in Figure 3.28. In this part of the study the nominal plant parameters are selected as given in Table 3.2. But the actual parameters are selected to be in the $\pm 10\%$ range of them for all plots;

$$m = m_N \times 0.92 \quad 3.124$$

$$b = b_N \times 1.05 \quad 3.125$$

$$T = T_N \times 0.90 \quad 3.126$$

$$k = k_N \times 1.01 \quad 3.127$$

Yet different filtering coefficients g are used in the plots to demonstrate the effect on the observer. Values are summarized on Table 3.6. In this figure (Figure 3.28) the plots marked with plus signs and dots demonstrates the disturbance rejection performance increase added by the DO. On the other hand, the comparison of the three plots marked with dots, circles and crosses clarifies the effect of the corner frequency increase for the filter G given in equation 3.94. As seen from the figure, increasing g coefficient increases the attenuation of the higher frequency disturbance as expected.

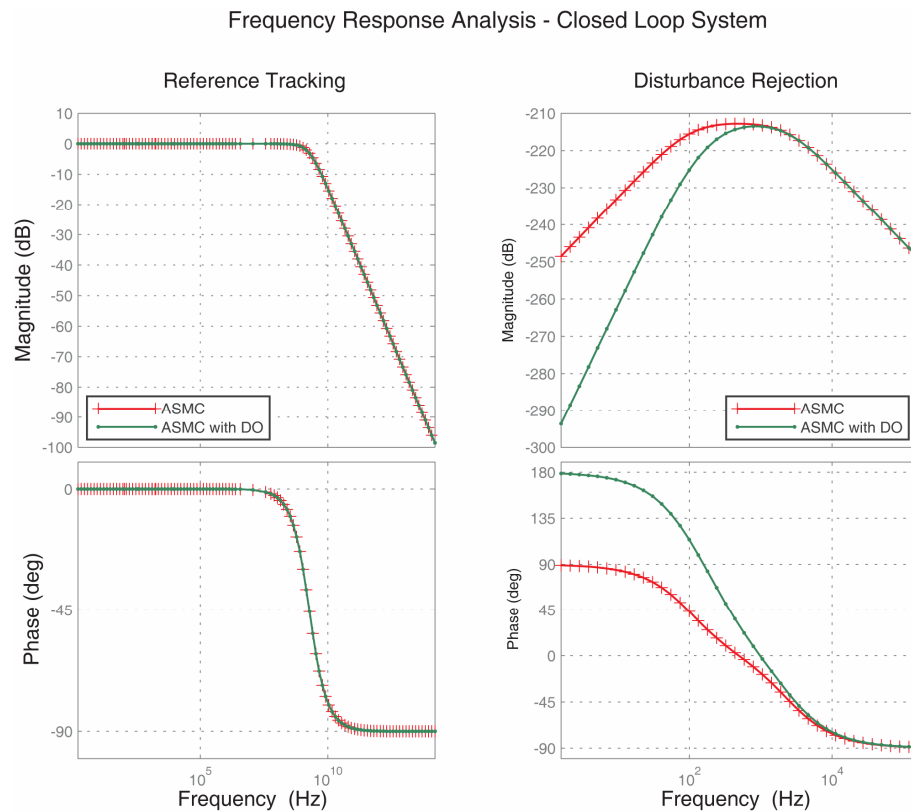


Figure 3.27: Frequency response analysis for plant under control with and without the disturbance observer: the reference tracking analysis on the left and disturbance rejection analysis on the right.

Table 3.6: Parameters used in the disturbance rejection performance study.

	Plot Marker	Disturbance Observer	g
Plot 1	+	no	1785.7
Plot 2	.	yes	1785.7
Plot 3	o	yes	$1785.7 \cdot 10$
Plot 4	x	yes	$1785.7 \cdot 10^2$

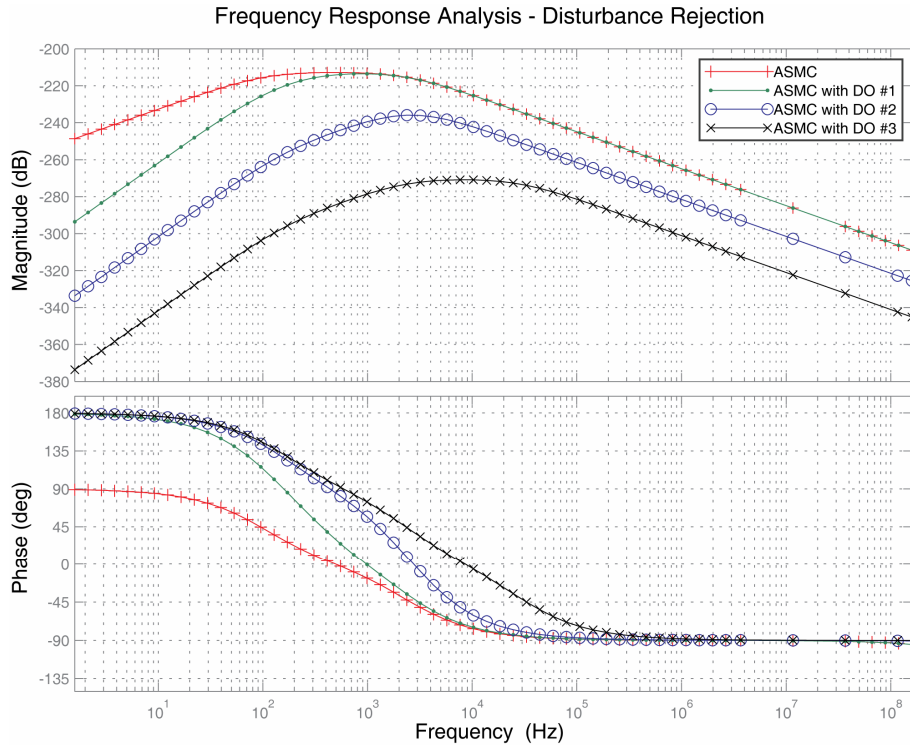


Figure 3.28: Disturbance rejection performance comparison for different parameters by means of Bode plot.

3.9.3 Circuit Simulations

In the above sections the analysis of the designed controller and disturbance observer are investigated. However, before final analog application, the circuit design should also be examined at least by simulations. For this purpose Orcad Capture software from Cadence Design Systems is used (version 9.2).

The plant is represented with a simple second order low pass filter designed in Sallen-Key topology (Figure 3.29). The circuit transfer function fits the plant transfer function with nominal parameters and since the filter is an inverting one, an inverting voltage follower is used for signal consistency. Much complicated equivalent circuits or

PEA circuit models from researchers could also be used. However, the purpose of this step is to understand the circuit behavior and not to simulate the plant. Therefore the used filter equivalent is considered to be enough for this work.

The result of the circuit simulations is presented in Figure 3.30. The plot at the top is the control “ $-u$ ” calculated by the designed circuit. The plot at the center demonstrates the reference and actual trajectories x_d and x together with the tracking error e which’s amplitude is neglectable compare to the other signals.

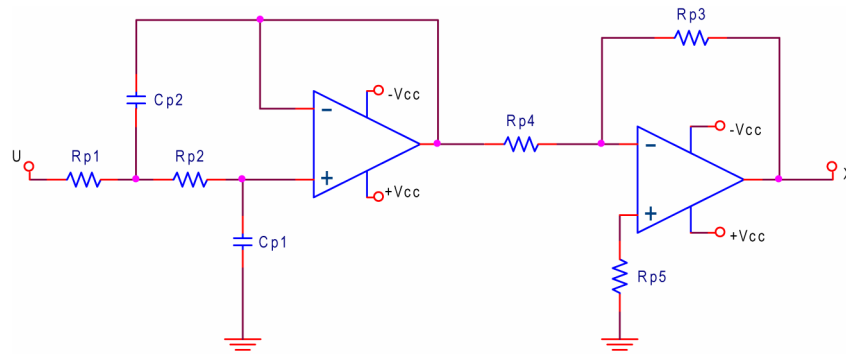


Figure 3.29: Plant representation for circuit simulation purposes.

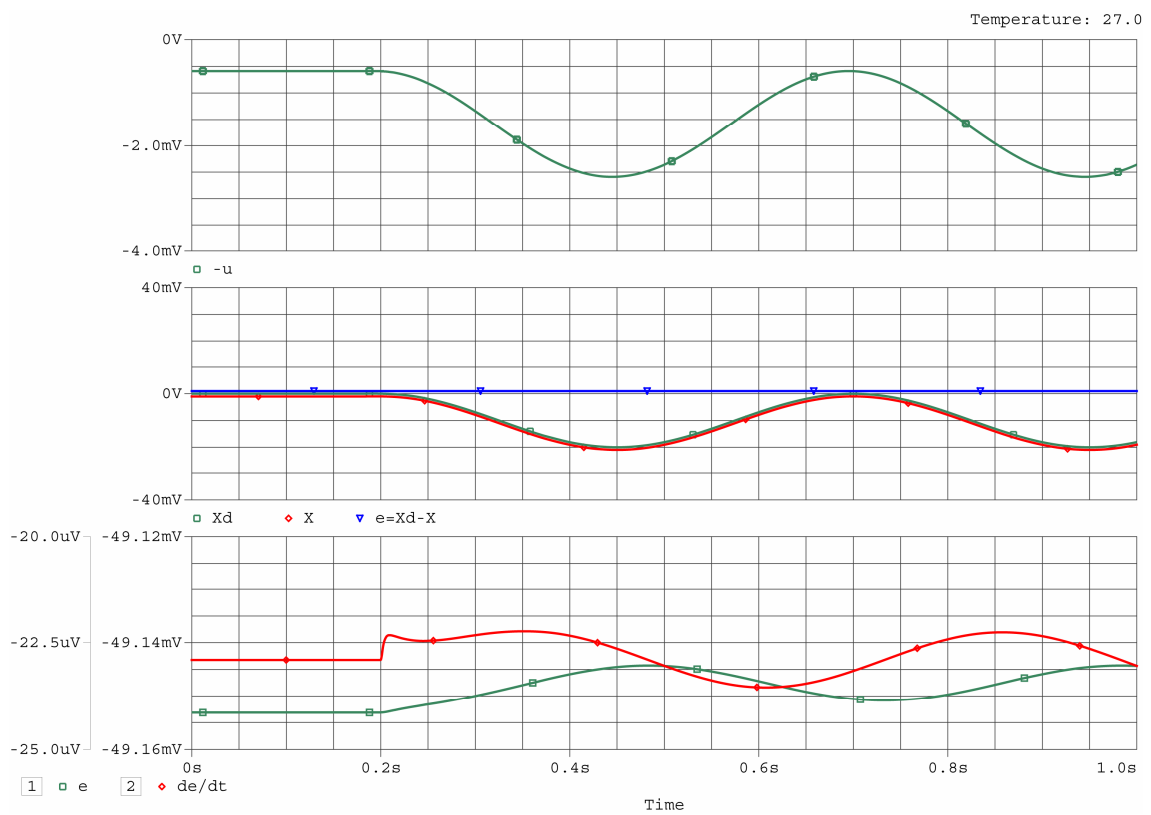


Figure 3.30: Circuit analysis results.

The two signals presented at the bottom part of the Figure 3.30 are the error signal and its derivative. One can see from the figure that, the tracking of the reference $x_d = 10 + 10 \cdot \sin(4\pi \cdot t)$ results with about 2 microvolts error corresponding to 0.01%.

The simulations are repeated for different input shapes and amplitudes but not all results are presented here. The result in Figure 3.30 is especially selected since it demonstrates the performance for small reference signals that can lead to very small signals in the calculations and therefore result with failure. Another trouble with the small signals is the signal to noise ratio that becomes large to deteriorate the performance.



4 EXPERIMENTAL RESULTS

4.1 Experimental Setup

For experimental purposes, the setup shown in Figure 4.1 has been constructed. The voltage amplifier is the circuit built by using MP108 power operational amplifier from Apex Microtechnology, PEA is the piezoelectric actuator with embedded strain gage for position measurement, PSt 150/5/60 VS10 from Piezomechanik SVR, and the strain gage amplifier is the SCM5B38-03 wide band strain gage amplifier from Dataforth Corporation.

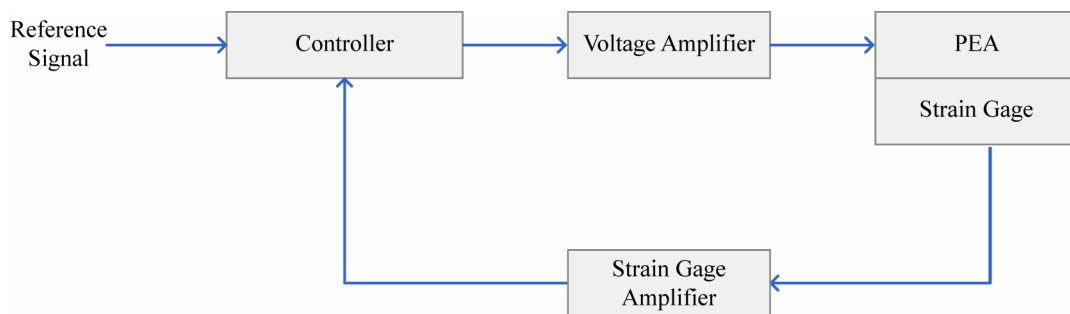


Figure 4.1: Piezoelectric actuator control setup.

For different experiments, the block marked as “Controller” is replaced by the suitable algorithm on the suitable platform; it is replaced by the DSP controller in DSP experiments or by the Analog Circuit in Analog Controller experiments.

The data is captured by Agilent Technologies 54622D digital oscilloscope. The reference and actual signals are generally presented without offset to have a better feeling on the tracking error. The third channel shown in some figures is the error signal. Peak to peak values are given at the image captions in metric correspondents: 17.96 μm (micrometers) corresponds to 1V of the strain gage amplifier reading, or in other words 1 μm position deflection results 55.68mV and 1nm creates only 55.68 μV .

Figure 4.2 shows the actual version of the controller test bed unit that has been assembled as part of this research. Computer connections are not shown in the figure. The setup shown consists of;

- PEA: the piezoelectric actuator mounted inside a plastic box, together with the strain gage amplifier circuit, to mechanically isolate from outside effects,
- HV PSU: high voltage power supply unit ($\pm 150\text{V}$),
- LV PSU: low voltage power supply ($\pm 15\text{V}$),
- HVA: the MP108 circuit mounted on a piece of aluminum cooler with fan,
- SMC & DO: the Sliding Mode Controller and Disturbance Observer circuits connected to each other and to the plant as it is required,
- Signal generator for reference input and oscilloscope for data connection.

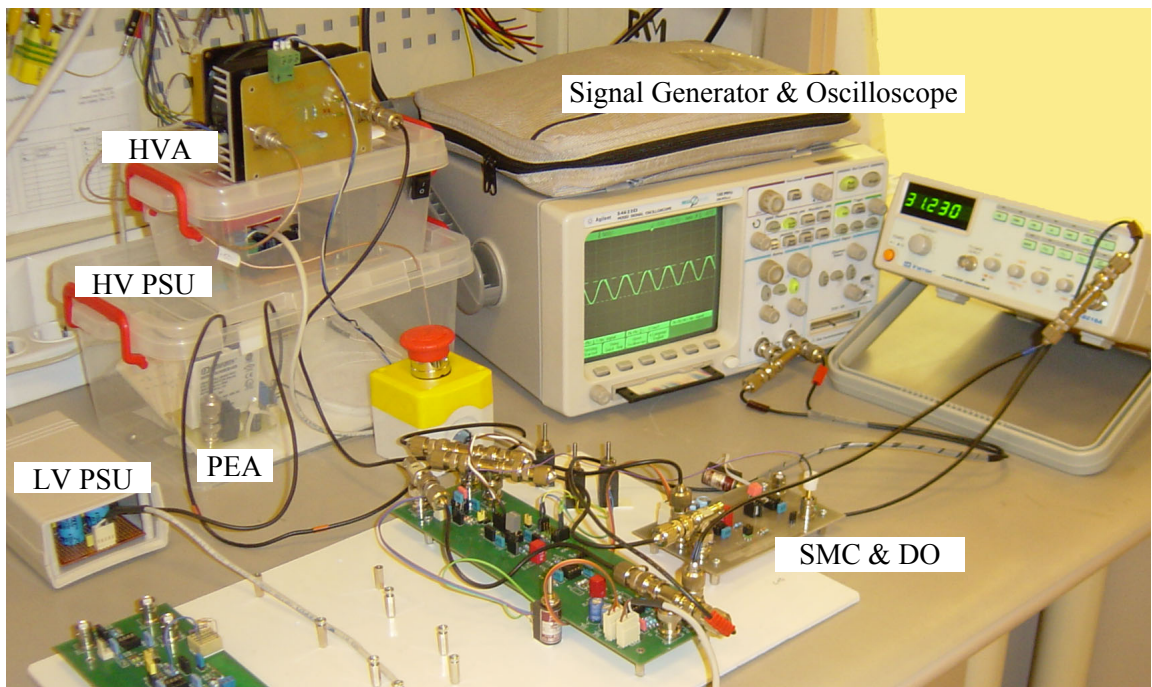


Figure 4.2: Actual photo of the experimental setup.

4.2 Model Verification

Most of the controller design and disturbance observer calculations is based on the selected plant model. Therefore the selected piezoelectric actuator model in this research must be compared with the real plant for model verification and parameter validity. The parameters used in the simulation are listed in Table 3.2 and the experimental part of the work is realized by Abidi [26].

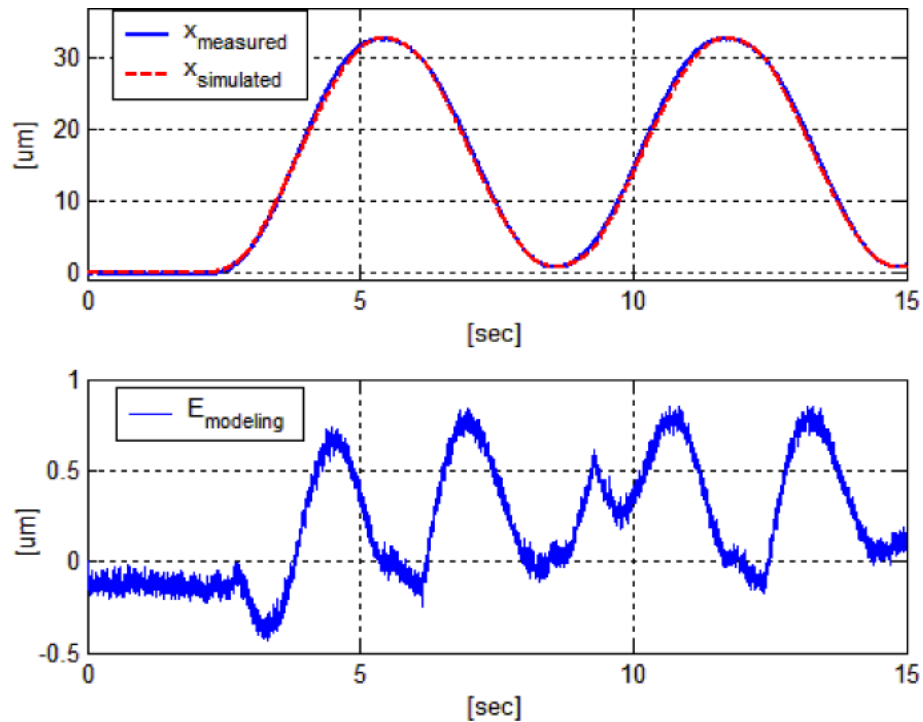


Figure 4.3: Real vs. simulated trajectory of the PEA for the input: $u=40+40.\sin(t)$ Volts presented with the corresponding modeling error.

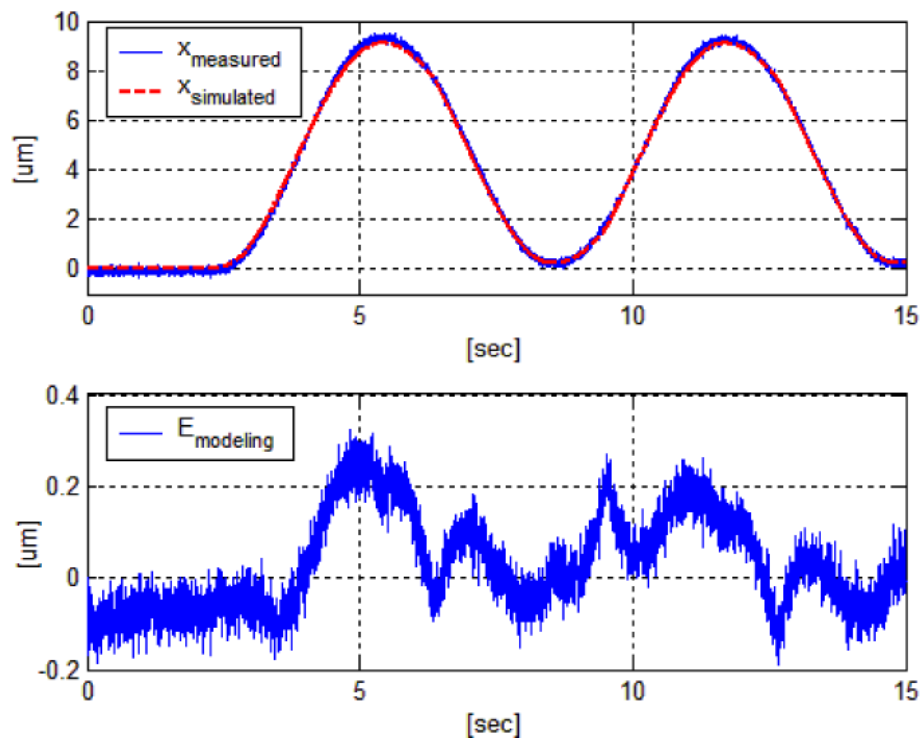


Figure 4.4: Real vs. simulated trajectory of the PEA for the input: $u=15+15.\sin(t)$ Volts presented with the corresponding modeling error.

The described model was used to estimate the response of the PEA to two different sinusoidal inputs each having an offset equal to the amplitude of the signal to

ensure only positive motion of the actuator. The resulting outputs are depicted in Figure 4.3 and Figure 4.4. From the work of Abidi [26], we can conclude that the selected model and calculated nominal plant parameters are able to estimate the PEA plant in focus quite satisfactorily especially for the residual displacement when the input tends to zero. The modeling errors are about 3.4% according to the experiments and we believe that the accuracy of the model is good enough to design a successful controller with disturbance compensation.

4.3 Open Loop Actuator Control

Since the selected model estimates the behavior of the actuator fairly well, as proven in the previous section, this model should be able to estimate the necessary input to the actual plant in order to follow a certain reference trajectory. This approach requires the inverse model calculation which is represented as a block diagram in Figure 4.5. So-called open-loop technique based on inverse model is presented to further compare with the closed-loop performance and demonstrate the added value by the Sliding Mode Controller.

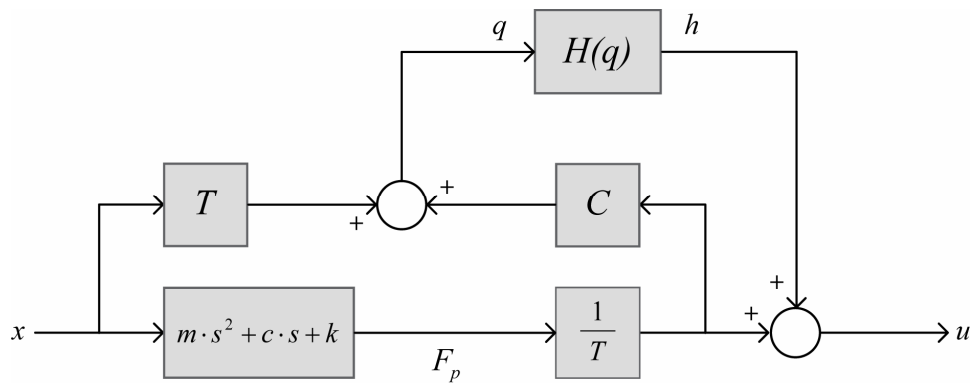


Figure 4.5: Inverse plant model for the Goldfarb-Celanovic model.

One point must be stressed; even though it is possible, the inverse model does not include the external force since that would involve force measurement and possible complications. However, since in the final application, the externally applied force to the PEA is assumed as a part of the disturbance, above cited reduction is not totally unrealistic.

Experimental tracking error is 6.7% as represented in Figure 4.6 which also shows the voltage control signal calculated by the inverse model.

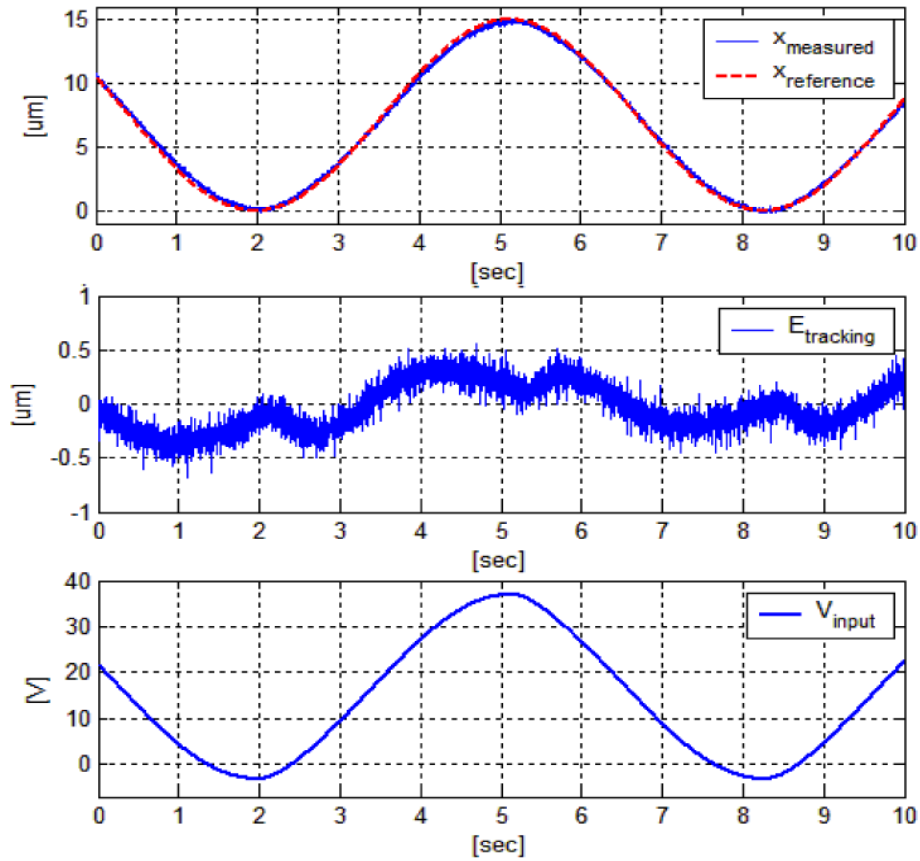


Figure 4.6: Open-loop tracking error and input voltage for $x_d = 7.5 + 7.5 \cdot \sin(t) \mu\text{m}$

4.4 Position Tracking Experiments Using DSP

DSP application of the control is realized on dSpace DS1102 platform which possesses TMS320C31 DSP chip running at 40MHz with 50ns cycle time. The platform has two 16-bit ADC (Input) $\pm 10\text{V}$ and four 12-bit DAC (Outputs) $\pm 10\text{V}$. The algorithm runs at 10kHz, and the discretization is made based on Euler's method.

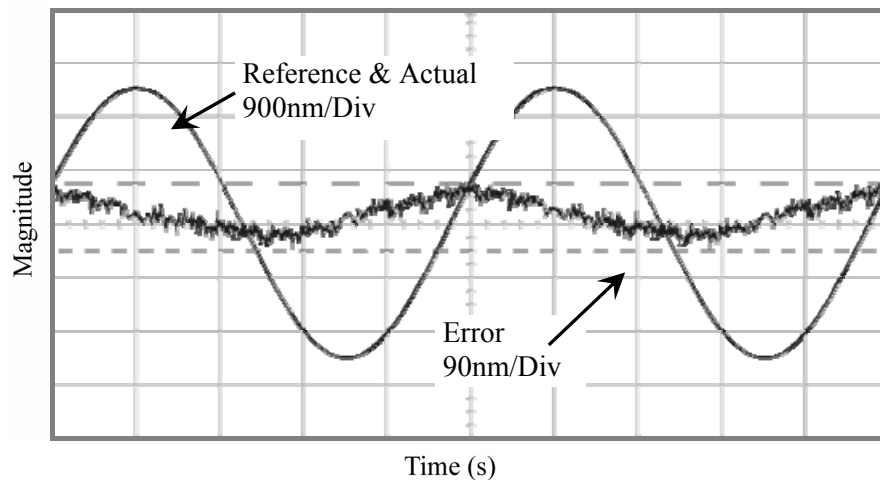


Figure 4.7: DSP tracking of 4.5 μm -pp 1Hz sinusoidal reference. The error is 110nm-pp (2.4%).

The position tracking of 1Hz sinusoidal inputs is studied. First 4.5 μm peak to peak and then 10.8 μm peak to peak inputs are tested. The results are shown in Figure 4.7 and Figure 4.8. The errors for comparison are 110nm and 200nm, corresponding to 2.4% and 1.8% respectively.

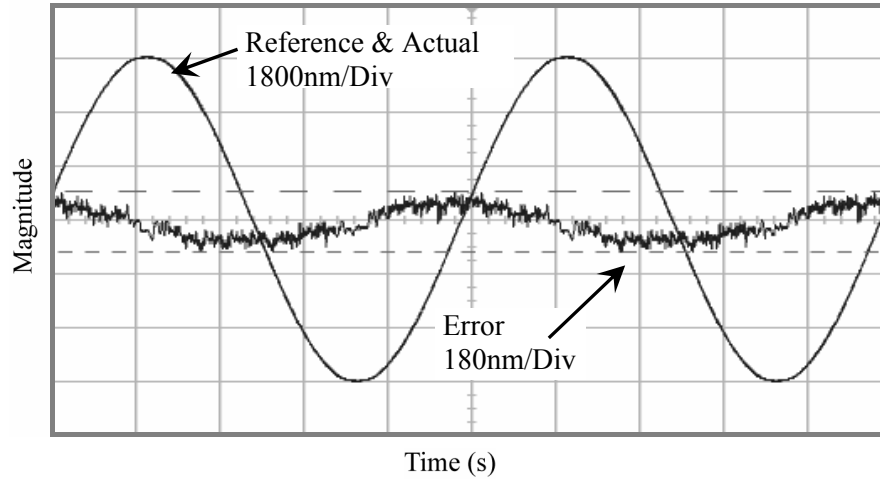
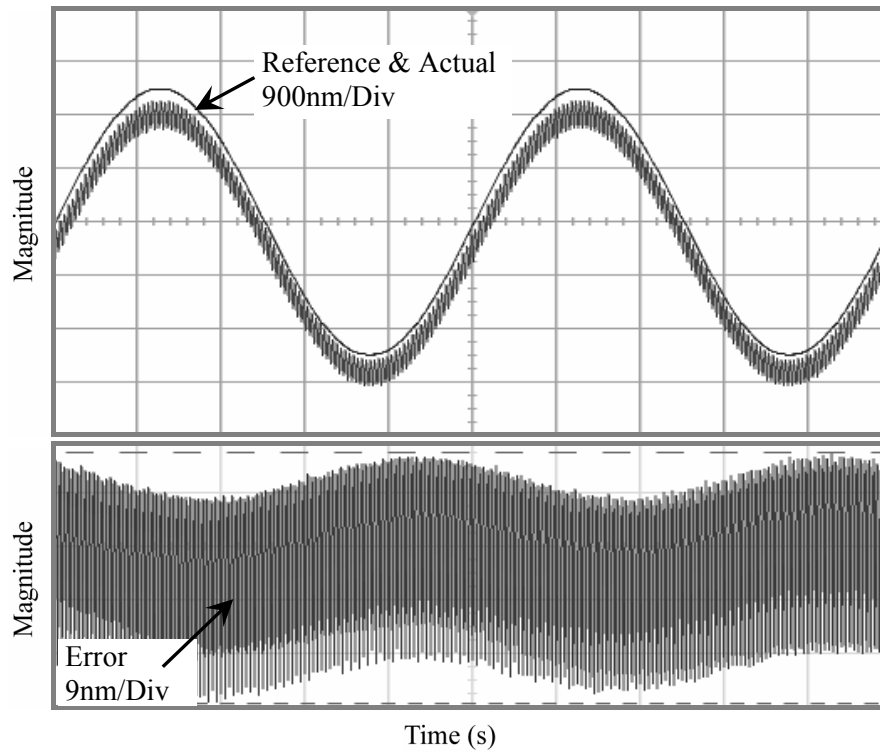


Figure 4.8: DSP tracking of 10.8 μm -pp 1Hz sinusoidal reference. The error is 200nm-pp (1.8%).

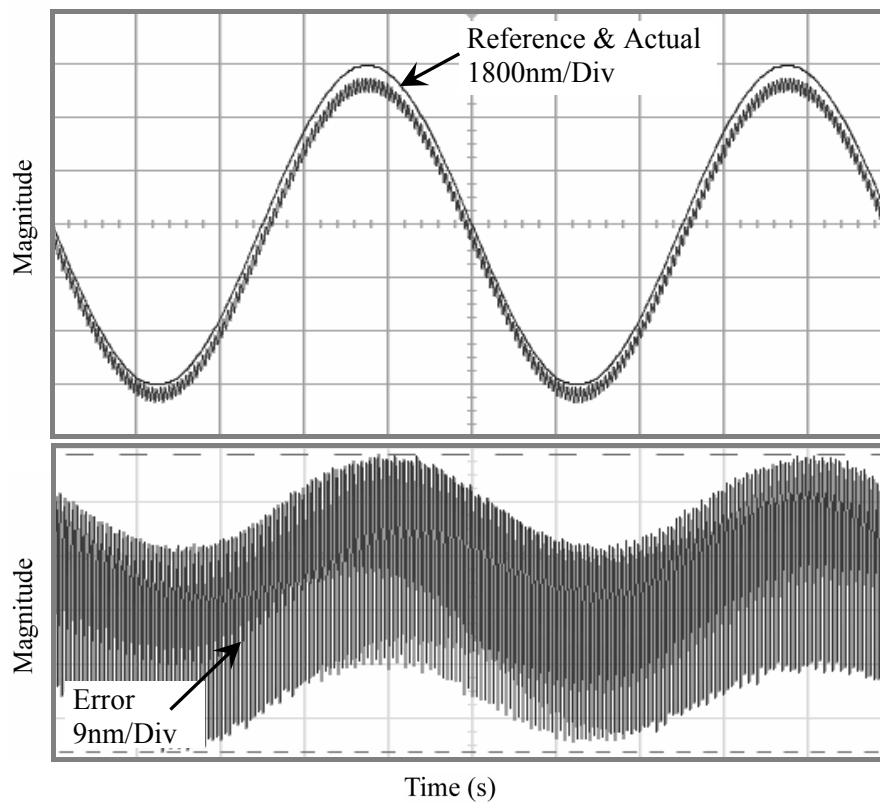
4.5 Analog SMC Position Tracking Experiments

Similar experiments are conducted for analog circuit realization of the SMC without the use of the disturbance observer. As can be seen on Figure 4.9 and Figure 4.10, 4.5 μm peak to peak 1Hz sinusoidal (Figure 4.9, part A) and triangular (Figure 4.10, part A) references are successfully tracked with 46.8nm and 44.8nm peak to peak tracking errors corresponding to 1.04% and 1.00% respectively. On the same figures, the tracking of 10.8 μm peak to peak 1Hz sinusoidal (Figure 4.9, part B) and triangular (Figure 4.10, part B) references are also presented. The corresponding tracking errors are 55.0 and 55.9nm peak to peak corresponding to 0.51% and 0.52% respectively.

From all four experiments, together with the DSP experimental results from last section, we can resume that the tracking control of the analog implementation performs 2 to 3 times better than DSP implementation of the same controller.

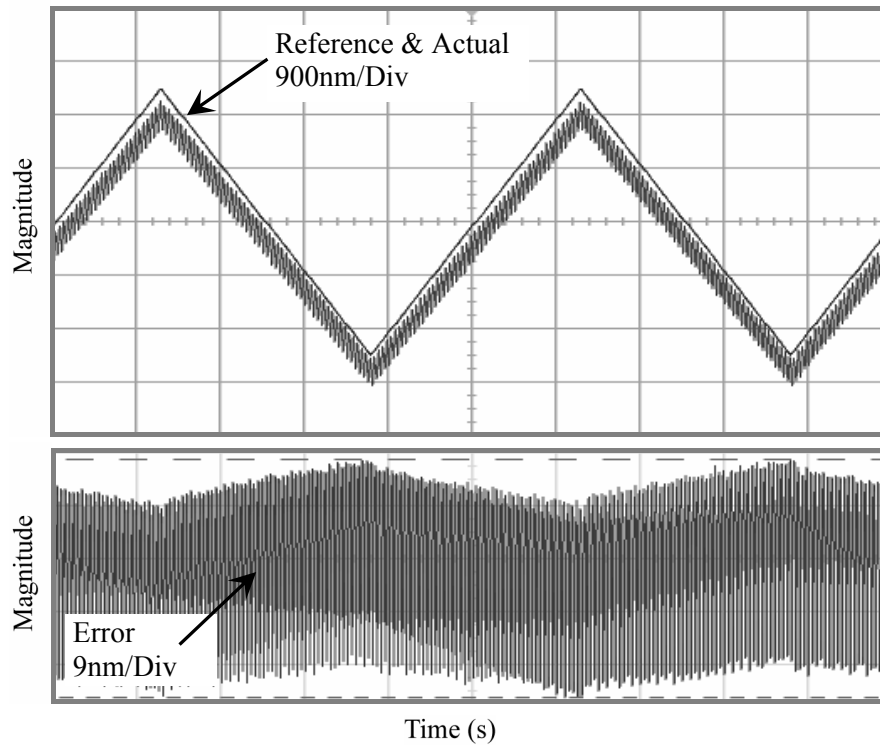


A/ Reference and actual positions shown at top (900nm/div) and error at bottom (9nm/div). The error is 46.8nm-pp (1.04%).

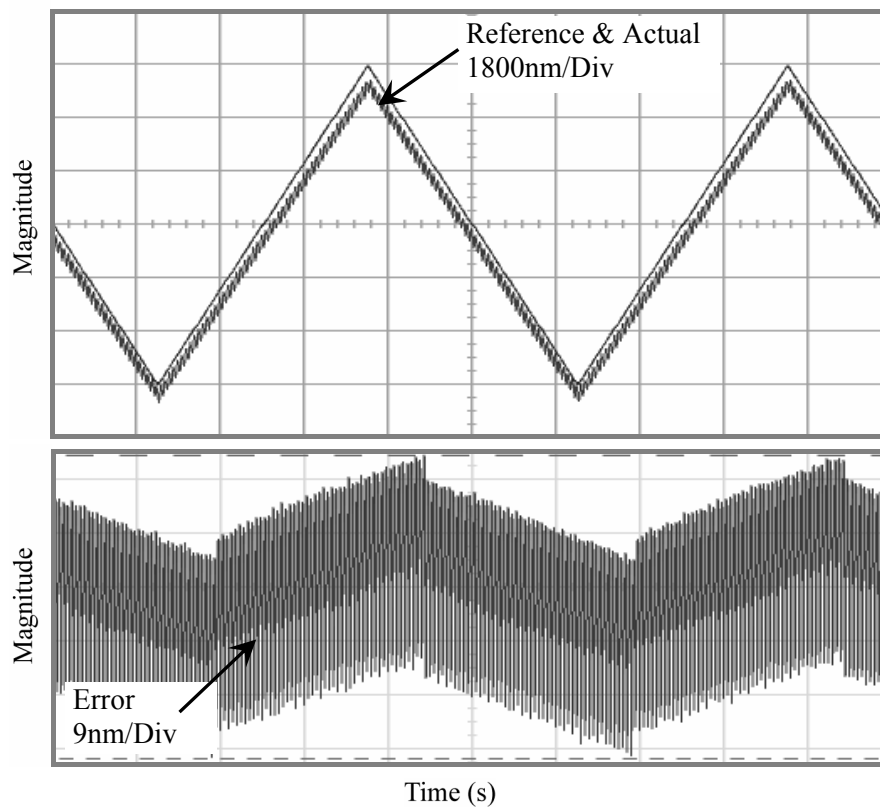


B/ Reference and actual positions shown at top (1800nm/div) and error at bottom (9nm/div). The error is 55.0nm-pp (0.51%).

Figure 4.9: ASMC tracking experiments for 4.5 and 10.8 μ m-pp 1Hz sinusoidal references.



A/ Reference and actual positions shown at top (900nm/div) and error at bottom (9nm/div). The error is 44.8nm-pp (1.0%).



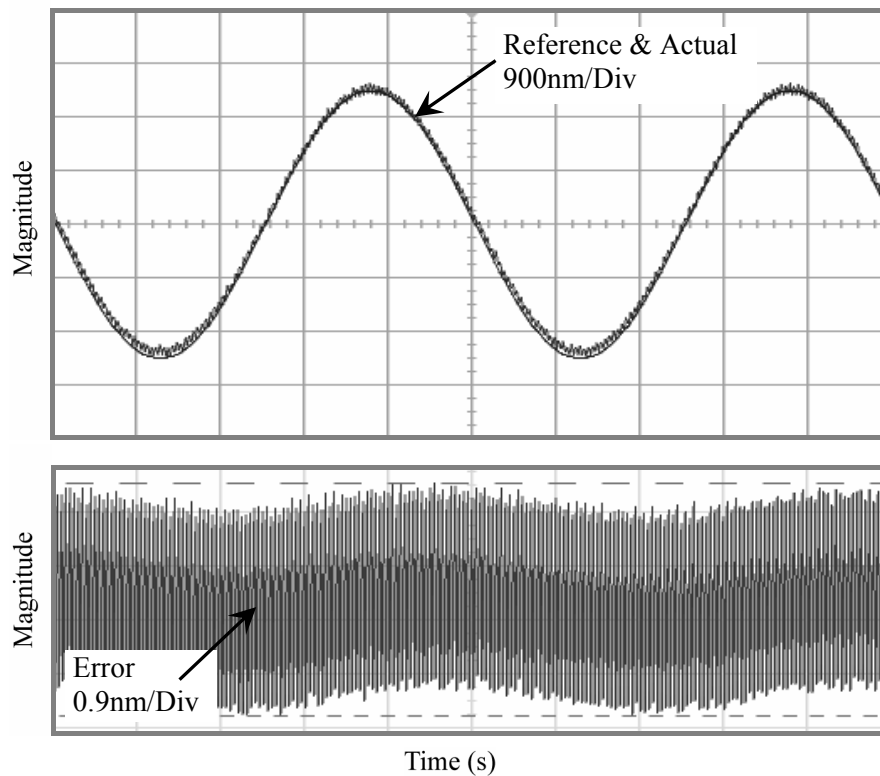
B/ Reference and actual positions shown at top (1800nm/div) and error at bottom (9nm/div). The error is 55.9nm-pp (0.52%).

Figure 4.10: ASMC tracking experiments for 4.5um-pp and 10.8um-pp 1Hz triangular references.

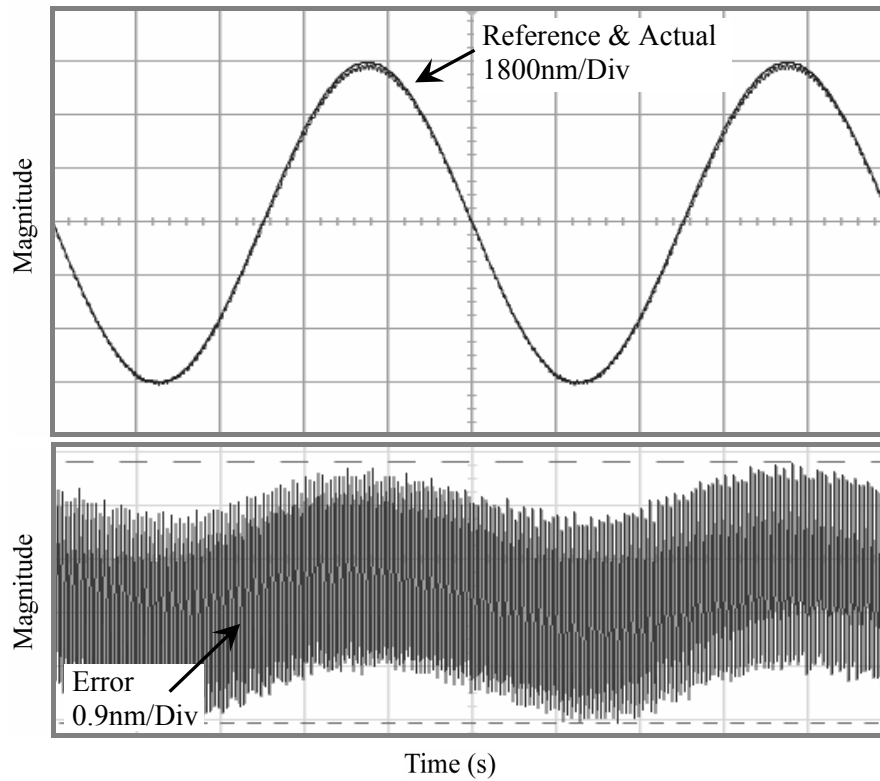
4.6 Analog SMC with Disturbance Observer

Same experiments are repeated for the Analog Sliding Mode Controller with the addition of the designed disturbance observer circuit. The tracking of a 4.5 μm peak to peak 1Hz sinusoidal reference resulted with 4.3nm peak to peak tracking error corresponding to only 0.10%. Compared to the 2.5% tracking error of the DSP implementation, this result is 25 times better (Figure 4.11). The same experiment repeated for 10.8 μm peak to peak sinusoidal input and the experiment resulted with 4.85nm peak to peak error corresponding to only 0.045%.

Triangular wave shapes experiments presented on previous section are repeated in the presence of a disturbance observer. Tracking of 4.5 μm and 10.8 μm peak to peak references succeeded with 4.52nm peak to peak (0.10%) and 4.95nm peak to peak (0.046%) errors respectively (Figure 4.12). Results are at least 10 times better compare to the just Analog Sliding Mode Controller case.

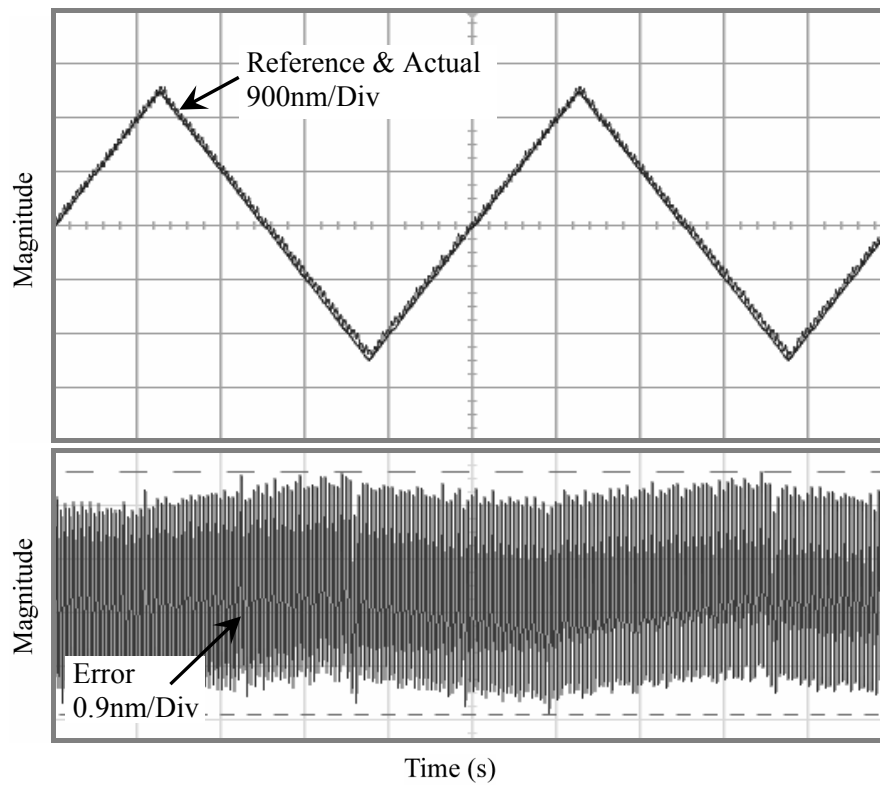


A/ Reference and Actual positions shown at top (900nm/div) and error at bottom (0.9nm/div). The error is 4.52nm-pp 4.3nm-pp (0.10%)

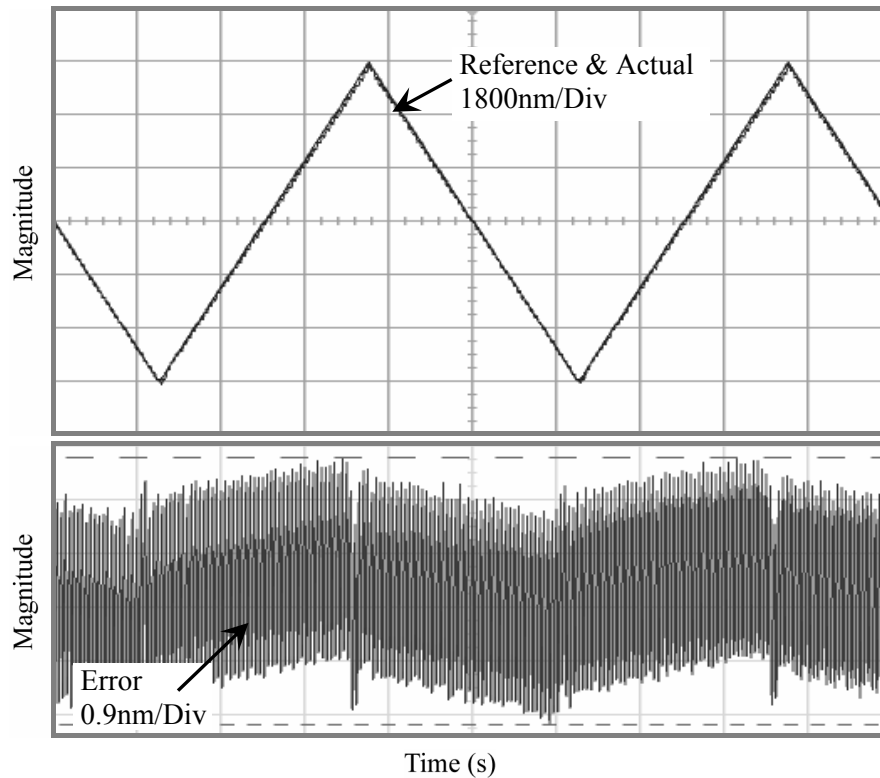


B/ Reference and Actual positions shown at top (1800nm/div) and error at bottom (0.9nm/div). The error is 4.85nm-pp (0.045%).

Figure 4.11: ASMC with DO tracking experiments for 4.5 and 10.8 μ m-pp 1Hz sinusoidal references.



A/ Reference and Actual positions shown at top (900nm/div) and error at bottom (0.9nm/div). The error is 4.52nm-pp (0.10%).



B/ Reference and Actual positions shown at top (1800nm/div) and error at bottom (0.9nm/div). The error is 4.95nm-pp (0.046%).

Figure 4.12: ASMC with DO tracking experiments for 4.5 and 10.8um-pp 1Hz triangular references.

To present the tracking of an abstract but continuous wave form, the tracking of a human heart beat signal is presented in Figure 4.13. For this waveform with peak to peak amplitude of 21.70um, the tracking resulted with 46nm peak to peak tracking error corresponding to 0.21%.

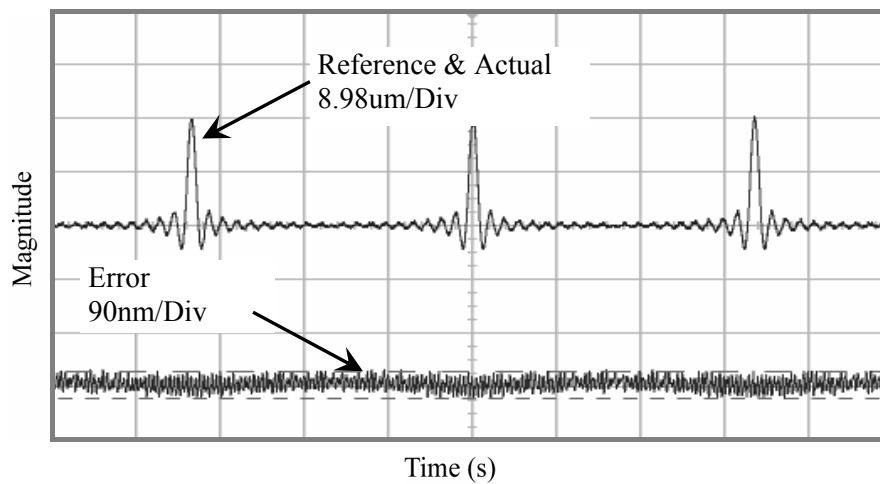


Figure 4.13: Tracking of human heart beat signal. The peak to peak reference signal is 21.70um. The error is 46nm-pp (0.21%).

4.7 Summary of the Experimental Results

Different position tracking experiments are performed for different controllers. To show the improvement of the work achieved in this research a comparison of the experimental results is presented on Table 4.1.

Form the table we can conclude that the Analog Sliding Mode Controller, designed and built in this research, performs more than 2 times better than the DSP implementation, when not supported by the disturbance observer. In the presence of the disturbance observer, the trajectory tracking performance increases more than 20 times.

For the triangular shape trajectory tracking, very similar results are obtained. Since for a perfect triangular wave, the derivative is not continuous, triangular trajectories constitutes important information. The non-continuous derivative may cause saturated signals and the circuit is expected to recover from the situation otherwise increase in the error may be observed.

Another important result from the table is regarding the signal sizes; since the controller performs well and the measurable output signals are continuous, we can conclude that the used operational amplifiers are not saturated during experiments. This reaction is expected since the scaling process summarized in 3.8.2 is used to ensure this behavior.

Table 4.1: Summary of the experimental results.

Input	Controller	Position Error for Reference Amplitude of	
		4.5 μ m-pp (250mV-pp)	10.8 μ m-pp (600mV-pp)
1Hz Sinusoidal	SMC implemented on DSP	110nm 2.4%	200nm 1.8%
	SMC implemented on Analog Electronics	46.8nm 1.05%	50nm 0.14%
	SMC with DO implemented on Analog Electronics	4.5nm 0.10%	4.85nm 0.045%
1Hz Triangular	SMC implemented on Analog Electronics	44.8nm 1.00%	55.9nm 0.52%
	SMC with DO implemented on Analog Electronics	4.52nm 0.10%	4.95nm 0.046%

On the other hand, observing the experimental output signals, one can remark that, the error signal is a wide trace mainly due to the high frequency noise contained in it. To prove the existence and size of the noise on the error signal, an experiment requiring the tracking of a single sinusoidal pulse of period 1 second and peak to peak amplitude 35.60 μm as shown in Figure 4.14. Accordingly, the peak to peak error value is 54nm corresponding to 0.15% tracking error. But the important point in this experiment is that, the error before the pulse, namely for zero reference input, was already around 40nm. This error includes the high frequency noise that interferes from position measurement to the calculation of the control. Hence oscillations around the reference are also part of the error.

The source of the noise does not require deep investigation to be discovered; the position measurement signal from the strain gage contains similar high frequency elements in it. Since the position measurement is relatively large signal, on the orders of few hundred millivolts, the SNR (signal to noise ratio) is high. However, since the error is expected to tend to zero, it is a small signal on the order of few millivolts, and therefore SNR is low. High SNR results with noisy signals that can still carry its characteristics but low SNR results with signal information loss since the signal magnitudes becomes comparable to the noise magnitude.

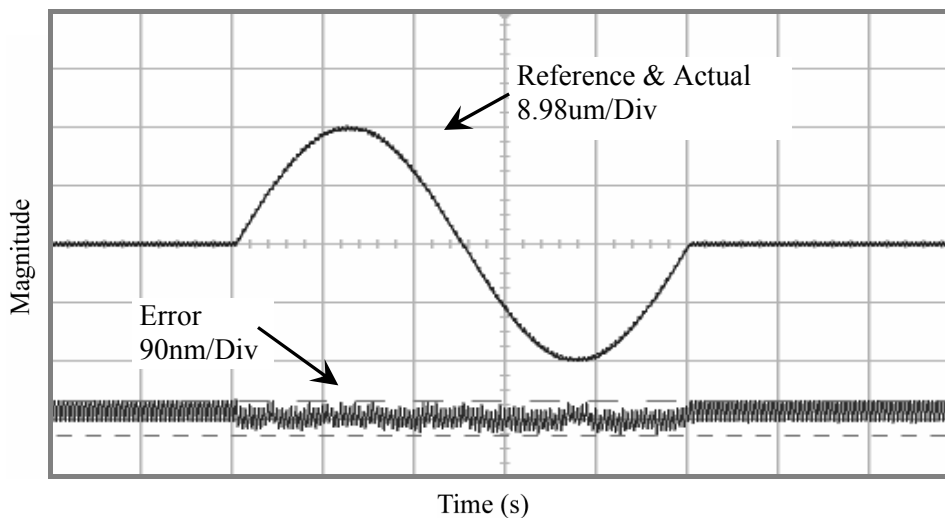


Figure 4.14: Tracking of 35.60 μm -pp 1Hz sinusoidal reference. The error is 54nm-pp (0.15%).

Filtering of the measurement signals may help to further increase the performance but in such a case the filtering may cause phase shifts, delay and/or other information loss. Therefore the filter should be adaptive and care must be taken in the design. The whole control algorithm is based on the error and its first derivative, therefore, instead

of filtering the measurement signal, cleaning the error signal and its derivatives may help more.



5 CONCLUSION AND FUTURE WORK

In this research SMC design methodology is used to arrive to a controller that has very small discontinuous component or in some cases no discontinuous component if the exponential convergence to sliding mode manifold is acceptable. Furthermore, the controller is combined with a disturbance observer in order to improve the tracking performance. The structure is kept as simple as possible in order to allow analog implementation with limited hardware. The aim in the later stage is to try to integrate a whole controller as a part of the plant together with the high voltage amplifier and that way create a monolithic actuator-controller. So far, in this text, the design of the control strategy and disturbance rejection methods are presented together with the promising analyses results. Circuit design is also summarized and followed by comparative experimental work. The designed control circuitry is proven to perform 10 to 25 times better compare to the DSP implementation of the same algorithms. In this part of the text, the results will be further discussed with possible future works.

5.1 Conclusions

Even tough, controllers applied on digital systems, promise ease of re-programmability, multi-DOF systems, with each axis motion independently measured and controlled, the application of the control requires high computational power and careful software implementation.

This work aimed to move the controller outside of the digital domain and use the digital controllers only for reference generation. This way *improvement on the tracking performance* and *decrease on the computational power necessity* is targeted. Research is motivated by the need of a motion controller for a 14-DOF Microassembly Workstation [1, 2] designed and built in Sabanci University for experimental purposes. And therefore the piezoelectric actuator is selected as the experimental plant since it is the main actuation source in the cited and in many other microsystem applications with a wide range of industrial applications. However beside their potential unlimited

resolution possibility, precise control of piezoelectric actuators is a challenging task due to the dominant hysteresis and other non-linear behaviors. Besides, the position measurement methods are not mature enough and can only provide measurements signals of very small in amplitude. The solution requires well designed, robust yet large bandwidth controllers with capability of rejecting external disturbances.

This thesis investigated the possibility of designing an *analog motion controller* for single input single output (SISO) systems of complex nature, based on non-linear control methodologies. The designed controller assures a quazi-sliding mode motion with exponential convergence to the selected sliding mode manifold. The combination of disturbance observer and the SMC based controller allows very compact analog electronics implementation.

Experimental results proved that the analog implementation of the proposed SMC is acceptable and that the controller can track a reference signal with high accuracy. In comparison with DSP realization of the same algorithm, the realization in continuous time domain showed at least 2 times performance increase. The addition of the disturbance observer on the other hand, improved this result another 10 times. Resulting controller can track appropriate signals at around 0.05% tracking error corresponding to 50nm for reference amplitude of 1 μ m. Achieved performance is already well adequate for the Microassembly Workstation project that inspired this research.

The system tracking performance is not as successful for smaller signals on the other hand. As it can be seen from Figure 4.14, the error signal is augmented by a group of high frequency signals. Part of the signal is caused by the high gain SMC, while majority is the noise introduced by the position measurement by the strain gage and amplified by the electronics.

It is known that the piezoelectric crystals dissipate some heat even at low frequency operation since their impedance is close to a capacitor with certain internal resistance. Strain gage, being another piezoelectric crystal attached on the body of the actuator, is affected by this heat and therefore may generate extra noise. To prevent this situation, in many works expensive capacitive sensors with very high resolutions are used. In this research, for the price of large noise, inexpensive strain gage position measurements are preferred in purpose since the capacitive sensor placement in real applications like robotics introduces additional design constraints in mechanics domain.

Even though high frequency operations are targeted at the beginning of the research phase, mainly limited by filter and the introduced filters, the final products bandwidth is not large enough. We believe that miniaturization in the circuit design may help in noise reduction but the ultimate solution will be integrated circuit application as will be discussed on the later section.

To sum up all, the Analog Sliding Mode Controller in the presence of a disturbance observer is promising. However, the development phase is very demanding. The work done in this research may be accepted as an introduction to the field where so far not much work exists. Yet we believe that the area shows potential and much work can be done.

5.2 Recommendations and Future Work

From the experience of this research, the following future works are suggested and are discussed in this part of the text;

- Sensorless operation
- IC design & application

The implementation in this thesis consists of two piezoelectric materials; one is configured as a stack actuator while the other as strain gage for stroke measurement. It is possible to combine the sensor and the actuator into a single element called a self-sensing actuator [71]. In that case, since the impedance of the piezoelectric actuator is essentially that of a capacitor, instead of resistive Whetstone Bridge for position measurement, capacitive Whetstone Bridge, a bridge structure with all elements being capacitors, can be used. The bridge supply voltage will also act as the control voltage of the actuator. By appropriate selection of the bridge capacitors one can make the output proportional to the position and that way may avoid large voltages of measurement. It is also possible to have configuration for force measurement.

Another important future target would be on the integrated circuit (IC) implementation and production of this design. There is a continuous trend in miniaturization for current and future subsystems mainly for mobile and autonomous applications. For electronics the state of the art miniaturization is IC applications. Application of the proposed control system design in microelectronics domain as a full monolithic integrated circuit, will supply many benefits to the user including saving from noise interactions and therefore much higher operation frequency.

For the circuit integration of sliding-mode controller, not much work exists in the area, to the best knowledge of the author. In particular, the only sliding-mode application specific integrated circuit reported so far is the work by Alarcon et al. [72]. Designed for switching converters of mass production, their implementation realized on an area of 0.33mm^2 and features a bandwidth of 2MHz.



6 REFERENCES

- [1] E. D. Kunt, K. Cakir, and A. Sabanovic, "A workstation for microassembly," presented at Mediterranean Conference on Control & Automation, 2007. MED '07, 2007.
- [2] E. D. Kunt, "Design and Realization of a Microassembly Workstation." İstanbul: Sabanci University, 2006, pp. 102.
- [3] K. D. Young, V. I. Utkin, and U. Ozguner, "A Control Engineer's Guide to Sliding Mode Control," *Control Systems Technology, IEEE Transactions on*, vol. 7, pp. 328-342, 1999.
- [4] K. D. Young, V. I. Utkin, and U. Ozguner, "A Control Engineer's Guide to Sliding Mode Control," presented at Variable Structure Systems, 1996. VSS '96. Proceedings., 1996 IEEE International Workshop on, 1996.
- [5] C. W. Lim and C. W. H. Lau, "A new two-dimensional model for electro-mechanical response of thick laminated piezoelectric actuator," *International Journal of Solids and Structures*, vol. In Press, Corrected Proof.
- [6] A. Suleman and A. P. Costa, "Adaptive control of an aeroelastic flight vehicle using piezoelectric actuators," *Computers & Structures*, vol. 82, pp. 1303-1314, 2004.
- [7] PI, "Physik Instrumente (PI) GmbH & Co. KG: <http://www.physikinstrumente.de>," 2005.
- [8] T. Morita, "Miniature piezoelectric motors," *Sensors and Actuators A: Physical*, vol. 103, pp. 291-300, 2003.
- [9] B. Zhai, S.-P. Lim, K.-H. Lee, S. Dong, and P. Lu, "A modified ultrasonic linear motor," *Sensors and Actuators A: Physical*, vol. 86, pp. 154-158, 2000.
- [10] S. Ashley, "Digital dampers," in *Mechanical Engineering*, vol. 120: American Society of Mechanical Engineers, 1998, pp. 130.
- [11] G. L. C. M. de Abreu and J. F. Ribeiro, "A self-organizing fuzzy logic controller for the active control of flexible structures using piezoelectric actuators," *Applied Soft Computing*, vol. 1, pp. 271-283, 2002.
- [12] Janker, Peter, M. Christmann, F. Hermle, T. Lorkowski, and S. Storm, "Mechatronics using piezoelectric actuators," *Journal of the European Ceramic Society*, vol. 19, pp. 1127-1131, 1999.
- [13] B. N. Agrawal, M. A. Elshafei, and G. Song, "Adaptive antenna shape control using piezoelectric actuators," *Acta Astronautica*, vol. 40, pp. 821-826, 1997.
- [14] "Shape shifting aircraft," in *Design Engineering*: Centaur Communications, 2001, pp. 5.
- [15] C. Duncheon, "Robots will be of service with muscles, not motors," *Industrial Robot-an International Journal*, vol. 32, pp. 452-455, 2005.
- [16] S. Fahlbusch, S. Fatikow, J. Seyfried, and A. Buerkle, "Flexible microrobotic system MINIMAN: design, actuation principle and control," presented at

- Advanced Intelligent Mechatronics, 1999. Proceedings. 1999 IEEE/ASME International Conference on, 1999.
- [17] J. Domingo, M. Puig-Vidal, J. Lopez, and J. Samitier, "Nonlinear control system based on fuzzy logic technique applied to drive piezoactuators for micro robotic applications MINIMAN: MINIaturised robot for micro MANipulation," presented at Emerging Technologies and Factory Automation, 1999. Proceedings. ETFA '99. 1999 7th IEEE International Conference on, 1999.
- [18] U. Simu and S. Johansson, "Evaluation of a monolithic piezoelectric drive unit for a miniature robot," in *Sensors & Actuators A: Physical*, vol. 101, 2002, pp. 175.
- [19] T. Kusakawa, A. Torii, K. Doki, and A. Ueda, "Control waveforms applied to piezo elements used in a miniature robot," presented at Micro-Nanomechatronics and Human Science, 2004 and The Fourth Symposium Micro-Nanomechatronics for Information-Based Society, 2004. Proceedings of the 2004 International Symposium on, 2004.
- [20] O. Fuchiwaki, N. Tobe, H. Aoyama, D. Misaki, and T. Usuda, "Automatic micro-indentation and inspection system by piezo driven micro robot with multiple inner sensors," presented at Mechatronics and Automation, 2005 IEEE International Conference, 2005.
- [21] H. Aoyama, O. Fuchiwaki, D. Misaki, and T. Usuda, "Desktop Micro Machining System by Multiple Micro Robots," presented at Robotics, Automation and Mechatronics, 2006 IEEE Conference on, 2006.
- [22] W. Yim and S. N. Singh, "Variable Structure Adaptive Force Tracking Control of a Cantilever Beam Using a Piezoelectric Actuator," in *Journal of Vibration & Control*, vol. 6: Sage Publications, Ltd., 2000, pp. 1029.
- [23] H. Richter, E. A. Misawa, D. A. Lucca, and H. Lu, "Modeling nonlinear behavior in a piezoelectric actuator," *Precision Engineering*, vol. 25, pp. 128-137, 2001.
- [24] N. Tamer and M. Dahleh, "Feedback control of piezoelectric tube scanners," presented at Decision and Control, 1994., Proceedings of the 33rd IEEE Conference on, 1994.
- [25] B. M. Chen, T. H. Lee, C.-C. Hang, Y. Guo, and S. Weerasooriya, "An Hinf almost disturbance decoupling robust controller design for a piezoelectric bimorph actuator with hysteresis," *Control Systems Technology, IEEE Transactions on*, vol. 7, pp. 160-174, 1999.
- [26] K. Abidi, "Sliding-Mode control for high-precision motion control systems / Thesis Advisor Asif Sabanovic." Istanbul: Sabanci University, 2004.
- [27] Y. T. Liu, R. F. Fung, and C. C. Wang, "Precision position control using combined piezo-VCM actuators," *Precision Engineering-Journal of the International Societies for Precision Engineering and Nanotechnology*, vol. 29, pp. 411-422, 2005.
- [28] H. v. d. Wulp, *Piezo-driven stages for nanopositioning with extreme stability: theoretical aspects and practical design considerations*. Delft, Netherlands: Delft University Press, 1997.
- [29] K. Uchino, "Materials issues in design and performance of piezoelectric actuators: an overview," *Acta Materialia*, vol. 46, pp. 3745-3753, 1998.
- [30] K. Uchino, *Piezoelectric Actuators and Ultrasonic Motors*. Boston ; Dordrecht: Kluwer Academic Publishers, 1997.

- [31] D. Zhang, C. Chang, T. Ono, and M. Esashi, "A piezodriven XY-microstage for multiprobe nanorecording," *Sensors and Actuators A: Physical*, vol. 108, pp. 230-233, 2003.
- [32] S. Bauer, "Piezo-, pyro- and ferroelectrets: soft transducer materials for electromechanical energy conversion," *Dielectrics and Electrical Insulation, IEEE Transactions on [see also Electrical Insulation, IEEE Transactions on]*, vol. 13, pp. 953-962, 2006.
- [33] H.-J. Shieh, F.-J. Lin, P.-K. Huang, and L.-T. Teng, "Adaptive tracking control solely using displacement feedback for a piezo-positioning mechanism," *Control Theory and Applications, IEE Proceedings-*, vol. 151, pp. 653-660, 2004.
- [34] H. J. M. T. S. Adriaens, W. L. De Koning, and R. Banning, "Modeling piezoelectric actuators," *Mechatronics, IEEE/ASME Transactions on*, vol. 5, pp. 331-341, 2000.
- [35] R. Banning, W. L. de Koning, H. J. M. T. A. Adriaens, and R. K. Koops, "State-space analysis and identification for a class of hysteretic systems," *Automatica*, vol. 37, pp. 1883-1892, 2001.
- [36] M. Goldfarb and N. Celanovic, "Modeling piezoelectric stack actuators for control of micromanipulation," *Control Systems Magazine, IEEE*, vol. 17, pp. 69-79, 1997.
- [37] J.-J. Tzen, S.-L. Jeng, and W.-H. Chieng, "Modeling of piezoelectric actuator for compensation and controller design," *Precision Engineering*, vol. 27, pp. 70-86, 2003.
- [38] C.-H. Yang and K.-M. Chang, "Adaptive Neural Network Control for Piezoelectric Hysteresis Compensation in A Positioning System," presented at Industrial Electronics, 2006 IEEE International Symposium on, 2006.
- [39] Y. Wu and Q. Zou, "Iterative control approach to compensate for the hysteresis and the vibrational dynamics effects of piezo actuators," presented at American Control Conference, 2006, 2006.
- [40] H. Jung, H. Jung, J. Y. Shim, J. Y. Shim, D. Gweon, and D. Gweon, "New Open-loop Actuating Method of Piezoelectric Actuators for Removing Hysteresis and Creep," *Review of Scientific Instruments*, vol. 71, 2000.
- [41] Y.-C. Yu and M.-K. Lee, "A dynamic nonlinearity model for a piezo-actuated positioning system," presented at Mechatronics, 2005. ICM '05. IEEE International Conference on, 2005.
- [42] "IEEE standard on piezoelectricity," in *ANSI/IEEE Std 176-1987*, 1988.
- [43] M. Guan and W.-H. Liao, "Studies on the circuit models of piezoelectric ceramics," presented at Information Acquisition, 2004. Proceedings. International Conference on, 2004.
- [44] D. C. Jiles and D. L. Atherton, "Theory of ferromagnetic hysteresis," *Journal of Magnetism and Magnetic Materials*, vol. 61, pp. 48-60, 1986.
- [45] Y. Pasco and A. Berry, "Consideration of piezoceramic actuator nonlinearity in the active isolation of deterministic vibration," *Journal of Sound and Vibration*, vol. In Press, Corrected Proof.
- [46] D. Song and C. J. Li, "Modeling of piezo actuator's nonlinear and frequency dependent dynamics," *Mechatronics*, vol. 9, pp. 391-410, 1999.
- [47] R. H. Comstock, "Charge Control of Piezoelectric Actuators to Reduce Hysteresis Effects." U.S. Patent 4,263,527: The Charles Stark Draper Laboratory, Inc. (Cambridge, MA), 1981.

- [48] C. Newcomb and I. Flinn, "Improving the Linearity of Piezoelectric Ceramic Actuators," *Electronics Letters*, vol. 18, pp. 442-444, 1982.
- [49] S. Lining, R. Changhai, R. Weibin, and C. L. a. K. Minxiu, "Tracking control of piezoelectric actuator based on a new mathematical model," in *Journal of Micromechanics & Microengineering*, vol. 14, 2004, pp. 1439-1444.
- [50] R.-J. Wai and J.-D. Lee, "Intelligent motion control for linear piezoelectric ceramic motor drive," *Systems, Man and Cybernetics, Part B, IEEE Transactions on*, vol. 34, pp. 2100-2111, 2004.
- [51] X. Zhao and Y. Tan, "Neural modeling for hysteresis in piezoelectrical actuator," presented at Control and Automation, 2005. ICCA '05. International Conference on, 2005.
- [52] Y.-C. Huang, K.-C. Chuang, M.-S. Lin, and C.-F. Chen, "Inspecting LED micro structure by piezo servo system," presented at Mechatronics, 2005. ICM '05. IEEE International Conference on, 2005.
- [53] F.-J. Lin, H.-J. Shieh, P.-K. Huang, and L.-T. Teng, "Adaptive control with hysteresis estimation and compensation using RFNN for piezo-actuator," *Ultrasonics, Ferroelectrics and Frequency Control, IEEE Transactions on*, vol. 53, pp. 1649-1661, 2006.
- [54] K. K. Leang and S. Devasia, "Design of hysteresis-compensating iterative learning control for piezo-positioners: Application to atomic force microscopes," *Mechatronics*, vol. 16, pp. 141-158, 2006.
- [55] K. Ohnishi, M. Shibata, and T. Murakami, "Motion control for advanced mechatronics," *Mechatronics, IEEE/ASME Transactions on*, vol. 1, pp. 56-67, 1996.
- [56] H. J. Shieh and C. H. Hsu, "An adaptive approximator-based backstepping control approach for piezoactuator-driven stages," *Ieee Transactions on Industrial Electronics*, vol. 55, pp. 1729-1738, 2008.
- [57] H.-J. Shieh, F.-J. Lin, P.-K. Huang, and L.-T. Teng, "Adaptive displacement control with hysteresis modeling for piezoactuated positioning mechanism," *Industrial Electronics, IEEE Transactions on*, vol. 53, pp. 905-914, 2006.
- [58] C. J. Lin and S. R. Yang, "Modeling of a piezo-actuated positioning stage based on a hysteresis observer," *Asian Journal of Control*, vol. 7, pp. 73-80, 2005.
- [59] C.-J. Lin and S.-R. Yang, "Precise positioning of piezo-actuated stages using hysteresis-observer based control," *Mechatronics*, vol. 16, pp. 417-426, 2006.
- [60] N. Bonnail, D. Tonneau, F. Jandard, G.-A. Capolino, and H. Dallaporta, "Variable Structure Control of a Piezoelectric Actuator for a Scanning Tunneling Microscope," in *IEEE Transactions on Industrial Electronics*, vol. 51, 2004, pp. 354-363.
- [61] K. Abidi, A. Sabanovic, and S. Yesilyurt, "Sliding mode control based disturbance compensation and external force estimation for a piezoelectric actuator," presented at Advanced Motion Control, 2004. AMC '04. The 8th IEEE International Workshop on, 2004.
- [62] K. Abidi, A. Sabanovic, and S. Yesilyurt, "Sliding-mode based force control of a piezoelectric actuator," presented at Mechatronics, 2004. ICM '04. Proceedings of the IEEE International Conference on, 2004.
- [63] A. Woronko, J. Huang, and Y. Altintas, "Piezoelectric tool actuator for precision machining on conventional CNC turning centers," in *Precision Engineering*, vol. 27, 2003, pp. 335.

- [64] S. K. Koji Yamada, Muneaki Ishida, Takamasa Hori,, "A study on higher-order disturbance observer and robust stability," *Electrical Engineering in Japan*, vol. 128, pp. 37-44, 1999.
- [65] S. Komada, N. Machii, and T. Hori, "Force control of redundant manipulators considering order of disturbance observer," presented at Industrial Electronics Society, 1998. IECON '98. Proceedings of the 24th Annual Conference of the IEEE, 1998.
- [66] S. Drakunov and V. Utkin, "A semigroup approach to discrete-time sliding modes," presented at American Control Conference, 1995. Proceedings of the, 1995.
- [67] W.-C. Su, S. V. Drakunov, and U. Ozguner, "An $O(T^2)$ boundary layer in sliding mode for sampled-data systems," *Automatic Control, IEEE Transactions on*, vol. 45, pp. 482-485, 2000.
- [68] V. Utkin, *Sliding Modes in Control and Optimization*, 1 ed. Berlin ; New York: Springer-Verlag, 1992.
- [69] Datasheet, "Texas Instruments TLE2074 Excalibur Low-Noise High-Speed JFET-Input Op Amps (Rev. B)," 2004.
- [70] Datasheet, "Apex Microtechnology MP108 Power Operational Amplifier," 2005.
- [71] A. Preumont, *Mechatronics: Dynamics of Electromechanical and Piezoelectric Systems*: Springer, 2006.
- [72] E. Alarcon, A. Romero, A. Poveda, S. Porta, and L. Martinez-Salamero, "CCII-based analog integrated circuit for sliding-mode control of switching power converters," *Analog Integrated Circuits and Signal Processing*, vol. 38, pp. 203-213, 2004.

